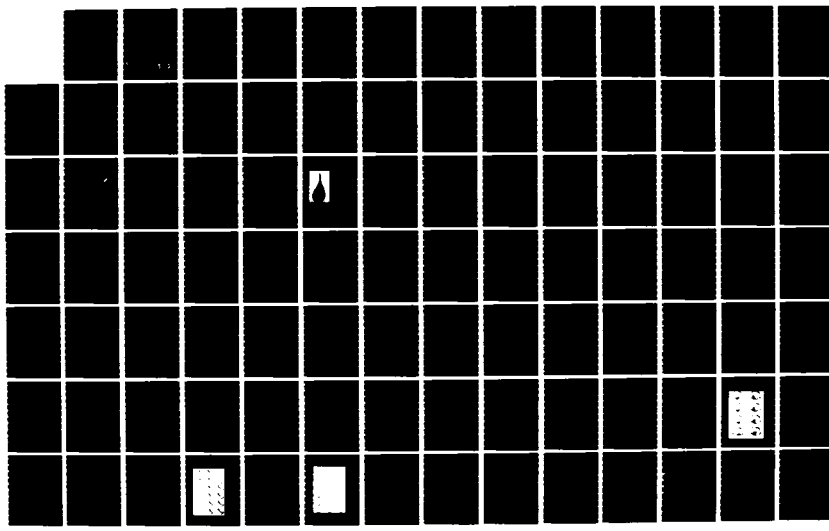
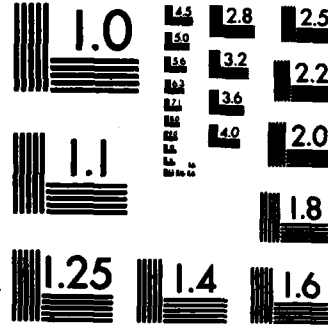


AD-A137 267 INTERPRETATION OF EXCITE SPECTRAL AND AURORAL INFRARED 1/2
SIMULATION DATA(U) PHOTOMETRICS INC WOBURN MA
I L KOFSKY ET AL. 30 NOV 82 PHM-TR-82-04 DNA-TR-81-191
UNCLASSIFIED DNA001-81-C-0003 F/G 4/1 NL





MICROCOPY RESOLUTION TEST CHART
NATIONAL BUREAU OF STANDARDS-1963-A

AD A137267

11-6301622

(12)

DNA TR-81-191

INTERPRETATION OF EXCDE: SPECTRAL AND AURORAL INFRARED SIMULATION DATA

PhotoMetrics, Inc.
4 Arrow Drive
Woburn, Massachusetts 01801

30 November 1982

Technical Report

CONTRACT No. DNA 001-81-C-0003

APPROVED FOR PUBLIC RELEASE;
DISTRIBUTION UNLIMITED.

THIS WORK WAS SPONSORED BY THE DEFENSE NUCLEAR AGENCY
UNDER RDT&E RMSS CODE B322081466 125AAXHX00010 H2590D.

DTIC FILE COPY

Prepared for
Director
DEFENSE NUCLEAR AGENCY
Washington, DC 20305

DTIC
SELECTED
S JAN 25 1984
J
B

83 12 88 002

Destroy this report when it is no longer
needed. Do not return to sender.

PLEASE NOTIFY THE DEFENSE NUCLEAR AGENCY,
ATTN: STTI, WASHINGTON, D.C. 20305, IF
YOUR ADDRESS IS INCORRECT, IF YOU WISH TO
BE DELETED FROM THE DISTRIBUTION LIST, OR
IF THE ADDRESSEE IS NO LONGER EMPLOYED BY
YOUR ORGANIZATION.



UNCLASSIFIED

SECURITY CLASSIFICATION OF THIS PAGE (When Data Entered)

REPORT DOCUMENTATION PAGE		READ INSTRUCTIONS BEFORE COMPLETING FORM
1. REPORT NUMBER DNA-TR-81-191	2. GOVT ACCESSION NO. DD-A137 267	3. RECIPIENT'S CATALOG NUMBER
4. TITLE (and Subtitle) INTERPRETATION OF EXEDE: SPECTRAL AND AURORAL INFRARED SIMULATION DATA	5. TYPE OF REPORT & PERIOD COVERED Technical Report	
7. AUTHOR(s) Irving L. Kofsky Malcolm T. Chamberlain Dennis P. Villanucci	6. PERFORMING ORG. REPORT NUMBER PhM-TR-82-04	
8. PERFORMING ORGANIZATION NAME AND ADDRESS PhotoMetrics, Inc. 4 Arrow Drive Woburn, Massachusetts 01801	9. CONTRACT OR GRANT NUMBER(s) DNA 001-81-C-0003	
11. CONTROLLING OFFICE NAME AND ADDRESS Director Defense Nuclear Agency Washington, D.C. 20305	10. PROGRAM ELEMENT, PROJECT, TASK AREA & WORK UNIT NUMBERS Task 125AAXHX-00010	
14. MONITORING AGENCY NAME & ADDRESS (if different from Controlling Office)	12. REPORT DATE 30 November 1982	
	13. NUMBER OF PAGES 96	
16. DISTRIBUTION STATEMENT (of this Report)	15. SECURITY CLASS. (of this report) UNCLASSIFIED	
	15a. DECLASSIFICATION/DOWNGRADING SCHEDULE NA since UNCLASSIFIED	
17. DISTRIBUTION STATEMENT (of the abstract entered in Block 20, if different from Report)		
18. SUPPLEMENTARY NOTES This work was sponsored by the Defense Nuclear Agency under RDT&E RMSS Code B322081466 I25AAXHX00010 H2590D.		
19. KEY WORDS (Continue on reverse side if necessary and identify by block number) Nuclear-Effects Simulation Upper Atmosphere Aircraft Measurements Nitric Oxide Excitation	Radiometry of Excited Air Spaceborne Electron Ejection Auroral Infrared Radiation	
20. ABSTRACT (Continue on reverse side if necessary and identify by block number) Nuclear infrared-backgrounds simulation data from excitation of the upper atmosphere by auroral particles and 3 kV electron beams from DNA/AFGL's EXEDE: Spectral rocket are analyzed and interpreted. The delay of 2.8 - 3.1 μm radiation output from >IBC II aurora calculated by a cross-correlation method from aircraft measurements by instruments with footprint <1 km has		

UNCLASSIFIED

SECURITY CLASSIFICATION OF THIS PAGE(When Data Entered)

20.. Abstract (continued)

an average value of 2 sec and (like the previously-measured energy conversion yields) appears to increase with the height of the maximum of the energy deposition rate profile. Fits of radiance data from moving arcs to a simple model of vibrational-bands emission from nitric oxide result in exponential predosing time constants between $1\frac{1}{2}$ and $2\frac{1}{2}$ sec, in qualitative agreement with current aerochemistry models.

Volume emission rate distributions of the blue-violet air fluorescence within 20 m of EXCEDE's accelerator were unfolded from radiometric photographs taken at characteristic ejection altitudes from onboard. This emission decreases very rapidly away from the rocket, and transverse to the beam axis fits a gaussian whose width first increases and then decreases. The measured excitation patterns, which cannot be fully attributed to outgassing from the vehicle, are interpreted in terms of a recent theoretical treatment of discharge initiation and electron heating resulting from an interaction between the charged beam and the local plasma it creates. The effects of such a collective process on feature radiances measured on upleg and downleg are discussed, and the altitude dependence of distance along the injected beam beyond which the secondary exciting-electron component no longer measurably affects the infrared radiation spectrum is estimated.

UNCLASSIFIED

SECURITY CLASSIFICATION OF THIS PAGE(When Data Entered)

SUMMARY

The objective of the work reported here is to interpret rocket and aircraft data on the infrared-optical radiations resulting from naturally-occurring and artificially-injected energetic particles that simulate excitation by atmospheric nuclear explosions. Photometrically-calibrated images from onboard of EXCEDE: Spectral's ejected electron beams and high-resolution auroral radiometry data from the Air Force Geophysics Laboratory's instrumented aircraft are considered. The field programs, performed by AFGL under Defense Nuclear Agency sponsorship, are described in Ref's 1,2,5 (EXCEDE) and 28 (the Test Plan for the aircraft-borne measurements).

The correlation between 2.8 - 3.1 μ m infrared emission from and particle energy input to the E region was systematically determined from fifteen of the highest signal/noise segments of data taken in or near the magnetic zenith in >IBC II aurora by coaligned radiometers having <1 km instantaneous projected footprint. The results apply to air parcels typically 30 km in height centered at altitudes determined by two-color photometry from the aircraft. Application of a standard cross-correlation method to the input and output data streams resulted in peaks in the correlation function that cluster near 2 sec, with individual values ranging between 0 and 7 sec. Like the previously determined (in Ref 1) energy conversion yield under steady-state bombardment, these lags in the SWIR emission give some indication of increasing with the height of the maximum of the profile of energy deposition by auroral electrons. This behavior and the magnitude of the delay are in qualitative agreement with the current model of excitation of overtone vibrational chemiluminescence from NO molecules by energetic particles from nuclear explosions.

Fits of a simplified input-output model were made to three data segments from isolated moving arcs, to whose rapidly varying energy input the results of the procedure are most sensitive. They indicated that the effect of pre-dosing on instantaneous SWIR yield decreases exponentially with time constants 1-1/2 to 2-1/2 sec, but failed to resolve the expected dependence of grow-in/decay time on mean energy deposition altitude. The lags show directly the temporal smearing of $2.8 - 3.1 \mu\text{m}$ sky backgrounds relative to particle energy input (whose distribution at past high altitude nuclear bursts is readily determined from photographs), and only somewhat less directly the attenuation of high spatial frequency components of the atmosphere's infrared radiance due to its wind shear and turbulence.

Volume emission rates of the blue-violet fluorescence of the air within 20 m of EXCEDE's electron accelerator were unfolded from the radiances measured from calibrated black-and-white photographs taken onboard the vehicle, for the purpose of assessing the effects on the spectrums of collective interactions of the electron beam and/or outgassing from the rocket. 78 millisec-exposure images from characteristic upleg and downleg altitudes, at the fixed injection current of 7 - 8 amperes, were selected for the evaluation. It was found that the volume emission distributions transverse to the beam's axis can be fit to adequate precision by gaussians. The pattern within ~5 m of the accelerator is almost independent of ambient air density between 128 km apogee and 110 km (and perhaps to lower altitudes); more radiation than predicted from independent-particle transport theory is present to at least 20 m, near which the initially-diverging beams appear to be refocusing (if this interpretation is correct they do not experience severe velocity spreading); and the volume emission rates are higher on upleg than downleg, more

so with decreasing rocket altitude (or increasing time between the measurements).

The spatial and altitude distributions cannot be fully attributed to outgassing of N₂ molecules from EXCEDE's payload and recovery system. We interpreted them following a recent preliminary model (Ref 20) of electron heating and initiation of discharges by an interaction between the beam and artificially-generated plasma. Intensities of ultraviolet, visible, and infrared features measured on upleg and downleg (not all of which have been extracted from the data) are shown to provide a further check on this model. The distances along the injection flux tube at which the electrons created and heated by the close-in discharge have little effect on air's infrared emission spectrum are estimated, and the value for 125 km is found to be in reasonable agreement with a ground-based measurement of the beam's radiance distribution. These ranges, whose precision can be readily improved by more refined calculations of the initial spectrum and transport of this secondary excitation source, apply in designing EXCEDE-concept simulation experiments in which the infrared radiation outputs are measured from remote (daughter) rocket platforms.

Accession For	
NTIS GRA&I	<input checked="" type="checkbox"/>
DTIC TAB	<input type="checkbox"/>
Unannounced	<input type="checkbox"/>
Justification	
By _____	
Distribution/	
Availability Codes	
Dist	Avail and/or Special
A-1	



PREFACE

This is a report of PhotoMetrics' second year's work under Contract DNA001-81-C-0003 on analysis and interpretation of atmospheric nuclear effects-simulation data taken for the Defense Nuclear Agency. The data are from the EXCEDE: Spectral electron-injection rocket (A51.970), launched 19 Oct 79 at Poker Flat Research Range, AK, and flights at auroral latitudes of the Air Force Geophysics Laboratory's NKC-135A infrared-optical aircraft 55-33120, in 1979-80. Earlier results from these field experiments are reported in Ref's 1 (the report of the first year's work on the program), 2, and 27.

The work was done under the direction of I.L. Kofsky. The authors express their thanks to R.R. O'Neil, E.R. Huppi (AFGL), D.H. Archer (Mission Research Corp.), J. Barrett, G.B. Parrent Jr (PhotoMetrics), and particularly K. Papadopoulos (University of Maryland) for providing useful information, and to Mrs. C.C. Rice for typing the manuscript. The encouragement of A.T. Stair Jr of AFGL and LtCol W. McKechnie and Dr. H.C. Fitz Jr of DNA is gratefully acknowledged.

TABLE OF CONTENTS

<u>Section</u>		<u>Page</u>
SUMMARY		1
PREFACE		4
LIST OF ILLUSTRATIONS		6
LIST OF TABLES		8
 1 VOLUME EMISSION RATES OF AIR FLUORESCENCE FROM EXCEDE: SPECTRAL		9
BACKGROUND		9
INSTRUMENTATION AND QUALITATIVE DESCRIPTION OF THE DATA		11
SELECTION AND INITIAL REDUCTION OF THE DATA		20
UNFOLDS		30
RESULTS		34
COMPARISON WITH PRELIMINARY MODEL RESULTS		43
LONGITUDINAL EXTENT OF THE EXCESS EXCITATION		48
A NOTE ON OUTGASSING		50
SUMMARY, CONCLUSIONS, RECOMMENDATIONS		53
 2 CORRELATION BETWEEN 2.8 - 3.1 μ m CHEMI- LUMINESCENCE AND PARTICLE ENERGY INPUT TO THE ATMOSPHERE		57
BACKGROUND		57
DATA		59
EXPECTED SPATIAL-TEMPORAL CORRELATION		63
DATA REDUCTION -- APPROACH		67
RESULTS -- EVALUATION		70
CONCLUSIONS		86
 REFERENCES		87

LIST OF ILLUSTRATIONS

<u>Figure</u>	<u>Page</u>
1. Spectral response of EXCEDE's short-pass filtered monochrome camera.....	12
2. H&D characteristic of the EXCEDE: Spectral film.....	13
3. Vignetting and distortion of the EXCEDE camera lens...	14
4. Altitudes of EXCEDE: Spectral frames selected for evaluation, with a diagram of the viewing geometry ...	24
5. Equi-density contour plot and print from frame at 127.8 km altitude on upleg (16169-3)	28
6. Scene radiance contour plot from frame at 127.8 km altitude on upleg	29
7. Gaussian fit to measured column emission rates at distance $D = 5$ meters from the accelerator, 127.8 km on upleg	32
8. Examples of small and large changes in inferred volume emission rate V_o on the beam axis and gaussian width parameter σ resulting from application of the sight path correction	33
9. Peak volume emission rate and gaussian width of the EXCEDE glow at altitude 127.8 km, upleg and downleg	35
10. Peak volume emission rate and gaussian width at 124.6 km upleg and 124.9 km downleg	36
11. Peak volume emission rate and gaussian width at 122.6 km upleg and 122.2 km downleg	37
12. Peak volume emission rate and gaussian width at 118.9 km upleg, and 118.8 and 119.7 km downleg	38
13. Peak volume emission rate and gaussian width at 109.8 km on downleg	39
14. Peak volume emission rate and gaussian width at 84.9 km on downleg	40
15. Altitude profiles of peak volume emission rate and gaussian width at three distances from the accelerator	42

LIST OF ILLUSTRATIONS (concluded)

<u>Figure</u>	<u>Page</u>
16. Altitude dependence of NO overtone emission yield in the 15 aircraft data segments	60
17. Schematic diagram of currently applied model of excitation of nitric oxide vibrational radiation by energetic particles	65
18. Cross-correlation and autocorrelation of the aircraft data	71-72
19. Cross plots of time and amplitude of maximum $C(\tau)$ against altitude of peak auroral deposition	74
20. Cross plot of time of maximum $C(\tau)$ against fractional solar illumination of the auroral profile	75
21. All-sky photographs of data segment 12's aurora ...	77
22. Radiometer and photometer traces of data segment 12's aurora	78
23. Chi-squared resulting from selection of τ_0 , n, and K, data segment 12	79
24. Best fits of SWIR predicted from model excitation function to radiance data, segment 12	80
25. All-sky photographs of data segment 3's aurora	82
26. Best fits of SWIR predicted from model excitation function to radiance data, segment 3	83
27. All-sky photographs of data segment 5's aurora	84
28. Best fit of SWIR predicted from model excitation function to radiance data, segment 5	85

LIST OF TABLES

<u>Table</u>		<u>Page</u>
1.	Identification of EXCEDE: Spectral Photographic frames selected for evaluation	25-26
2.	Velocities of the EXCEDE: Spectral rocket relative to the geometric field	45
3.	Observation and auroral parameters of 2.8 - 3.1 μ m band enhancements	62

SECTION I

VOLUME EMISSION RATES OF AIR FLUORESCENCE FROM EXCEDE: SPECTRAL

BACKGROUND

Evaluation to date of the onboard (Ref's 1,2) and ground-based (Ref's 3,4) photographs of the airglows excited by the 3 kV electron beam from EXCEDE: Spectral (A51.970, 19 Oct 79; Ref's 5,6) has shown their radiance distributions to be markedly different from those calculated assuming the energy deposition is by independently-acting particles (Ref 7), both within individual scenes and in dependence on the upper atmosphere's density. This finding has been interpreted as due to electric discharges from collective interaction of the charged sounding rocket and/or cold electron stream with the ambient and artificially-created ionospheric plasma (Ref 1, on the basis of Ref's 8 and 9). An important result of this interaction is that the number densities and energy distributions of the secondary electrons in the fields of view of infrared instruments on the vehicle differ substantially from those produced by individual charged particles (Ref's 10,11), such as are emitted from atmospheric nuclear explosions (β -rays, debris ions, secondary electrons of thermal x-rays and λ -rays). As these secondary electrons efficiently excite vibrational states of pre-existing molecules (principally, CO₂ and its precursor N₂, and H₂O) and also play a part in the aerochemical processes that create new infrared-active species (NO, O₃, NO⁺, others), the difference in energy spectra would introduce errors in scaling EXCEDE's radiometry data to infrared sky background intensities in nuclear warfare.

The presence of enhanced fluxes of secondaries in the beam was further indicated by unexpectedly high radiances in

several of the ultraviolet, visible, and infrared molecular band systems of air that have high optical cross-sections for excitation by low-energy electrons, as was detailed in Ref 1. (While some aspects of the spatial and altitude dependence of photographic brightness might appear due to molecules outgassed from the rocket body -- on which more presently -- outgassing can not explain the spectral ratios of N₂ emission features.) Furthermore, qualitatively similar visible-radiation patterns have been reported from other injections of ~1-10 keV electrons into both the thermosphere and low-pressure air in laboratory tanks, as also discussed in Ref 1 (more recent observations are in Ref's 12 and 13). The optical data, along with data on radiofrequency-wave emission (oscillating electric fields heat the electrons), plasma density and temperature, and neutralization of spaceborne accelerators, have brought forth a body of thought on collective interactions of the charged beam and rocket with the surrounding atmospheric plasma (as reviewed in Ref's 9, 13, and 14; see also Ref 15).

The purpose of analyzing EXCEDE: Spectral's radiometric photographs can be stated as determining the distance from the ejection rocket beyond which the effect of secondary electrons from any collective processes on the infrared chemiluminescence and fluorescence spectrums can be neglected or reliably corrected for. That is, the work reported here is intended to characterize the plasma heating (if any occurs) only to the extent required to assess its interference with the simulation of nuclear particle-excited sky background radiations and processes. This information about spatial distributions of short-wavelength visible air fluorescence is intended 1) for interpreting existing EXCEDE: Spectral optical/IR data and 2) for designing experiments in which the infrared sensors view excitation of particle beam-excited air from

daughter platforms spatially separated from the mother (accelerator-carrying) vehicle.

Up to now, evaluation of these photographic images (Ref's 1,2,13 (p217 ff)) has consisted of determining the glow's surface radiance distribution as projected to the wide-angle camera, from five rocket altitudes. In the present work, we have systematically computer-reduced images at a series of upleg and downleg altitudes with a fixed injected current to volume emission rates within ~20 meters from the electron accelerator. These represent the "fundamental" physical quantity in the film data, as they measure the volume rates of excitation of N₂ molecules by beam and secondary electrons and thus the sum of products of excitation cross-section and flux of these particles. The longitudinal variation of this excitation measures the extent of the interaction-and-discharge region, and its width transverse to the beam axis provides further information on the behavior of the beam and plasma.

INSTRUMENTATION AND QUALITATIVE DESCRIPTION OF THE DATA

The rocket's photographic system of one 16 mm camera filtered for sensitivity to blue and violet fluorescent radiation coaligned with a similar unit with 3-layer color film (in effect, Ektachrome) is described in Ref 1; for completeness, we review the fast monochrome camera's pertinent characteristics and calibration here. Figure 1 shows its spectral response, Figure 2 the diffuse transmission density-log exposure (H&D) characteristic of its black-and-white film measured with the same short-pass filter (Schott BG-12 colored glass) in the sensitometer as was used in the camera, and Figure 3 the intensity vignetting and geometric distortion of its lens. The camera images a 62° x 94° field onto the 7.64 x 12.0 mm film frame, with the long dimension in the direction of the ejected electron beam (refer to the photo-

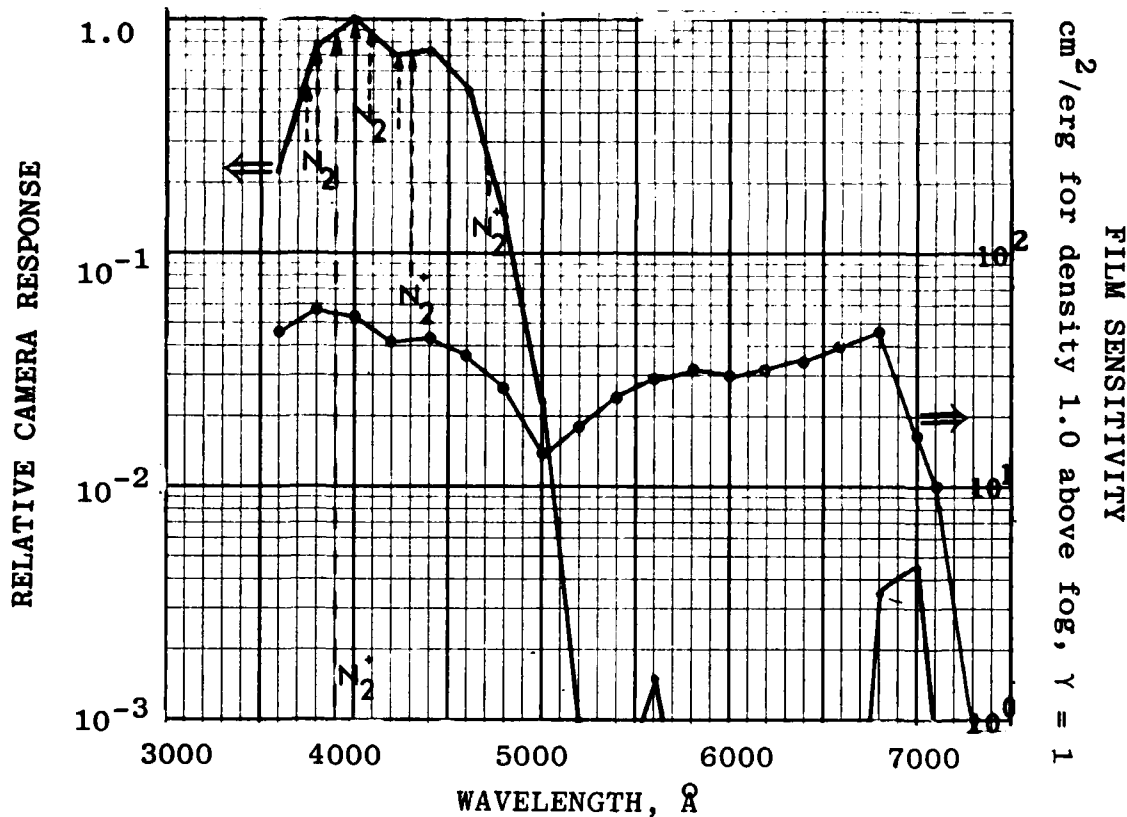


Figure 1. Spectral response of the EXCEDE camera and film. The sharp falloff above 4600 Å results from the attenuation by its BG-12 Schott filter, and its response at wavelengths below 3900 Å is limited by lens absorption. The lengths of the dotted lines are roughly proportional to the relative intensities in an EXCEDE spectrum at 74 km rocket altitude (see text).

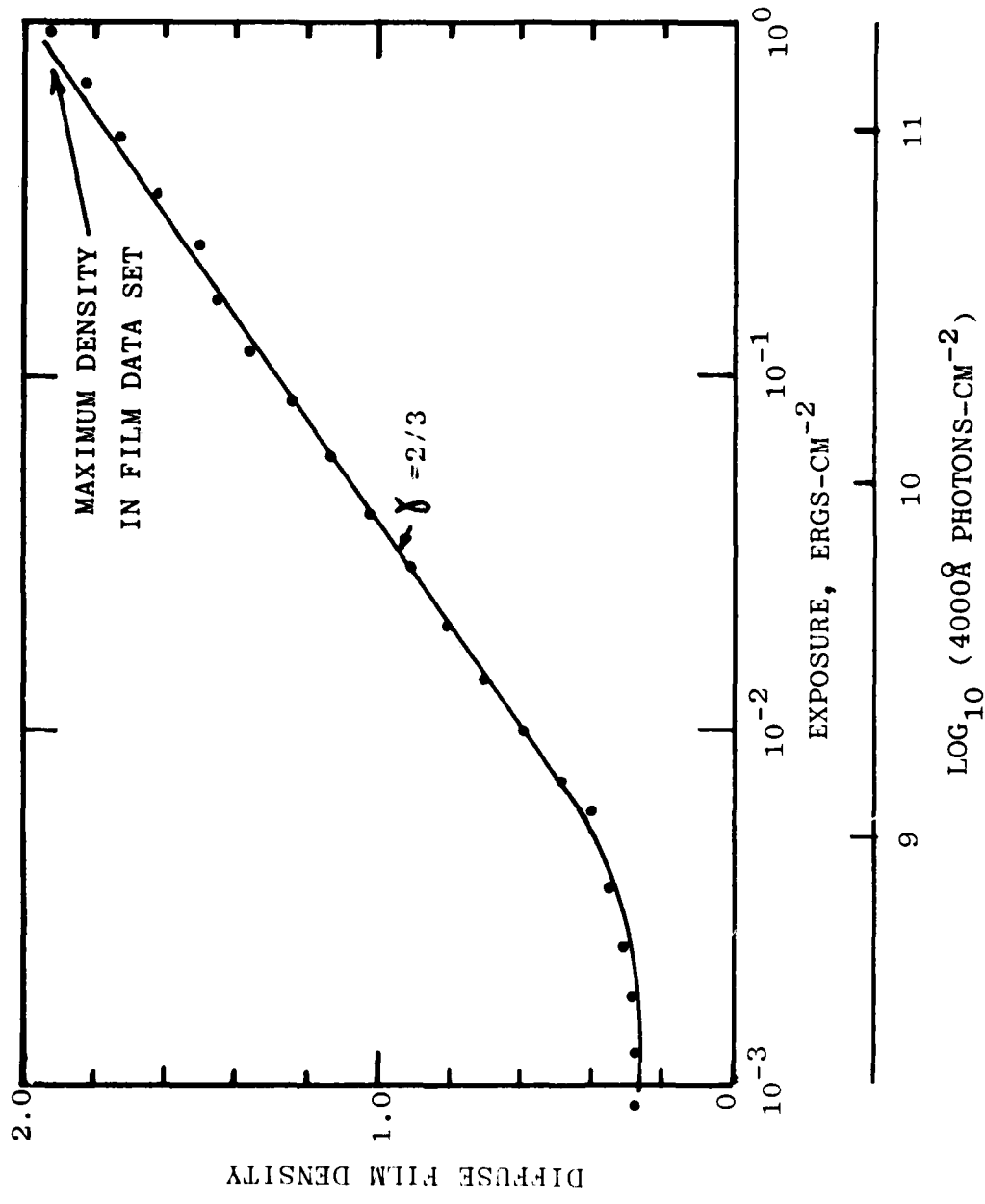


Figure 2. H&D response characteristic of the black-and-white film, measured in blue light.

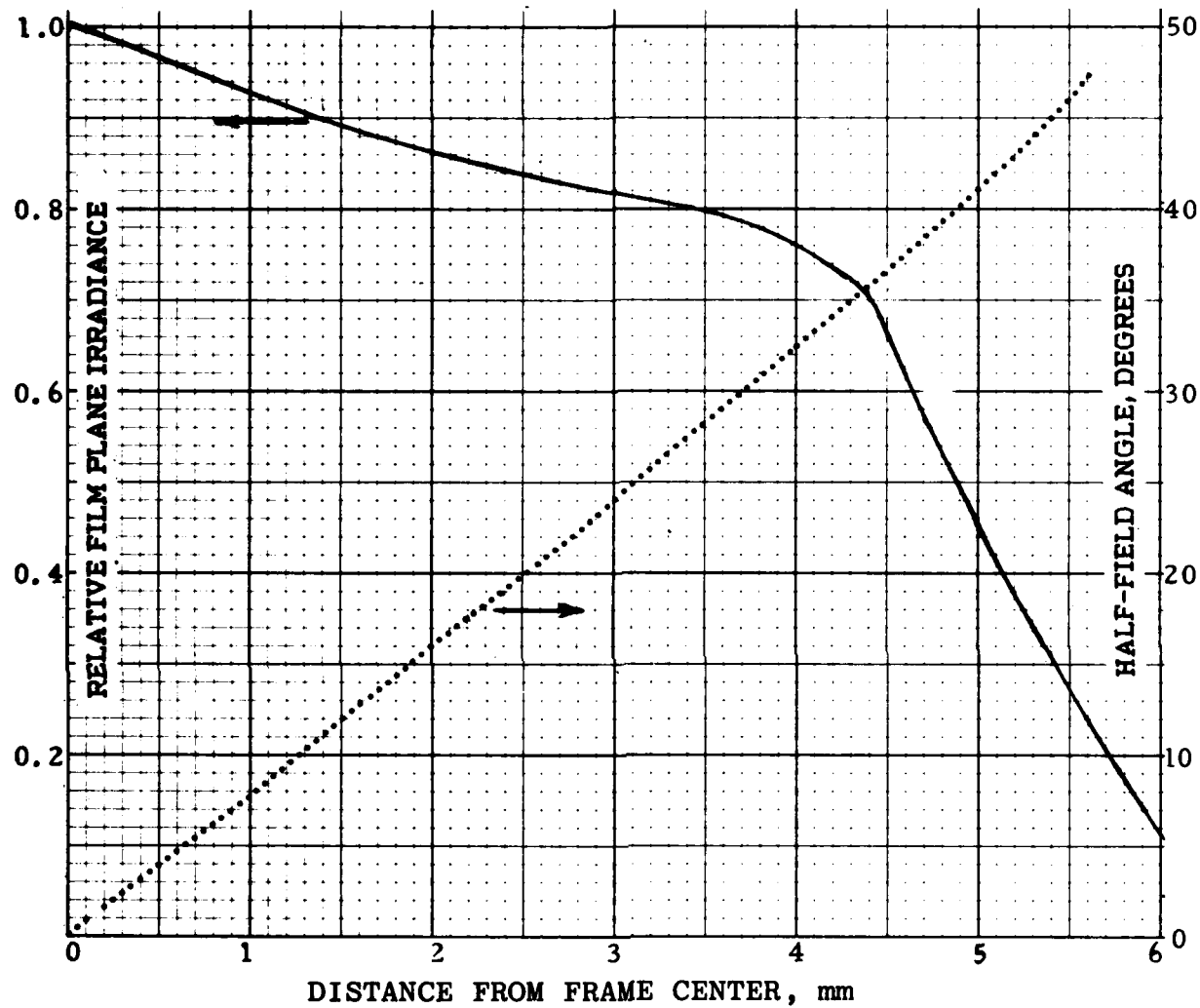


Figure 3. Measured relative irradiance in the image (solid line) and field-of-view half-angle (dotted line) as a function of displacement of image points from the field's center. These lens vignetting and distortion data are applied in converting the film density distributions to scene radiance distributions.

graphs and isophote plots in Ref's 1 or 13) and the diagonal sharply truncated beyond $\sim 105^\circ$. Points 1/2 m away from the lens are in focus to within the image's $\sim 1/3^\circ$ circle of confusion. Continuous sequences of 8, 78, and 800 millisec exposures were made, uncoordinated with the programming of EXCEDE's electron accelerator pulses.

Fig 1 also shows the relative intensities of N_2^+ First Negative ($B \rightarrow X$) and N_2 Second Positive ($C \rightarrow X$) band intensities measured by EXCEDE's visible-sensitive spectrometer at 73 km downleg altitude (p 28 of Ref 5). Within the camera's passband this published spectrum is sensibly that of intense aurora (Ref 16) and of ionizing radiations from nuclear explosions depositing energy at altitudes between 55 and 125 km. Under conditions that the glow excited by the beam has this emission spectrum, about 62% of the actinic exposure is due to the N_2^+ 3914 Å (0,0) band, another 14% is from the 4278 Å (0,1) band, and 16% is from the N_2 Second Positive bands. Where the population of electrons in the camera field with energy above the 11.03 eV threshold for exciting N_2 's C state is enhanced (relative to that resulting from impact of primary electrons), the Second Positive system makes a larger relative contribution. (The threshold for exciting the B state of N_2^+ is 18.74 eV.)

Such a change in EXCEDE's emission spectrum is evidenced by the magenta color outward from the apparent beam axis, which is due to excitation of N_2 's violet-blue $C \rightarrow X$ and red $B \rightarrow X$ (First Positive) triplet-state bands by laterally-scattered secondary electrons. (Refer to the schematized cross-sections in Fig 17 of Ref 2.) This emission of course also overlies the central whitish-blue "core" region, as the beam Coulomb-scatters secondaries at all azimuths. We have not yet analyzed the color film (which has virtually the same high signal/noise and overall data quality as the black-and-white film)

to ascertain what information about the secondary-electron spectrum is contained in this purplish component of the photographic radiance pattern.

In any case, since the camera has a relatively wavelength-insensitive response (Fig 1) only a small change in its radiometric calibration results from any such changes in the glow's emission spectrum. As was shown in Ref 1, application of the fluorescence spectrum of air in the E-region (which as noted is closely similar to the published low-altitude EXCEDE spectrum) shows that the effective exposing wavelength is about 4000 Å in the "core," and the known cross-sections for excitation of Second Positive bands by the secondaries indicate that in those regions where the color film is magenta it is about 3900 Å. The camera's spectral sensitivity differs by only 12% over this narrow wavelength range. In assigning the absolute calibrations in Fig 2 we corrected the film's response to the sensitometer's illumination spectrum to its response to 4000 Å photons. Since the onboard spectrometer's field of view encompasses the core its spectra give the actual relative contribution of First Negative and Second Positive band emission to the photographic signal at all ejection altitudes, in that central area of film image where the color remains substantially constant. (These spectra have not yet been published.) In summary: the measured total number of photons emitted per unit volume of glow will change only slightly with its emission spectrum, but where the fluxes of 11-~19 eV secondary electrons are enhanced the N₂ Second Positive system contributes more than the aforementioned fraction of the radiation signal.

The camera's absolute radiometric calibration is subject to a systematic error at low exposures due to uncertainty in transmission of blue light by the more optically dense area of the sensitometer's step tablet. This error is a maximum of 25%

near the toe of the film's response characteristic and becomes negligible when the film-plane exposure reaches 1×10^{-1} erg/cm². Note (Fig 2) that the film's contrast γ is essentially constant between the maximum exposure recorded and $\sim 10^{-2}$ erg/cm². This latter exposure results from low scene radiances, of the order of 1/2 erg/cm²-sec-sterad (1 megarayleigh), and as previous isophote plots (in Ref's 1 and 2) show the glow brightnesses drop to this level only well outside the flux tube into which the electron beam is injected. Thus the fractional uncertainty in radiance introduced by microdensitometry errors and digitization noise, which is $\log_{10} x \times (\text{density error})/\gamma$, changes little over most of the glow's image. Where the density error is 0.05 units, this radiometry error would be 17%.

A further systematic error at all exposures is due to uncertainty in the lens's transmission of axial rays, and a small and scene angle-dependent error results from uncertainty in the transmission of the blue glass filter. Still further radiometric error is introduced by imprecision of the correction for vignetting by the camera's wide angle lens (Fig 3), which becomes large toward the edge of its field of view. Considering these and other potential errors noted in Ref 1, we estimate the absolute brightness measurement accuracy to be within a factor ± 1.5 at the geometric center of the image, and less than a factor 2 at the extremes of the frame within ~ 2 m from and beyond ~ 15 from the rocket body. Absence of any unforeseen large error in the film radiometry is evidenced by the agreement between the photographic radiances 4-1/2 m down the beam and those measured in essentially the same projection by a 3914 Å-band photometer in the payload (Fig 16 of Ref 2, from yet-unpublished data).

Lens distortion causes radiation originating at large angles α to image at angles β (both measured from the principal points of the lens). This small effect was taken into account by incorporating into the computer reduction

the measured relation (in Fig 3) between position on the film image and direction in object space. Offset of the lens axis from the geometric center of the film frame can be seen to be less than $150\mu\text{m}$ in the long dimension of the frame -- that is, the direction of the beam --, as is shown by the position of the edges of the circular image. Misalignment transverse to the beam would have only second-order effects on the results of the analysis, and insofar as the film advance is pin-registered any photogrammetry errors would be systematic throughout the data set. Timing error is negligible, as each photographic image can be directly identified with accelerator operation conditions and rocket altitude.

The camera viewed toward the electron beam from 3-1/4 m north of the anode of the accelerator that operated over most of the flight, with its optic axis in the plane defined by the injection field line and the rocket's long axis. The projection direction moved to 21° east of the meridian when the rocket's azimuth was changed just after apogee to align the payload with the trajectory so as to increase its instruments' sight paths through irradiated air; this causes the image of the glow to tilt to the right (northwest) on the downleg frames. A side view of the camera's field, the ejected beam, and the location of these instruments -- whose fields intercept the beam axis 4-6 m outward from the accelerator -- is in Ref 1, and a simplified diagram appears in Figure 4.

Image positions of some points on the beam's axis are

1.5 m from the accelerator, near the bottom edge
of the frame (limit of camera fov);

1.8 m, the line from the camera lens is per-
pendicular to the axis;

4.4 m, center of the image, the vector from the
lens makes a 45° angle with the axis;

20 m, 4-1/2 mm above the center of the image,
the vector from the lens makes a $8-1/2^\circ$
angle with the axis.

The direction at which the finite-width beam appears to converge at infinity lies within the frame. We have so far extended the film data analysis to 20 m along the beam from the accelerator, as the physical properties of the glow do not seem to change substantially beyond about 8 m -- although there is now evidence of a refocusing node -- and the foreshortened perspective (and secondarily, imprecise vignetting correction) introduces increasing error into the unfolds of the radiance distributions. Specifically, the sight path that intercepts the beam axis at 20 m passes through the "edges" of the emitting region at distances ~10 and 30 m from the accelerator; although the column emission is weighted toward the axis, this oblique projection may be the reason that no obvious beam refocusing node is seen in the surface radiance. (The first node is at 21 m in the magnetic field over Poker Flat Research Range, where EXCEDE: Spectral was conducted.) The method adopted for correcting the nominally radially-symmetric volume emission rates for these off-perpendicular projections is described later.

Exposure of the negative is within its dynamic range, and the photographs are otherwise of good quality, at all ejection altitudes. Characteristic frames are reproduced in montages in Ref's 1 and 13. The images show that sensibly all the emission in the field of view, which intercepts the beam axis 1-1/4 m out from the rocket body, comes from within ~2 m from the injection flux tube. That is, no general dc corona glow surrounding the rocket and outside the beam area proper, such as might be ignited by energized ionospheric electrons returning to charge-neutralize the vehicle (Ref 15), is detectable. Analysis of the complementary groundbased images for ~125 km rocket altitude showed that the transverse-integrated radiance along the field-confined beam also lies above predictions of an independent-particle energy-

dissipation model between ~40 m (their nominal spatial resolution) and 400 m from the accelerator (Ref 3). On the other hand the end-point range of the beam does not appear substantially different from what is expected (although this issue has not been addressed quantitatively; refer to Ref 17), which would indicate that no major discrete change in the energy distribution beam of the electrons can be occurring near the accelerator.

When the rocket is above ~100 km the negatives show a broad bright area extending about halfway up the frame, from which extends an apparently-narrower region whose longitudinal increase in brightness is at least qualitatively consistent with the increasing sight path. In retrospect this wider area can be seen to be associated with the unexpectedly steep increase in glow brightness toward the rocket within the first ~5 m, which is shown in the isophote plots and Fig 16 of Ref 2. As we will see, the broadening turns out to be a photographic-thresholding and perspective effect, since the halfwidths of surface brightness and volume emission rate in the glow actually decrease toward the rocket (closer than ~10 m from the accelerator). The lack of clear dependence on ambient density of the axial radiances in this close-in region over a two order of magnitude range in density is one of the more noteworthy aspects of the data; the emission is by and large consistent with some near-constant fixed fraction of the beam's kinetic energy being absorbed in this region.

SELECTION AND INITIAL REDUCTION OF THE DATA

We selected 19 of the ~270 useful black-and-white film images for analysis, on the basis of the following criteria. The set includes the five frames previously manually reduced to equi-radiance contour plots and reported in Ref 2; these were re-run ab initio to ensure that the same standard micro-

densitometry procedures were applied to all data.

- 1) Constant ejected current (and voltage) from a single electron accelerator unit. This choice eliminates dependence of the photographic radiation yields on beam energy, and furthermore maintains a fixed viewing geometry. (EXCEDE's four accelerators were spaced 50 cm apart in a line at the same rocket azimuth as the cameras.) In practice unit #4, most favorably sited farthest from the lens, injected 7 to 8 amperes over most of the flight; the other units operated sporadically. Some information on the volume excitation rates' dependence on beam current, which although apparently not needed for interpreting EXCEDE: Spectral's infrared radiometry data would be useful for qualifying future high-current injection concepts, can be derived from analysis of other of the photographic frames.
- 2) Pairs of frames at the same altitude (to within ~40% in ambient air density) on upleg and downleg. This choice serves to investigate the effects of the ejected beam's dwell time on individual flux tubes (which depends on the rocket's velocity relative to the irradiated volume) and outgassing from the vehicle (which would be expected to decrease with time after launch).
- 3) Ejection-altitude increment less than a scale height of N_2 , ~7-8 km. Significant changes in the energy distribution pattern might be expected over factor-e changes in the ambient gas density.

4) Constant film exposure duration, 78 millisec.

This limitation removes any variability due to the camera's integration time. We note in passing that the correction for reciprocity failure of the film (the difference in effective exposure among the 8, 78, and 800 msec frames) introduces only negligible error.

Besides not considering the radiation pattern from injection of 21-24 amperes (3 accelerator units in operation), the data set selected does not address the questions of variations between adjacent short-exposure frames or long and short exposures. As the aforementioned photometer data show no erratic 10's millisec-scale variability when the accelerator current and voltage remain constant over the 2-4 sec ejection pulses, reducing adjoining frames would determine the precision of our radiometric photography. The fact that the only discernible change in the photometer signal over these injection periods can be ascribed to increasing or decreasing air density leads to the expectation that the spatial radiance distributions measured in long and short film exposures would be similar.

No particular effort was made to match the onboard frames to time exposures from the groundbased cameras (Ref 5). (These provide a second projection of the glows with spatial resolution much poorer close to the rocket but far better beyond ~40 m.) This is because the limited number of high-quality ground photographs available would restrict the selection, and in any case continuous low light level video images exist (Ref 17). We note that a video camera was operated onboard EXCEDE: Spectral, which due to what appears to be its restricted dynamic range returned very little useful information (Ref 5).

The above data-selection conditions were met for altitudes above 116 km, where one upleg accelerator #4 achieved relatively stable operation. An additional altitude-matched pair results from inclusion of (one of) three upleg frames starting at 106 km during which the same unit emitted brief pulses. These images provide some scaling to lower injected currents, but have poorer signal/noise because of their generally lower optical densities. (They have been reduced but not yet analyzed.) Frames meeting conditions 1) and 4) are available at 110, 98, and 85 km on downleg; these are separated by almost two, rather than the desired less than one scale height. In addition we included two 8 millisecond frames at 79 and 74 km, during which accelerators #1 and #3 respectively were operating; this shorter exposure keeps the film densities on scale at the higher air densities. The anodes of these two accelerators are 1-3/4 and 2-3/4 m from the lens, and the camera's field extends to within 5/8 m of #1 (refer to Fig 12 of Ref 1). (These also are not yet evaluated, as they have a different photogrammetric scale than the other frames, the payload's orientation has changed, and the end-point or "practical" range of 3 keV electrons at this altitude is only about 2 m.) Rocket altitudes at the 19 frames analyzed are shown in Figure 4, and identifying data for them are listed in Table 1.

The roll of 16 mm EK2475 film had been processed in a reel tank using agitation known to result in spatially-uniform development. Transmission density distributions in these frames and of the calibration step tablets that had been previously exposed onto the film (as described in Ref 1) were read onto seven-track digital magnetic tape by our scanning microdensitometer, with a 150 μ m square aperture sampling in a rectangular raster on a 48 x 50 μ m grid. This oversampling results in approximately 43,000 run-length coded density points per film frame. The digitization increment is about 10% in

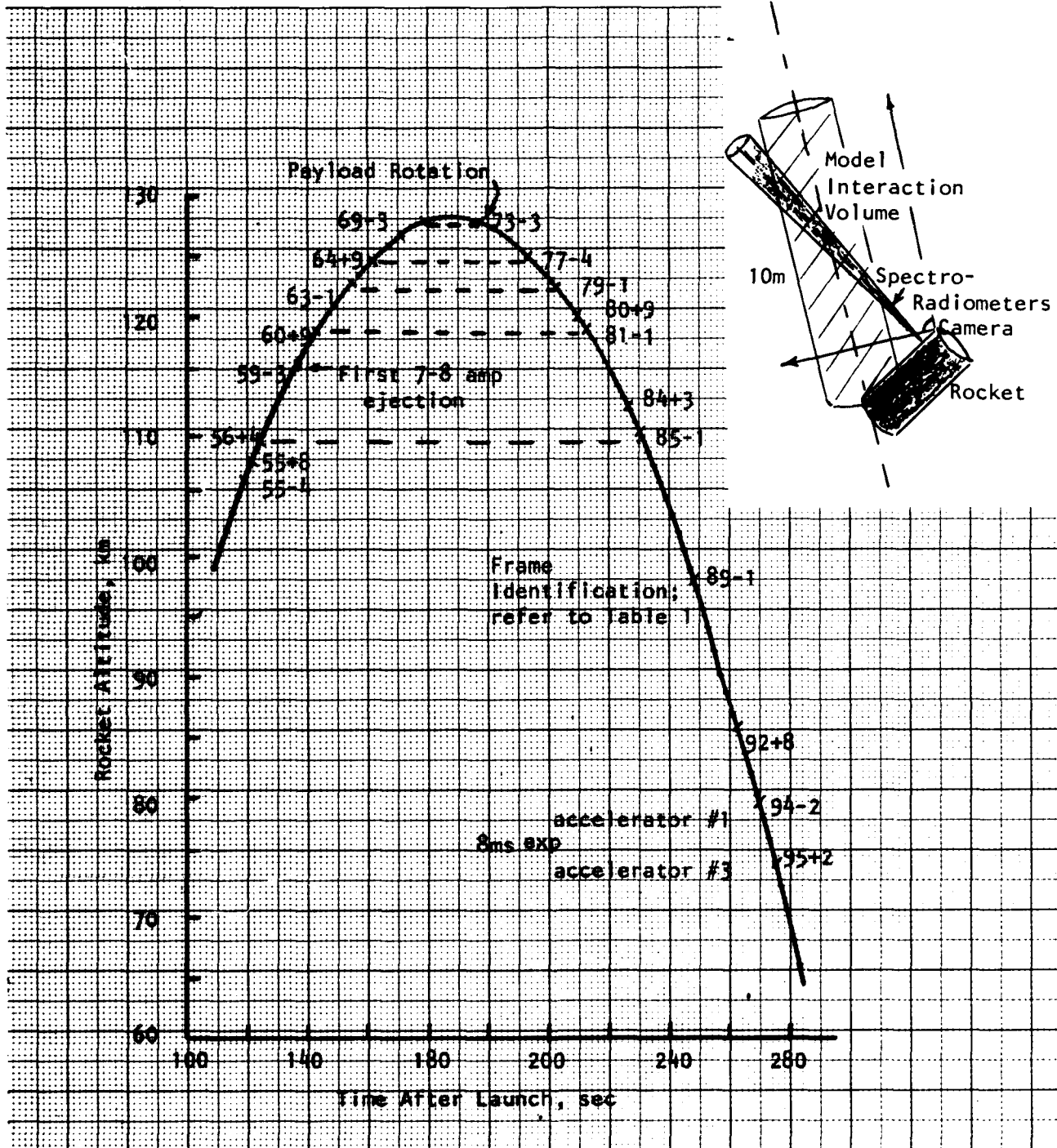


Figure 4. Altitudes of EXCEDE: Spectral 78 msec-exposure photographic frames selected for evaluation. The electron accelerator ejects the first 7-8 ampere beam at 116 km on upleg. The diagram at upper right is a side view, to scale, of the camera and other instrument fields and (Ref 20) model beam interaction volume.

Table 1. Identification of EXCDE: Spectral photographic frames selected for evaluation

TAPE CT5020 12 Feb 1982 Wedge F

1. 16163-1 153.2 sec 122.6 km upleg
2. Step tablet 2, 3 scans step 19, 2 scans each steps 18-1
3. 16159-3 136.0 sec 115.7 km upleg
4. 16184+3 246.5 sec 111.8 km downleg
5. 16189-1 267.9 sec 97.7 km downleg

TAPE CT5010 17 Feb 1982 Wedge F

1. 16192+8 aborted
2. 16192+8 283.3 sec 84.9 km downleg (accelerator turned off during exposure)
3. 16164+9 160 sec 124.6 km upleg
4. 16177-4 214 sec 124.9 km downleg
5. 16169-3 179 sec 127.8 km upleg
6. 16173-3 197 sec 127.8 km downleg
7. Step tablet 1, 2 scans each of steps 19 through 6

TAPE CT5070 26 March 1982 Wedge F

1. 16160+9 143 sec 118.9 km upleg
2. 16179-1 223 sec 122.2 km downleg
3. 16180+9 230 sec 119.7 km downleg
- empty file
4. 16181-1 faulty, aborted
5. 16181-1 232 sec 118.8 km downleg
6. Step tablet 2, 2 scans each of steps 18 through 1

TAPE CT5000 29 March 1982 Wedge F

1. 16185-1 250 sec 109.8 km downleg
2. 16194-2 289.8 sec 78.9 km downleg (8 msec, accelerator #1 only)
3. 16195+2 295.0 sec 73.7 km downleg (8 msec, accelerator #3 only)
4. Step tablet 2, 2 scans each of steps 19 through 1

TAPE CT5060 31 March 1982

1. 16156+4 124.2 sec 109.3 km upleg, short accelerator pulse, wedge D
2. 16155+8 120.7 sec 107.2 km upleg, short accelerator pulse, wedge D
- empty file
3. 16155-4 118.4 sec 105.7 km upleg, short accelerator pulse, wedge D
4. Step tablet 3, 2 scans each of steps 14 through 1, Wedge D
5. 16154+4 115.8 sec 104.0 km upleg, short accelerator pulse, wedge A. Very noisy, no calibration

Explanatory Information for Table 1.

Table 1 lists the frames digitized from the black and white 16 mm EXCEDE: Spectral film onto five separate magnetic tapes. These data were later transferred to one labeled multi-file data set on half inch 7-track magnetic tape at the AFGL Computer Center. The frame identification scheme used here is derived from the film footage numbers appearing on the film edge. As these footage numbers each span two frames, each number is allocated to that frame adjacent to the least significant digits, e.g., frame #16163 identifies the frame adjacent to the digits 63. Frame #16163+5 is five frames from that position in the direction of increasing footage numbers, and Frame #16163-3 is three frames from 16163 in the direction of decreasing footage numbers.

All the photographic step tablets used for calibration were exposed with PhotoMetrics' sensitometer set on Stop 1024, through a Schott BG-12 filter. Tablet 1 is a 1 sec exposure, 2 is 1/15 sec, and 3 is 1/125 sec. Wedges F and D are continuous density reference scales incorporated in the microdensitometer. Their density quantization steps are 0.032 and 0.025 units respectively.

The data on the labeled multi-file tape are stored in their original form; no decoding was done prior to recording on this tape. Each data file, i.e., each digitized image, is stored as a separate file with a unique label. All files actually containing any information on the original tapes were loaded onto the labeled tape. These included one run aborted during digitization (on CT5010) and another which was believed to be faulty and so repeated (on CT5070). Any empty files, for example those formed by consecutive end-file marks on the original tapes, were removed during transfer to the labeled tape; these empty files are indicated in Table 1.

The labeled tape is identified by the number OS0762 and the system of labeling individual files is illustrated by the following example,

Label EX264 is derived from:

EXCEDE

26th March 1982 -- digitization date

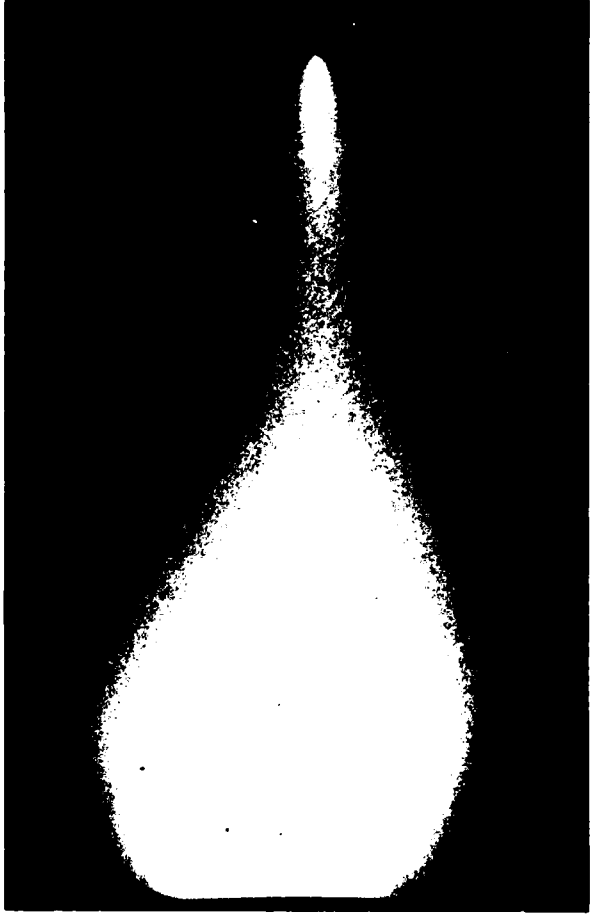
4th image digitized on 26 March 1982.

Individual data images may be accessed and copied to disk files for analysis by procedures described in the Control Data Corporation NOS/BE system manual under the general heading of labeled multi-file tapes.

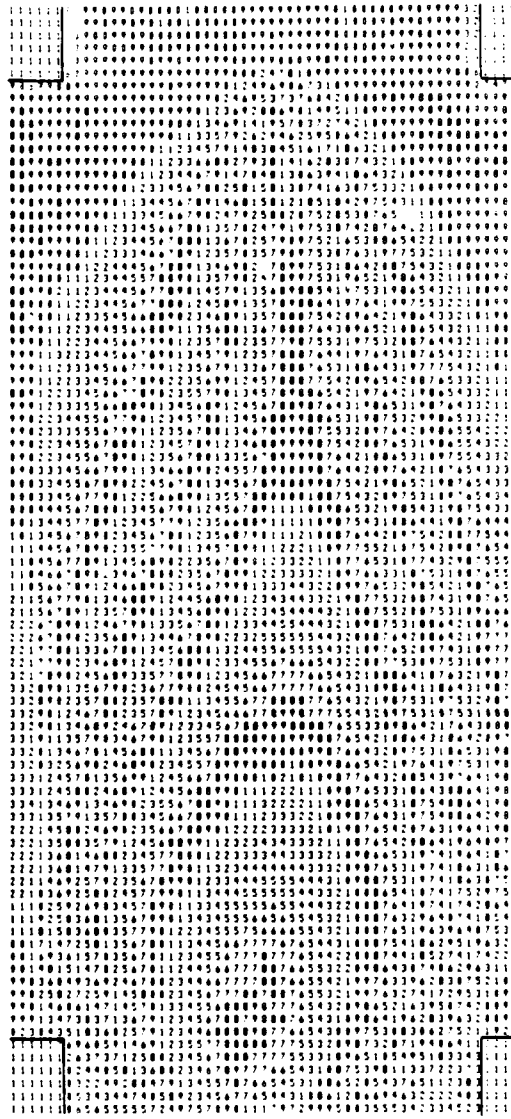
scene radiance over most of the image. Frame edges were aligned parallel to the microdensitometer's scan direction to within one scan line advance by reference to edges of the sprocket holes. These holes, besides establishing the angular orientation of the images, also were used to determine the frame centers, which as noted align with the optic axis of the lens in the long dimension of the frames to less than one scanning slit width.

Software was written for reducing this film density file using AFGL's CDC-6600 digital computer. Programs access and identify the densities, convert them to scene radiances with the view angle-dependent correction for lens vignetting (this had been done manually for the isophote plots reported in Ref 2), and determine axial and radial distributions of volume emission rate using the unfold method described below. Approximately 10 sec of central processor time is required to decode the data file to access one photographic frame, 2 sec to locate its center, and 30 sec to compute a set of volume emission rate distributions in ten cuts through the glow transverse to its long dimension.

Fig's 5 and 6 show 2-D plots of raw film density and scene radiance before and after the vignetting correction, for a typical frame. Only one-ninth the number of data points actually used in the film evaluation are retained for this display. Note (Fig 6b) that straight lines perpendicular to the beam axis and the view direction generally map onto the image plane as curved lines; in addition equally spaced sampling points in perpendicular cuts are unequally spaced along these lines. As the viewing directions computed for individual steps in the transverse scans do not in general correspond exactly to positions of digitized data points in the film plane, we devised a simple interpolation scheme to determine radiance at the desired image position from its four immediately-surrounding stored data



(a)



(b)

Figure 5. Equi-density contour plot (b) and print (a) from frame at 127.8 km on upleg (identification 16169-3). The least significant digit of the optical density code (integers 0-63) is printed. The astigmatism in the computer plot results only from the character spacing of the printer and in no way affects the data analysis.

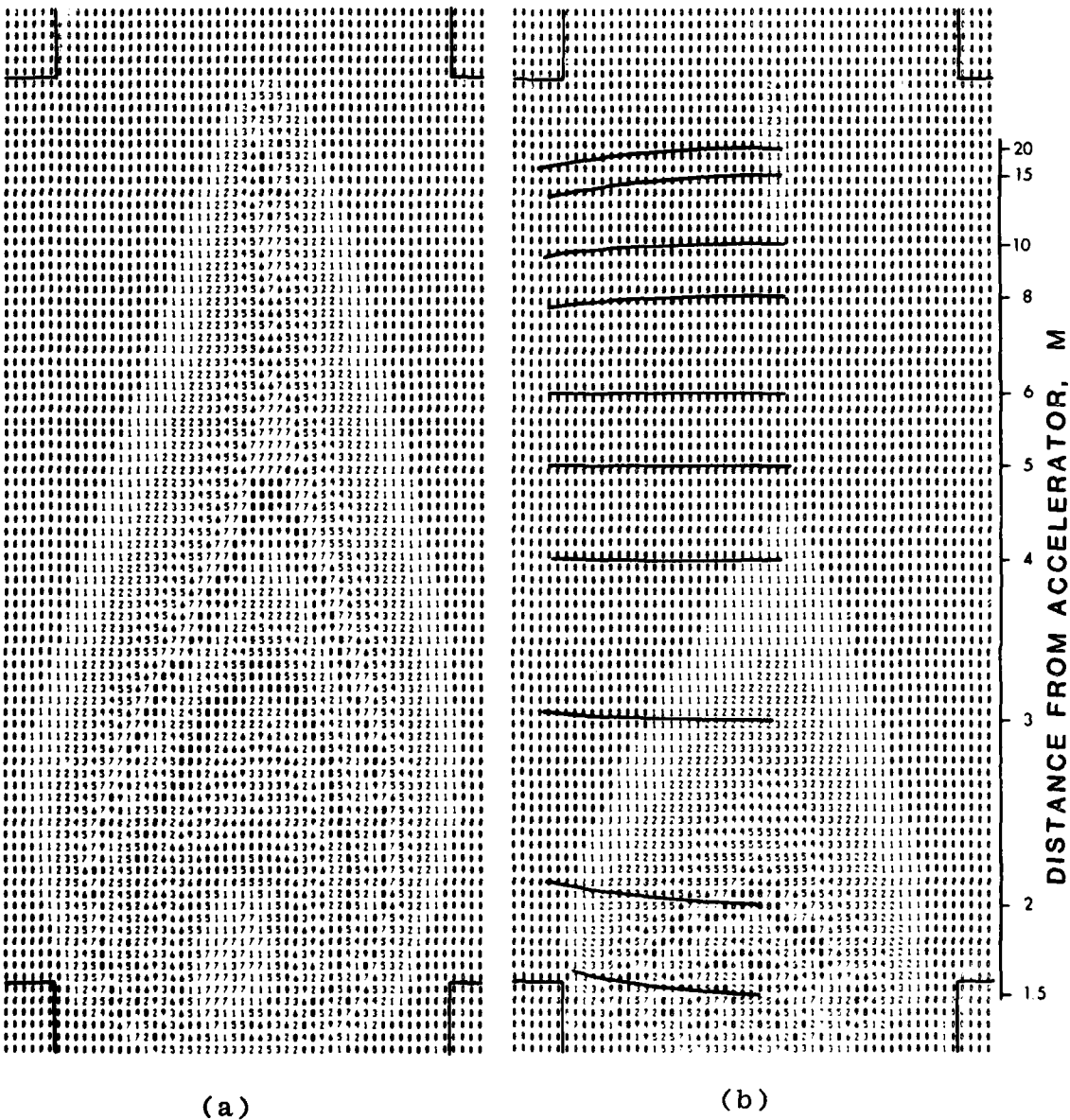


Figure 6. Uncorrected (a) and corrected (b) scene radiance plots from frame at 127.8 km on upleg (16169-3). The least significant digit of the radiance code is printed. The ten lines indicate projections perpendicular to the geomagnetic field-aligned beam axis.

points. This procedure also smooths the quantization noise inherent in the original digitization.

UNFOLDS

The cylindrical symmetry and optical thinness of the radiation patterns allows their volume emission rates to be unfolded from their surface radiance distributions. Column emission rate $B(x)$ at points intercepting the symmetry axis at transverse distance x -- the measured quantity -- is related to volume emission rate $V(r)$ at radial distance r from the symmetry axis by

$$B(x) = 2 \int_0^{r'} V(r) r(r^2 - x^2)^{-1/2} dr,$$

where V goes to zero at $r = r'$. This is Abel's integral, and inverts to

$$V(r) = \pi^{-1} \int_{r'}^{\infty} (dB/dr) (x^2 - r^2)^{-1/2} dr.$$

We extracted linear arrays of column emission rate $B(x)$ at ten ranges D along the beam axis from the electron accelerator from each each two-dimensional image brightness array (such as Fig 6b), increasing x in equal increments in object space.

We first attempted to fit B with sets of third- or fourth-order polynomials, which allows Abel's integral to be solved analytically (see, for example, Ref 18). The line data sets were organized into seven-point segments with a three-point overlap at each end, for which coefficients of x^m were calculated by a least-squares method. This standard procedure was found unable to smooth the occasional large (~20%) fluctuations in radiance, as was evidenced by persisting and unsystematic spatial structure in the unfolds. This appears to be because polynomials tend to follow large excursions. Little if any improvement was effected by varying the segment length or by prior smoothing using three-point weighted averages.

As the transverse radiance distributions look to be roughly gaussian in shape -- see, for example, Fig 21 of Ref 1 -- we

substituted fitting by single gaussian functions. This turned out to result in reasonable fits to the experimental distributions, as evidenced by chi-squared tests (as prescribed in Ref 19 (see also Section 2); the chi-squared or residual for unweighted data is calculated in conjunction with each least-squares fit). Figure 7 shows a computer fit to one of the measured line radiances in Fig 6b. Note the two errant data points at high film exposure, which we believe to be the source of the unsuitability of the more general polynomial fitting method. A gaussian offers the further advantage of characterizing the distributions with two readily-recognizable descriptors, peak surface radiance B_0 (or volume emission rate V_0) and width parameter σ .

Straightforward unfold of a gaussian radiance having full width at half-maximum 2.354σ gives the result that the volume emission rate at radius r is

$$V = (2\pi\sigma^2)^{-1/2} B = (2\pi\sigma^2)^{-1/2} B_0 \exp(-r^2/2\sigma^2).$$

The assumed-constant background in the radiance pattern (see Fig 7) is removed by our fitting and unfold procedure. Note that the brightness and volume emission patterns have the same halfwidth parameter, which as we have defined it makes $V_0 = B_0/\sigma\sqrt{2\pi}$ and places 64% of the total emission within distance $\sqrt{2}\sigma$ from the symmetry axis, where the volume emission rate is V_0/e .

Gaussian-shaped oblique column emission projections can not of course result from strictly gaussian radial volume emission rate distributions whose V_0 and σ change non-linearly with axial distance D from the accelerator. Nonetheless insofar as the fractional changes in V_0 and σ are not large over individual slant paths (column emission in these paths is in any case weighted to the region within 1σ of the glow's axis), the radial volume emission rates can be fit to gaussians with only somewhat larger chi-squareds.

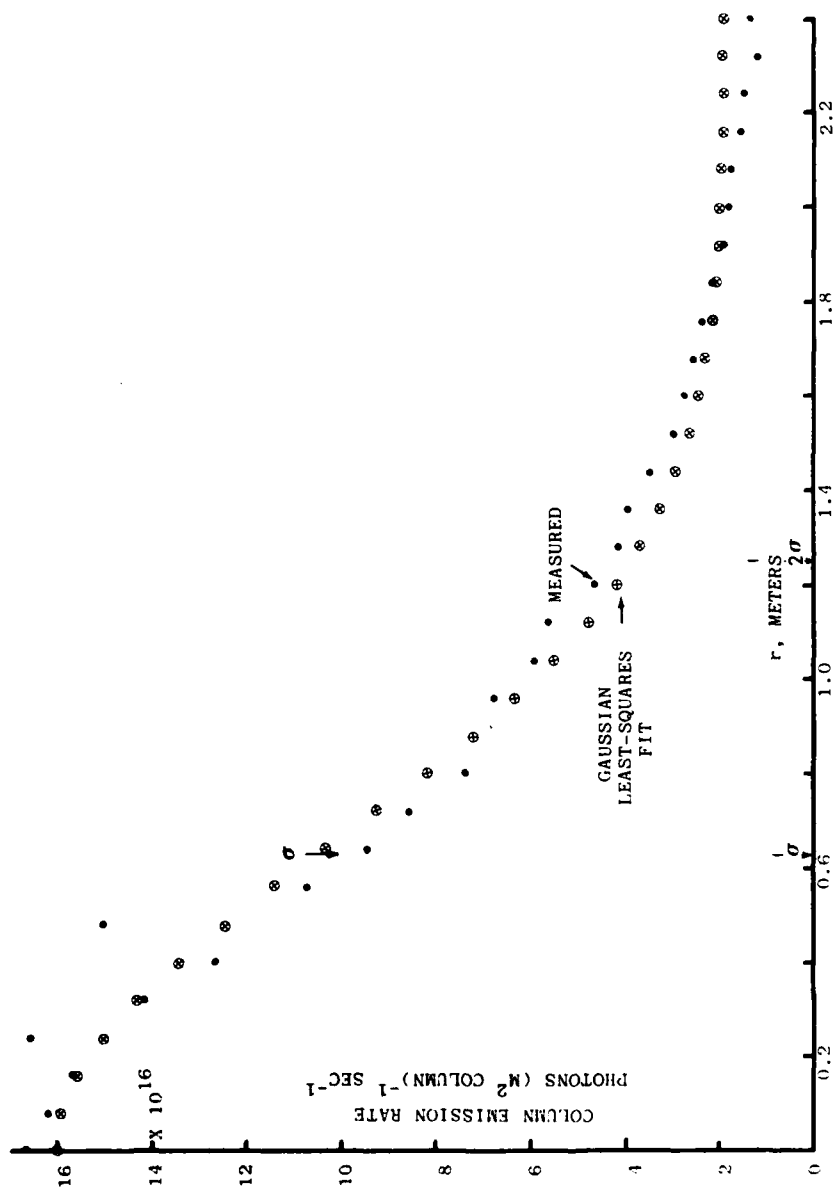


Figure 7. Gaussian least-squares fit to the measured column emission rates at distance $D=5$ m from the accelerator, 127.8 km on upleg (16169-3). Note the large fluctuations in some of the data points at large glow radii.

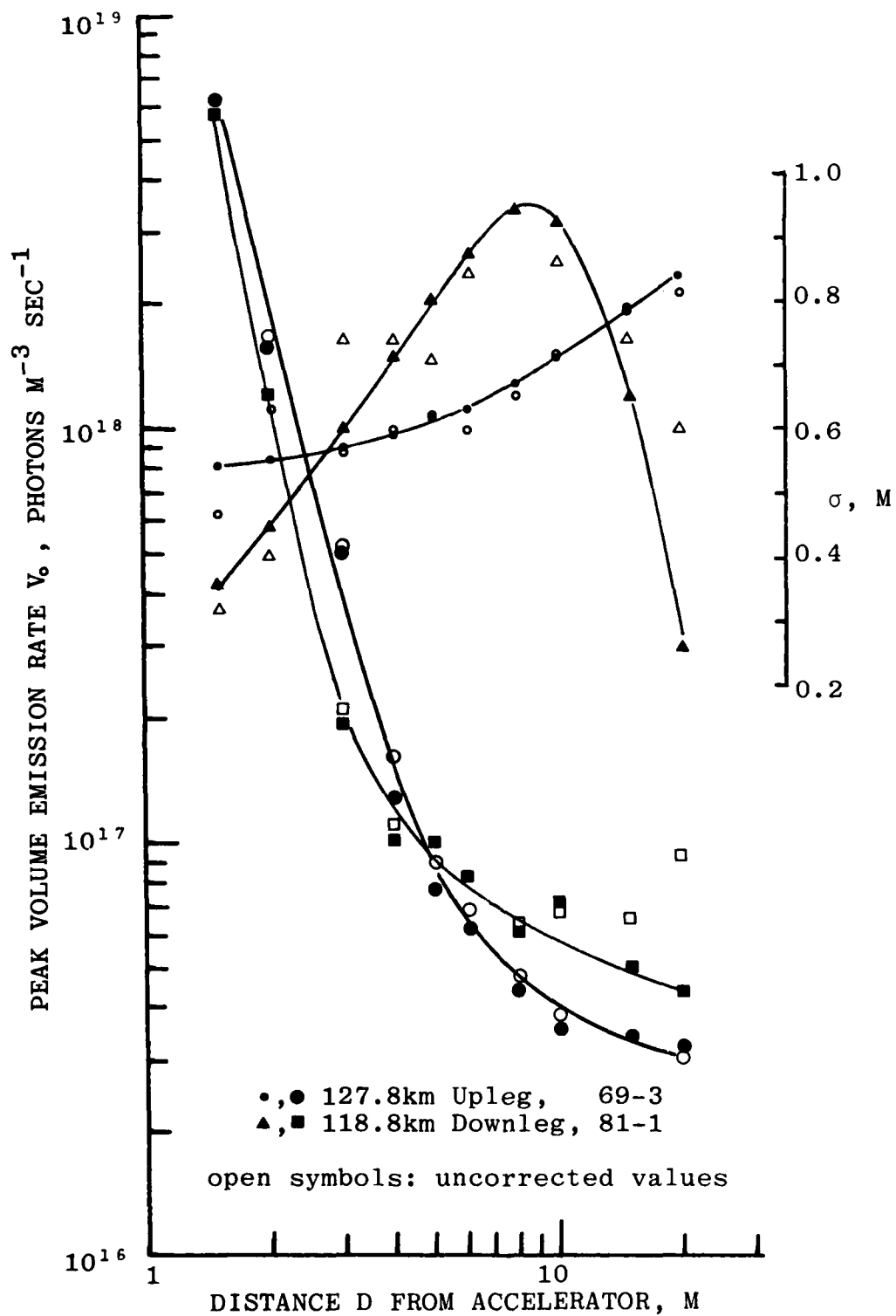


Figure 8. Examples of the effect on V_0 and σ of the first-order view angle correction for cases where the correction is small (127.8 km upleg) and large (118.8 km downleg).

We made a first-approximation correction for the oblique views using the following procedure. We summed three-dimensional volume emission rates from the set of zeroth-order V_0 , σ determined for $D = 1-1/2, 2, 3, 4, 5, 6, 8, 10, 15$, and 20 m to derive synthetic transverse radiance distributions viewing both perpendicular to the glow axis and from the camera's actual position. These were then fit to gaussians to determine new V_0 's and σ 's for the two sets of projections.

The improved V_0 's and σ 's are then each taken as

$$\frac{\text{measured zeroth-order } V_0 \text{ or } \sigma}{V_0 \text{ or } \sigma \text{ derived from synthetic slant-path data}} \times (V_0 \text{ or } \sigma \text{ derived from synthetic perpendicular-projection data}).$$

In practice, this first iteration resulted in only a small change in V_0 , σ up to $D = 8 \text{ m}$, and in some of the frames a large (factor ~2) decrease in σ and increase in V_0 at $D = 15$ and 20 m . Cases with small and large corrections are illustrated in Figure 8. A second iteration may be indicated for these latter data.

RESULTS

The first-approximation corrected V_0 's and σ 's for the four upleg-downleg pairs are plotted in Figures 9-12, and plots for individual downleg frames at the lower altitudes of 110 and 85 km are in Figures 13 and 14. Results for 125 km downleg (Fig 10) are qualitatively different from the others (σ is larger and V_0 substantially smaller where $D > 5 \text{ m}$), which suggests that this data record should be re-examined for unanticipated errors. The altitude dependence of V_0 and σ at three distances along the beam axis from the accelerator is shown in Figure 15.

At the higher altitudes V_0 has two almost straight-line segments on the log-log scale and is largely independent of

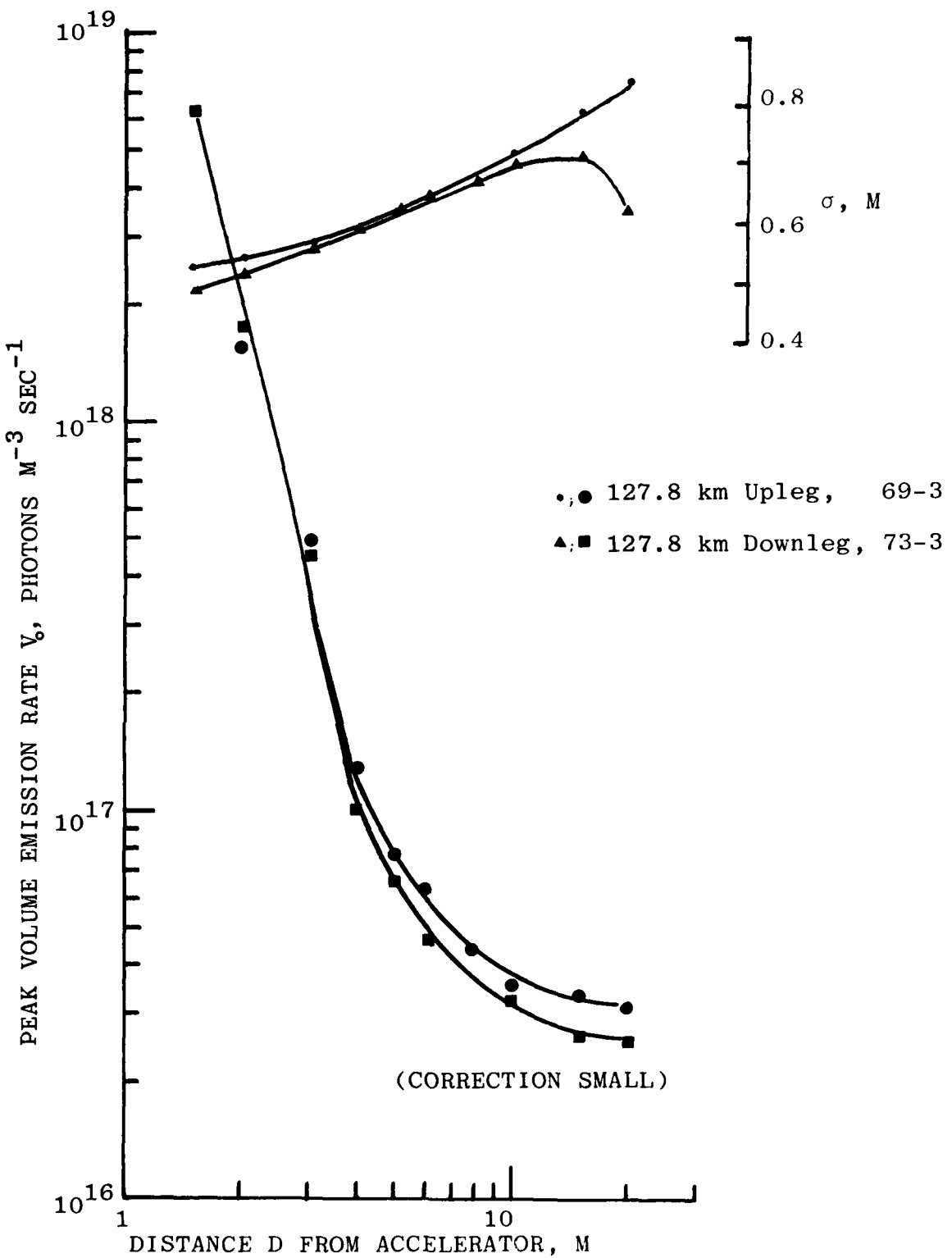


Figure 9. Photographic volume emission rate V_0 on the beam axis and gaussian width parameter σ , for altitude 127.8 km on upleg and downleg. The sight path correction is small, as shown in Fig 8.

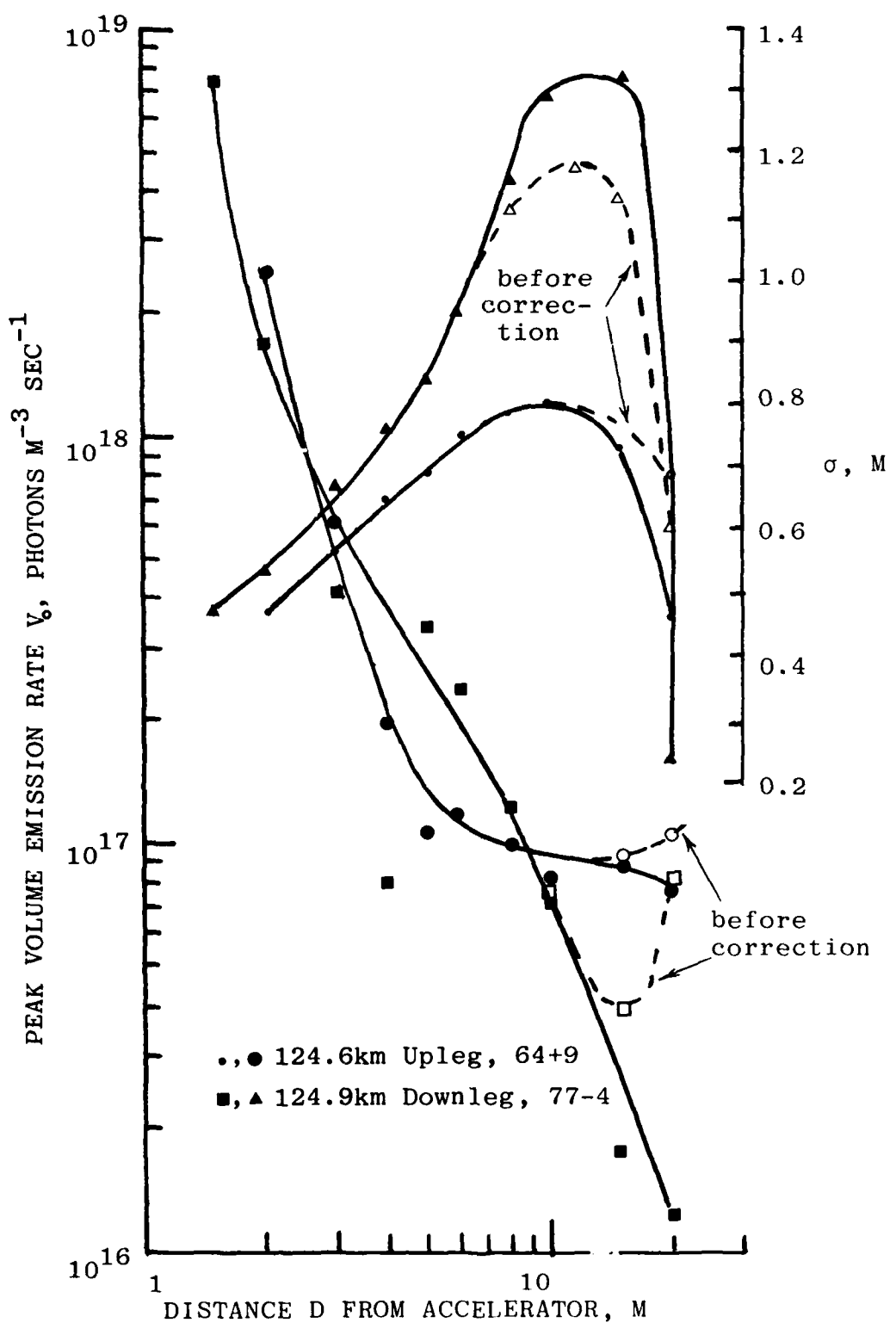


Figure 10. Photographic volume emission rate V_0 on the beam axis and gaussian width parameter σ , for altitude 124.6 km upleg and 124.9 km downleg.

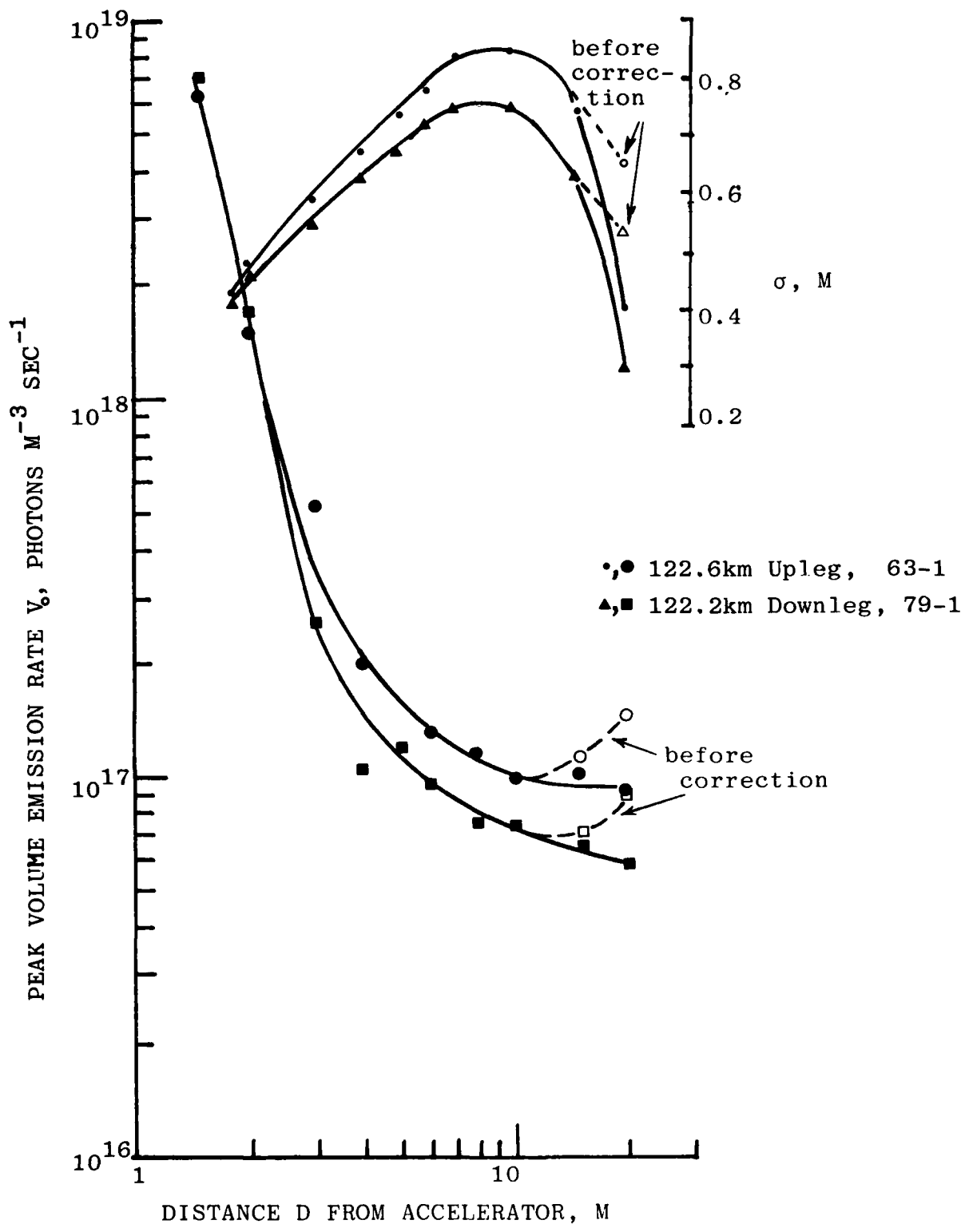


Figure 11. Photographic volume emission rate V_0 on the beam axis and gaussian width parameter σ , for altitude 122.6 km upleg and 122.2 km downleg.

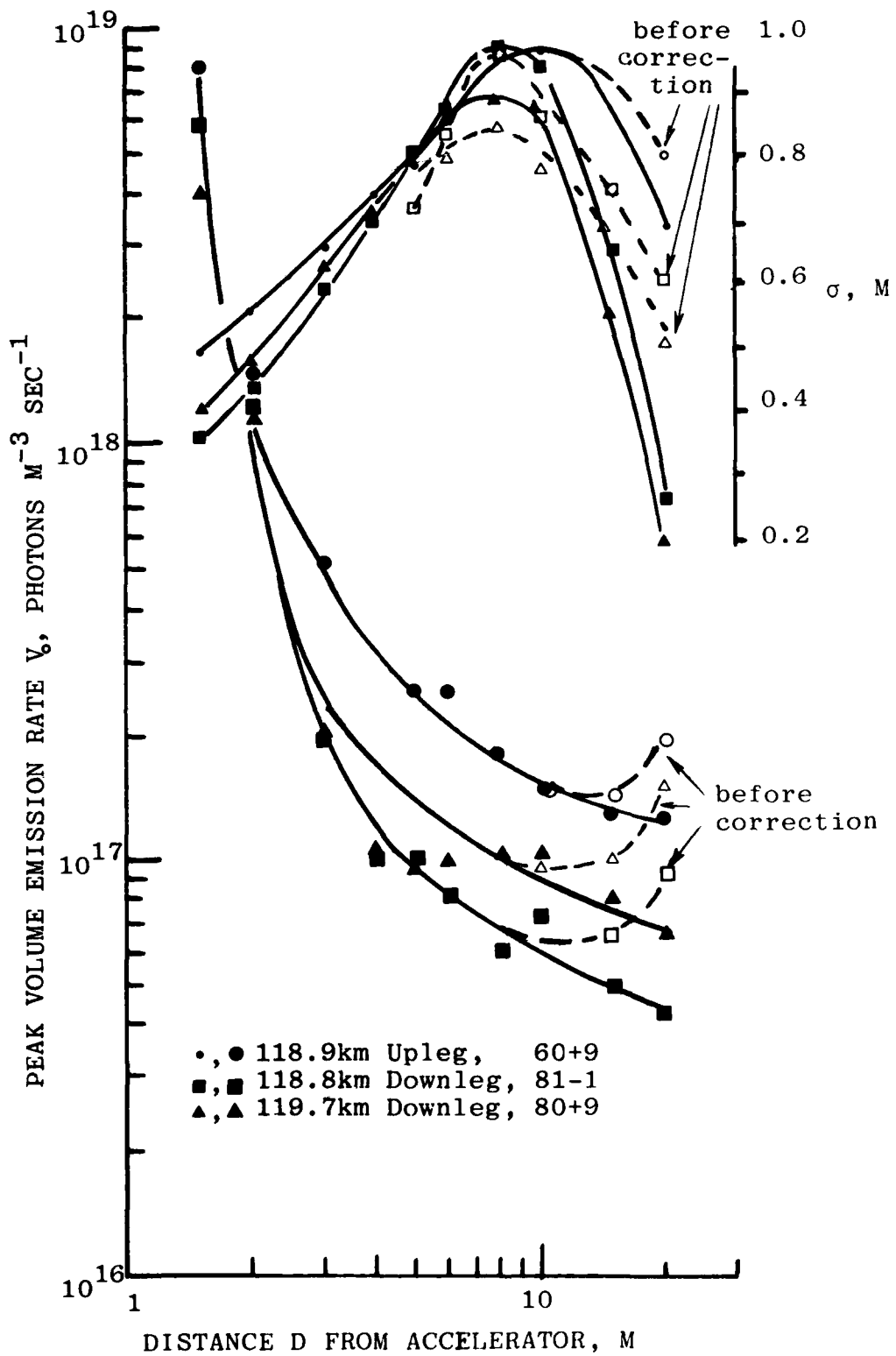


Figure 12. Photographic volume emission rate V_0 on the beam axis and gaussian width parameter σ , for altitudes 118.9 km upleg and 119.7 km and 118.8 km downleg.

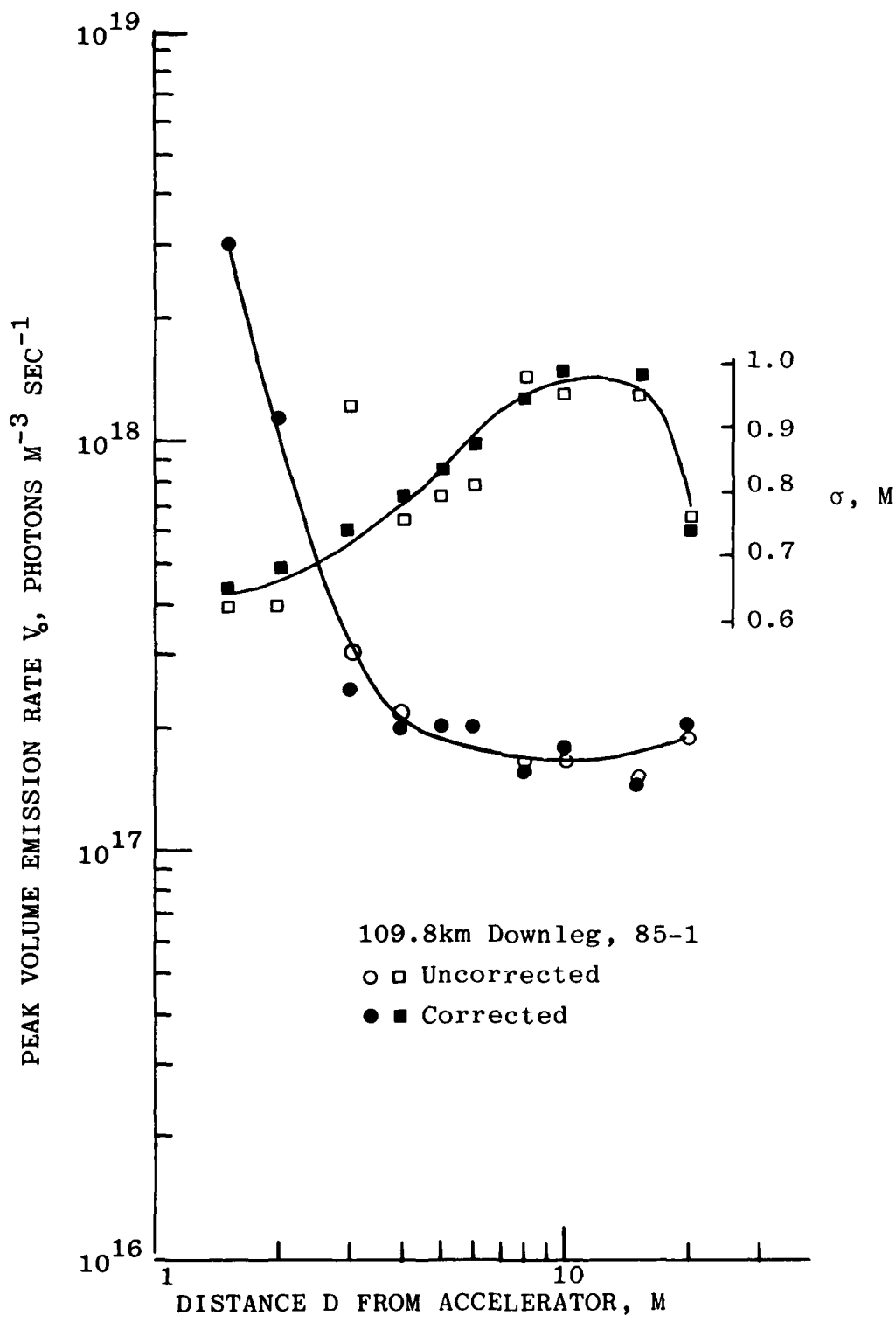


Figure 13. Photographic volume emission rate V_p on the beam axis and gaussian width parameter σ , for altitude 109.8 km on downleg.

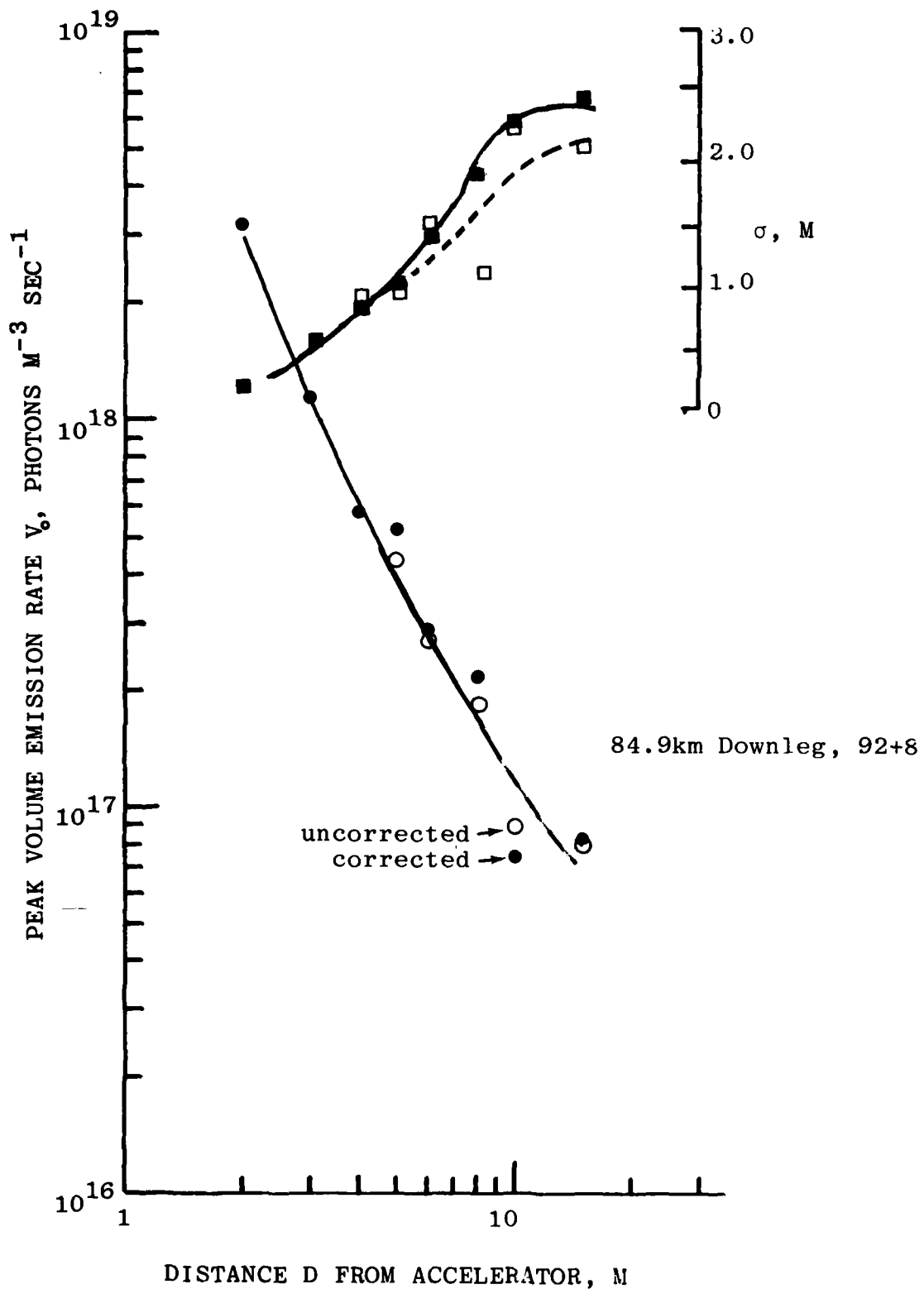


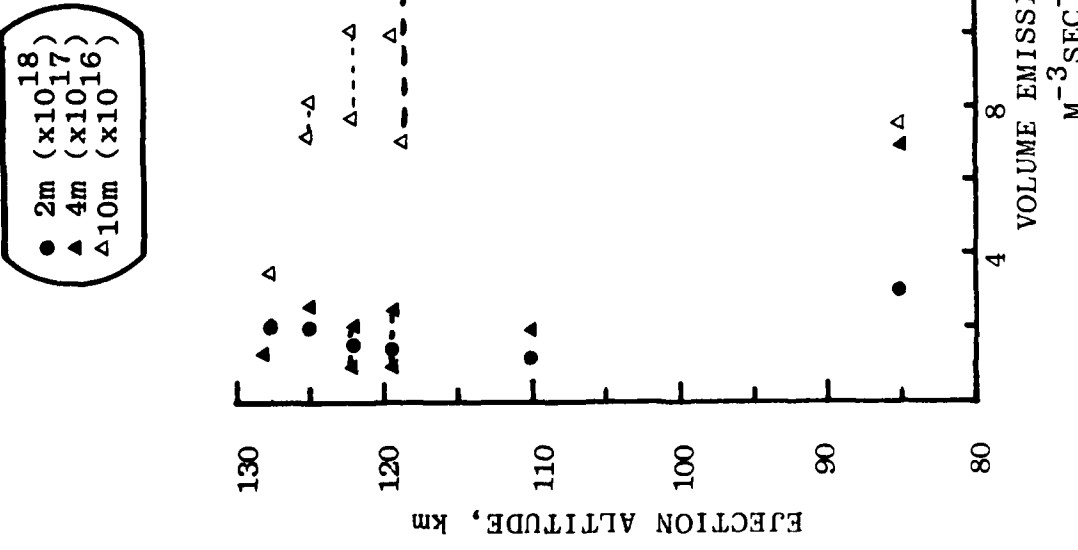
Figure 14. Photographic volume emission rate V_0 on the beam axis and gaussian width parameter σ , for altitude 84.9 km on downleg.

altitude, while σ at constant D decreases slowly with altitude. For $D < \sim 4$ m the logarithmic slope of V_0 is about -4, and beyond ~ 5 m it falls to about -0.3 (and is less well defined). The distance to the intercept of the two manually-drawn slopes shows an increase with altitude, being 3, 3, 4, 5, 5 at 110, 118, 112, 125, 128 km respectively. No sharp change in slope is seen at 85 km, where the practical range of 3 kV electrons is only 12 m. The large difference between the two dependences of V_0 on distance to the accelerator anode suggests that different physical processes are occurring in the two spatial regimes.

Even in the low-slope region V_0 is substantially greater than predicted by single-particle energy dissipation models (Ref 3) above at least 110 km. In any case the theory shows essentially constant radiance viewing perpendicular to the beam direction to well beyond 20 m.

A plausible preliminary interpretation of these findings is that a discharge is occurring in the in-close region, from which energetic electrons flow down the field lines to produce the excess excitation beyond about 3-5 m. We return to this interpretation after reviewing further features of the volume emission rate geometry.

The gaussian width parameter generally starts to decrease with distance along the beam at $D = 6-10$ m, the exception being the 127.8 km upleg frame (Fig 9). While the σ 's are reliable when the view angle to the beam axis is $> 45^\circ$, when D becomes as large as 10 m some of the oblique-view corrections are quite large and the treatment would benefit from a further iteration. Nonetheless the turn-down in $\sigma(D)$ is present even before the correction is applied and does appear to be real. It may be caused by refocusing of the initially diverging beam by the near-parallel magnetic field as noted, expected to occur at $D = 21$ m. This would mean that the relative



velocity spread of the electrons is not large, that is, that collective interaction results in only moderate pitch angle scattering and heating of the beam. On the other hand as the primary electrons themselves produce only a fraction of the total excitation, their crossing-over would not be expected to have so substantial an effect on the measured spread parameter. The total excitation per unit path ($\int V \times d$ (area) = $2\pi\sigma^2 V_0(D)$, not plotted) is decreasing with increasing D beyond 6 m, as might be expected.

σ as well as $V_0(D > \sim 5 \text{ m})$ can be seen to be higher on upleg than downleg, the exception being the suspect data frame at 125 km. This effect was also observed by the onboard photometer (Ref 21). The volume emission rate distribution at 85 km is qualitatively different from that at higher altitude, as a result of the short electron range; the frame at 97.7 km would be expected to show a transitional behavior. At 74 km lateral Coulomb scattering is expected to form the excitation into a near-spherical volume of diameter about 2 m, which with its origin from accelerators closer to the camera requires reprogramming of the projection geometry.

COMPARISON WITH PRELIMINARY MODEL RESULTS

Densities and temperatures of the free electrons produced by collective interaction of the ejected charged beam with the plasma have very recently been computed numerically (Ref 20). Space-averaged volume rates of excitation of the major electronic and vibrational states of N₂ were calculated from the number fluxes and energies of both the heated secondary electrons and the primaries. The model assumes that a beam-plasma interaction takes place, and adopts a fixed coupling coefficient (0.1) for heating of the plasma electrons (secondaries and ambient-ionosphere) by absorption of wave energy from the resulting rf electric fields. To date it averages

this energy input over a breakdown oscillator length extending 10 meters along the geomagnetic field from the accelerator and width twice the Larmor radius of 3 keV electrons at the edge of the 15° half-angle ejection cone (1.2 m), and neglects transport of energy out of this volume.

The accuracy of the preliminary calculations is known to be limited because of these simplifications, the assumption that the electrons have a Maxwellian energy distribution, and omission of the backscattered and hard forward-scattered secondary electron component (which produces about as much ionization and excitation as the primaries themselves (Ref 10)). The plasma electrons' velocities would be expected to depart from a Boltzmann distribution near the higher end of EXCEDE: Spectral's altitude range because the time between electron-heavy particle (energy-loss) collisions becomes comparable to the time between electron-electron (energy-redistribution, and thus kinetic temperature-establishing) collisions. (That is, the actual population reflects directly the electrons' discrete energy losses when they excite ambient atmospheric species.) Nonetheless the model, which calculates the macroscopic results rather than the physical origin of beam-plasma interactions, is a source of ideas for interpreting measured volume emission rate distributions such as in Fig's 9-14 and emission spectrums in terms of plasma-physics processes. The data in turn serve to provide input parameters -- such as the dimensions of the interaction region -- for refining the calculations of electron energy distributions and thus excitation rates of infrared features.

The pertinent output of the calculation is time dependent, space-averaged volume excitation rates in the first 10 msec after the electron beam is turned on. Although its energy deposition is of course spatially continuous, for purposes of comparing theory and experiment the beam may be

Table 2. Velocities of the EXCEDE: Spectral rocket relative to the geomagnetic field.

TIME (SEC)	TIME-TO* (SEC)	ROCKET ALTITUDE (KM)	VELOCITY (M/SEC)			TOTAL
			PARALLEL	PERPEND- ICULAR		
136.0	-51.5	115.7	399.1	447.2	599.4	
143.0	-44.5	118.9	334.3	433.4	547.3	
153.2	-34.3	122.6	240.3	412.9	477.7	
160.0	-27.5	124.6	177.7	399.2	437.0	
179.0	-8.5	127.8	3.6	361.1	361.1	
197.0	9.5	127.8	-161.1	325.7	363.3	
214.0	26.5	124.9	-316.9	292.9	431.5	
223.0	35.5	122.2	-399.6	275.5	485.4	
230.0	42.5	119.7	-463.8	262.6	533.0	
232.0	44.5	118.8	-482.6	258.1	547.3	
246.5	59.0	111.8	-616.8	229.4	658.1	
250.0	62.5	109.8	-649.0	223.0	686.3	
267.9	80.4	97.7	-816.9	180.2	836.6	
283.3	95.8	84.9	-962.8	128.8	971.4	
289.8	102.3	78.9	-1024.6	99.8	1029.5	
295.0	107.5	73.7	-1070.2	115.1	1076.4	

* APOGEE IS AT T0 = 187.5 SEC AFTER LAUNCH

visualized as entering previously-undisturbed air volumes in time intervals determined by the interaction volume's dimensions and the rocket's velocity. For orientation, we show in Table 2 its velocity components v_{\perp} and v_{\parallel} with respect to the geomagnetic field direction (refer also to the diagram in Fig 4). The time interval in which the beam crosses transverse to the interaction cylinder is $\sim 2.4/v_{\perp}$ sec, and it passes one cylinder length down or up the field in $\sim 10/v_{\parallel}$ sec. (As the tabulated velocities show, these times are in general comparable to the 10 msec for which the model "freezes" the beam on a parcel of air.) The rocket instruments' fields of view as well as the beam itself dwell longer on the collective-interaction volume on downleg than upleg: the fields are passing out of the interaction region on upleg and into it on downleg (see Fig 4), a point to which we shall return shortly.

The preliminary model results for EXCEDE's electron ejection conditions show short (~ 3 msec), intense discharge pulses near apogee, and heating of the secondary electrons to temperatures near 6 eV at 10 msec at the lower rocket altitudes. This temperature decreases by about 5 eV from its narrow peak to clamp just below one of the excitation potentials of N_2 that are carried in the code's tabulations of energy-loss cross-sections. At the higher altitudes the rates of ionization and 3914 Å-band emission are about a factor 50 larger than those due to individual particle impacts during this pulse, after which they decrease to the rates determined by single particle dynamics. (As noted, the back-flowing and hard scattered electron component is not considered in the model.) The tabulation on the next page illustrates results of runs to date.

The interaction model in effect predicts the weak dependence of photographic volume emission rate on ambient neutral-species density within the first few meters from the

<u>Injection altitude:</u>	<u>128 km</u>	<u>123 km</u>	<u>100 km</u>
Duration of discharge pulse	~3 msec	~2 msec	No avalanche develops
Discharge ionization/ beam ionization, max	~100	~30	-0-
Plasma electron density, temperature at 3 msec	$10 \times 10^8 / \text{cm}^3$, 21-1/2 eV	$5 \times 10^8 / \text{cm}^3$, 21 eV	$5 \times 10^8 / \text{cm}^3$, 6.7 eV
Average 3914 Å photon emission rate, 0-3 msec	$1-1/2 \times 10^{10} /$ $\text{cm}^3 \text{ sec}$	$0.6 \times 10^{10} /$ $\text{cm}^3 \text{ sec}$	$1-1/2 \times 10^{10} /$ $\text{cm}^3 \text{ sec}$

accelerator (see Fig 15). (However the preliminary absolute numbers are well below those we measured, which may be due to numerical errors in the code's plotting routines.) The existence of a discharge phase with duration comparable to the dwell of the beam and instrument fields on parcels of air in the flux tube provides a potential explanation for the differences in apparent volume emission rate between upleg and downleg (as noted this also shows in the onboard 3914 Å-band photometer data). Since on upleg the beam passes through undisturbed air volumes at a higher velocity, and the fields of view move more rapidly out of the interaction region, the onboard instruments -- including the camera -- see on the average the higher air-excitation rates due to the brief discharge pulse. Note that the increase with decreasing rocket altitude in the upleg/downleg radiance ratios at D = 4 and 10 m (Fig 15), and also in the photometer data, is in the same direction as the increase in ratios of the v_{\perp} 's listed in Table 2.

Three further points about the model's predictions merit notice. First, the "zero-dimension" calculations do not of course reproduce the steep longitudinal emission gradients observed in the first 10 meters. (Space-resolved calculations are underway, Ref 20.) We estimated the fraction of the beam's energy going into the close-in glow by extrapolating the volume emission rate distribution at 128 km to $D < 1-1/2$ m from the acceleratoreator. The result indicates that at least 1/10 of the energy -- the figure adopted in the model -- couples to the plasma.

Second, even when no discharge is ignited the secondary electrons heated by plasma instabilities to energies above the excitation thresholds of electronic and vibrational states of ambient and newly-created molecular species will alter the optical/infrared spectral intensities. Reference is made to our comments in Ref 1 on this issue, in particular with regard to the N₂ triplet sequence, the CO₂ 4.3 μm and 15 μm bands (also enhanced), and the unexpectedly high signals from water vapor in its 2.7 μm and 6.3 μm bands and perhaps at longer infrared wavelengths. We point out that the measured radiances in these and other infrared emission features would also be different at the same altitudes on upleg and downleg due to the effect on the time-averaged signal of the aforementioned temporal variations in electron temperature during the beam-plasma interaction. (This issue has not been directly addressed in the spectrum data analyses to date.)

LONGITUDINAL EXTENT OF THE EXCESS EXCITATION

Third, these heated plasma electrons flow out of the interaction region, in both directions along the geomagnetic field lines. (Their gyro radii are much smaller than their collision mean free paths down to at least 85 km altitude.) This second electron source enhances the Coulomb-backscatter

tail behind the accelerator, and in the direction in which the 3 kV beam is injected it both increases the radiance at wavelengths where photographic film and video cathodes are sensitive and -- more important for EXCEDE simulation purposes -- extends the distance from the rocket in which the excess excitation referred to in the preceding paragraph takes place. The enhancement in photographic signal (over that predicted by an independent particle energy dissipation-transport model) to a few hundred m at 128 km injection altitude is shown in Ref 3; note that the cross-field integrated intensities in the backward direction are almost as large as those in the ejection direction (Fig 3-9), which would be expected if high fluxes of ~21 eV plasma electrons are diffusing outward from the interaction volume.

The propagation of these heated electrons can of course be directly computed from the cross-sections of ambient atmospheric species for inelastic collisions and elastic scattering into the backward hemisphere. We made a first-order calculation assigning energy kT to each electron (that is, neglecting the energy spread of the thermal distribution) and assuming that they transport in a one-dimensional (field-confined) random walk due to $>90^\circ$ collisions. This simplified calculation shows the mean free paths for one energy-loss collision to be 120 m at 128 km altitude, 60 m at 123 km, 25 m at 100 km, and 5 m at 90 km. The bidirectional flux of these second-source electrons reduces to that of the unheated secondaries from the beam after perhaps three such interaction lengths. Thus their effects on the infrared spectral distribution become small beyond $D \approx 75-350$ m above 100 km beam ejection altitude, and at substantially shorter distances at lower altitudes.

This simplified calculation provides estimates of the minimum measurement-intercept distance for remote optical/IR sensors on the daughter platform in mother-daughter EXCEDE

investigations. The electron transport calculation can be refined and even specialized to excitation of specific infrared emission features (for example, those collisionally excited by very slow electrons) by applying propagation codes such as ARCTIC (Ref 7). This effort would be justified when the computations of the plasma electrons' energy spectrum, taking into account the dwell time of the beam and the longitudinal variation in energy coupling, are finalized.

A NOTE ON OUTGASSING

We discuss briefly the potential role of outgassing of N₂ molecules from the rocket in producing the measured photographic volume emission rate distributions. That the radiation to which the camera is responding is indeed virtually all N₂ fluorescence is shown by the glow's spectrum, and secondarily by the measurement of 3914 Å radiance at axis intercept D = 4-1/2 m. To result in the observed emission pattern the spatial distribution must explain (among other features) the aforementioned similar decrease of V_o in both upleg and down-leg ejection geometries, its essentially constant near-in altitude profile above 100 km, and the high signals from beyond D = 30 m reported in Ref's 3 and 4. Further, the total number of N₂ molecules calculated as outgassed over the trajectory must be consistent with the number that could reasonably be expected to be carried up by EXCEDE: Spectral's 0.6 m radius, 6 m long Talos Castor vehicle.

Desorption of much more easily condensed H₂O molecules from EXCEDE is evidenced by the strong water vapor (and some H₂) radiations when the beam was on (Ref 5), and perhaps also by collisional quenching of other emissions by H₂O. Its v₁ and v₃ bands at 2.73 and 2.66 μ m (effective radiative lifetime 10 msec) were reported detected by the interferometric spectrometer with decreasing intensity between at least 105

and 81 km downleg rocket altitude (p 133), and the presence of its ν_2 band at $6.3\mu\text{m}$ and rotational lines above $17\mu\text{m}$ (pp 183ff) is also inferred. (Preliminary attribution to H_2O of $\sim 2.75 - 3.0\mu\text{m}$ emission seen at 74 km by the circular variable filter spectrometer (pp 29-30) is probably in error, as the unstructured feature lies at too-long wavelengths.) The interferometer's field of view intercepts the beam axis at 4 m from the accelerator, which is large compared to the molecular collision mean free paths in this altitude range (see below). Thus the electron beam is presumably indirectly (by excitation transfer) or directly (by impact) exciting H_2O left in the rocket's wake. Altitude profiles of intensities in these water vapor bands, which would be expected to differ on upleg and downleg, have not yet been derived from the spectrums.

The spatial distribution of outgassed molecules calculated for spherical-shaped orbiting satellites (Ref's 22, 23; other treatments are referenced in Ref 24) can be adapted for estimating the dependence of outgassed N_2 concentrations on ambient air density and distance D' from the cylindrical sounding rocket. The model predicts that the density of desorbed molecules decreases from the vehicle surface both as D'^{-1} or 2 and exponentially with a scale length about 0.4 times the collision mean free path. This length is 550 cm at 128 km altitude, 150 cm at 120 km, 25 cm at 110 km, and 6 cm at 100 km (and 1 cm at 90 km and 0.1 cm at 80 km, where agreement of volume emission rates with independent-electron energy dissipation calculations has not been tested and excitation of water vapor is still observed). These numbers, as expected, are comparable to the initial-expansion radii of luminous chemical releases (Ref 25). As the rocket's velocity (Table 2) is greater than the molecules' thermal velocities (after collision) at all but the highest ejection altitudes, the close-in

spatial distribution is different in its wake and motion directions. This appears to contradict the observation that the volume emission rates differ between upleg and downleg in magnitude rather than "shape" (they are actually lower looking into the wake). Further, the excess high-altitude emission at $D \approx 5-20$ m when the electron beam is directed either ahead of or behind the rocket, and also at $D \approx 40-400$ m, falls off much more slowly than predicted from Ref 22's outgassing-transport model.

A rough estimate of the outgassing rate required can be derived by comparing an N_2 density inferred from the model with that which would fit the prediction of electron energy deposition theory. At 123 km and $D (\approx D')$ = 2 m the measured V_0 is 100x that predicted, which would call for an outgassed N_2 density 100x ambient, or $3 \times 10^{13}/\text{cm}^3$. Taking either Eq 12 or 18 of Ref 22 (for spherical spacecraft) as applicable to EXCEDE, for which we adopt an effective radius of 1 m, we find that the required outgassing rate is about 1 mole/sec. This means that to fit this reasonably typical emission data point the payload and recovery system must be releasing as much as 20 liters of N_2 at standard temperature and pressure each second.

These arguments, while by no means the last word on the issue, indicate that outgassing alone does not fully explain the spatial and altitude profiles of N_2 fluorescence excited at EXCEDE: Spectral. Note, however, that outgassing is thought to play a part in ignition of discharges near electron injection rockets (by providing a more dense plasma, Ref 26); thus quantitative calculations of the desorbed molecules' spatial distribution would apply in refining the beam-plasma interaction model.

SUMMARY, CONCLUSIONS, RECOMMENDATIONS

The volume emission rate distributions of N_2^+ and N_2 fluorescence unfolded from onboard radiometric photographs of the glows produced when EXCEDE: Spectral's accelerator #4 injected 7-8 amperes over the altitude range 116 km - 128 km apogee - 85 km show the following principal properties.

- 1) Very rapid falloff along the beam axis within the first ~5 m from the rocket, with
- 2) little dependence on ambient density above 110 km (and perhaps lower altitudes), and
- 3) more excitation than predicted by individual-electron energy dissipation theory both in this region and in a region of slower decrease that extends to at least 20 m;
- 4) a fit to gaussians transverse to the symmetry axis, with width parameter that increases up to ~6 m from the rocket and then decreases in all but one or two of the 78 millisec-exposure frames reduced; and
- 5) higher maximum values and width parameters on upleg (that is, earlier in the flight) than on downleg, where the electron beam and fields of the camera and other instruments are directed into or very close to the rocket's wake.

The altitude dependence (Item 2) and existence of two emission regimes (Items 1,3) are consistent with a discharge close-in to the rocket, the excitation in which is being predicted by a current theoretical study program (Ref 20).

An approximate calculation of the ranges of the secondary electrons that flow outward from this region in both directions along the geomagnetic field, using the mean energies from the preliminary model calculations, is in qualitative agreement with the few hundred m derived from an analysis (Ref 3) of photographs of the visible glow taken from a ground station. The predicted distance along the injection flux tube beyond which IR/ optical measurements from daughter platforms would include only negligible amounts of radiation excited by plasma electrons -- that is, where the injection of keV electrons more precisely simulates excitation of the atmosphere by particles from nuclear explosions -- decreases with decreasing altitude through the E region. However the altitude resolution in the set of photographic frames so far evaluated is insufficient to verify estimates of the altitude at which this standoff distance approaches the long dimension of current sounding rocket payloads.

These transport calculations can be readily improved and specialized to individual impact- or indirectly-excited infrared features (for example those from CO₂ molecules) when the energy spectrums of the heated secondary electrons resulting from collective interaction of the primary beam electrons is finalized. Further, the measured longitudinal and lateral distributions of excitation provide input parameters for model calculations. For example the preliminary runs assume the plasma heating regions to be uniform within in a 10 m long, 1.2 m (Larmor) radius cylinder, while the data indicate axial limits of 3 m at 110 km injection altitude increasing to 5 m at 128 km, and gaussian widths decreasing with increasing altitude. The observed extremely strong dependence of emission on distance from the accelerator's anode indicates a need for space-resolved calculations of the excitation of N₂ and N₂⁺ by plasma electrons.

The volume emission rate patterns do not appear ascribable to outgassing from the payload, as both physically-unreasonable spatial distributions and total number of desorbed N₂ molecules would be required. Nonetheless the question of outgassing merits further consideration, as it affects both the initial molecule densities in the beam's path and (through its strong H₂O component) the ionization-excitation potentials to be input to beam-plasma interaction calculations. We have provisionally interpreted the higher radiances on upleg (Item 5) as an effect of the ~3 msec (calculated) duration of the avalanche phase of the collective interaction within the image field. This idea, however, has not been quantified. One of its ramifications is that the relative spectral distributions at ultraviolet, visible, and infrared wavelengths will also differ along EXCEDE's trajectory, a point that has not been investigated from the data in existing emission spectrums. Indeed, the uncertainties inherent in the model calculations indicate a pressing need for evaluation of the upleg and downleg altitude profiles of radiance in features whose excitation mechanisms are quantitatively understood (for example the N₂ Second Positive and other triplet systems), for refining the energy distributions of the secondary electron component that is also exciting less well understood infrared features.

Interpretation of the decrease in gaussian width in the outer, low-slope emission region as due to refocusing of the initially-diverging 3 kV beams by the geomagnetic field does not appear consistent with the conclusion that these plasma electrons contribute much more of the fluorescence excitation than the beam electrons. Beam-plasma interaction theory should provide further information about the velocity spread of the primary electrons (which would be expected to be related to the energy transferred to the plasma), and about the physical

interpretation of the gaussian width parameter's longitudinal variation. In this regard, the end-points of detectable glow radiance in ground photographs (which are only partially analyzed) so far do not indicate severe energy degradation of EXCEDE: Spectral's beams.

The major conclusion of this evaluation of EXCEDE: Spectral closeup images is that excess fluxes of secondary electrons accompany the primary field-confined beam to at least 20 m at injection altitudes above ~100 km. As the expected energy distributions of these electrons (near-Maxwellian, with peaks comparable to the excitation potential of atmospheric species, Ref 20) differ from that of the secondaries produced in impact ionization by fast charged particles (power-laws, Ref 10), the infrared emission spectra they excite in the atmosphere will differ out to 10's - 100's m from the rocket at altitudes where conventional thermionic cathodes and cryocooled spectroradiometers operate without severe interference from the atmosphere. Comparison of the measured fluorescent-emission patterns with early model predictions is still preliminary, and several of the geometric features have not been interpreted.

SECTION 2

CORRELATION BETWEEN 2.8-3.1 μ m CHEMILUMINESCENCE AND PARTICLE ENERGY INPUT TO THE ATMOSPHERE

BACKGROUND

The high spatial- and temporal-resolution aircraft measurements of short wavelength infrared emission from aurora (Ref's 1,27) represent the primary source of direct information about this radiation's correlation with deposition of ionizing energy in the real atmosphere, and thus about structure of the SWIR sky background resulting from nuclear explosions. In this section we quantify the relationship between near-zenith radiances in the 2.832-3.125 (FWHM) wavelength band (the infrared output, from vibrational chemiluminescence of NO) and a fluorescence band of N₂⁺ (which measures the energy input rate into the air column) using the procedures we developed as part of the Test Plan for the aircraft data missions (Ref 28).

The measurements were made with a cryocooled radiometer accurately coaligned (as described in Ref 29) with a conventional photoelectric filter photometer having the same 6 millirad-square field of view. (The atmosphere above the NKC-135A jet aircraft's operating altitude is essentially transparent and presents only small thermal background in the selected sensitivity band.) This field gives a 7/10 km instantaneous footprint at auroral-emission altitudes, comparable to that under consideration for future spaceborne infrared surveillance systems. Signal integration time for S/N ~ 10 was less than 1 sec, during which the aircraft moves 2/10 km. The instruments were fixed-mounted in AFGL/DNA's Optical Flying Laboratory (serial 55-3120) to point to the magnetic zenith when it was flying south along a geomagnetic meridian

at auroral latitudes in the Western Hemisphere, so as to view particle beams restricted to a narrow flux tube and thus with a nominally unique and calculatable altitude profile of energy deposition. Data taken when the aircraft was returning northward in series of passes underneath the auroral oval, and from some west-east flight trajectories, were also analyzed. Support instrumentation onboard included a photographic all-sky camera (images spanning the useful radiometer data segments are shown in Ref 1), all-sky and narrow-field video camera with better temporal resolution (so far not applied in the data evaluation), hydroxyl airglow radiometer (for measuring the comparably intense but very slowly varying fundamental Meinel-bands background in the $2.8 - 3.1 \mu\text{m}$ signal), and multi-channel filter photometer (which determines the peak energy deposition altitude of the auroral electrons (Ref 30), and in addition served in calibrating the primary air-fluorescence photometer).

Further particulars of the aircraft measurements, background information on the aerochemistry of NO^+ , and program results to date are given in Ref's 1 and 27 and the references therein. To place the current data evaluation in context we briefly review here the previous findings from the flights of the narrow-field instruments in 1979-1980 and similar earlier missions with a 160 mrad-field, 30 sec-response pair whose axis pointed to the aircraft's zenith (also supported by the instrumentation described above). The yield of SWIR photons in the radiometer's passband from the atmosphere between 150 and 100 km is linear with energy-input rate in the range reached in aurora, $\sim 10^5 - 10^6$ ion pairs/cm³-sec; however this energy conversion efficiency varies over at least a factor two within individual flight missions and a factor 3 among missions, for reasons that have not been explained. The mean yield, and even the minimum yield, is

higher than predicted from laboratory and theoretical investigations of NO vibrational band excitation/de-excitation (on which more shortly), but consistent with the results of sidelooking rocket radiometry of auroral forms (Ref 30). No statistically-significant correlation has been identified between this energy conversion efficiency or the delay in SWIR emission following particle input and geophysical or instrument factors such as solar illumination of the auroral ionosphere, rate of energy input, K_p, measured intensity of the hydroxyl airglow (which might indicate calibration instability), aircraft flight direction, or position of the flight in the series. On the other hand the yield of NO photons averaged over ~1-min data segments appears to be increasing with altitude of the maximum in the auroral electron energy deposition profile, in the 110 - 130 km altitude range containing most of the peaks' occurrences (Figure 16).

The aircraft radiometry data have resolution far superior to that of the SWIR output-energy input measurements from rockets (or contemplated research satellites, which have less favorable viewing projections). Quantification of the temporal-spatial correlations would permit the visible-photographic data on past high altitude nuclear detonations to be used for characterizing sky clutter in the important 2.8-3.1 μm wavelength band.

DATA

A total of 15 segments from 10 flights has been selected for analysis on the basis of their large infrared signal enhancements coincident with visible aurora. The ~70 min of data include a mix of instrument pointing directions (5 segments are from the intended magnetic zenith) and solar depression angles. Another 6 segments (~15 min), in which the column emission rates in the N₂⁺ (0,0) First Negative fluorescence

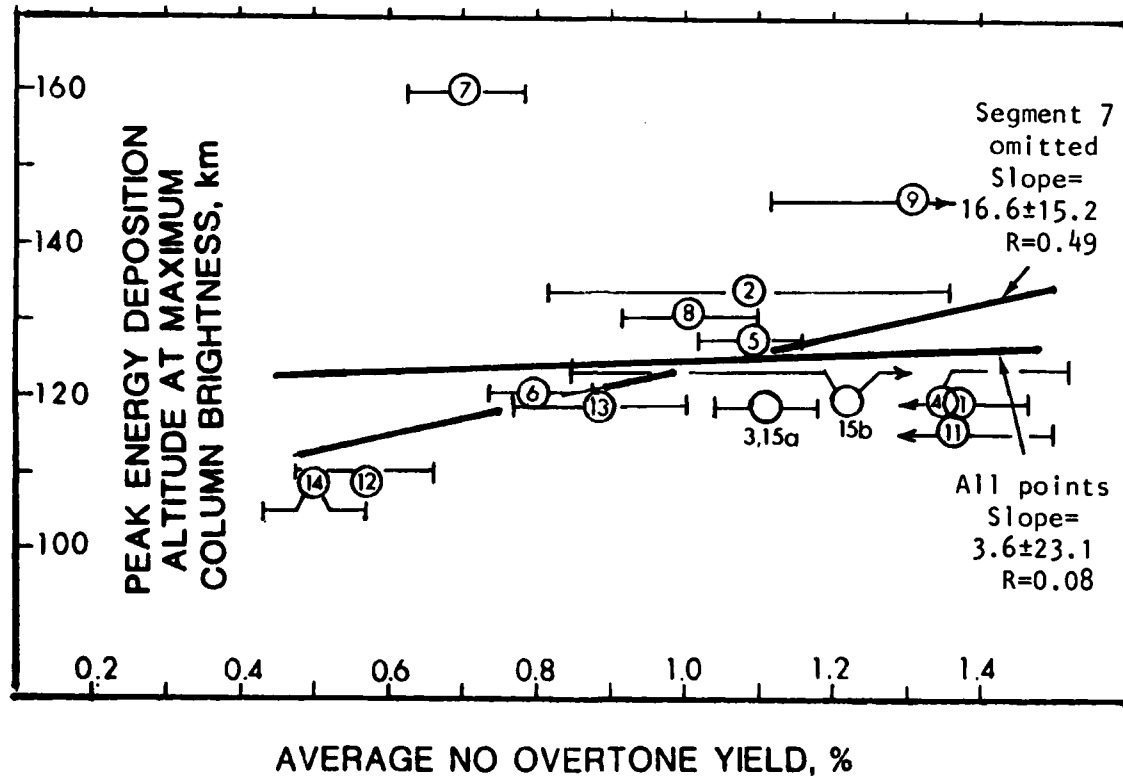


Figure 16. Altitude dependence of NO overtone emission yield in the 15 aircraft data segments. The error bars on yields are statistical, and the altitude uncertainty (+10, -5 km) is omitted.

band ranged from 20 up to 50 kilorayleighs, may also merit evaluation. (Column energy input is proportional to intensities in this sequence within 10% over the measured range of peak deposition altitudes (Ref 30; see also Section 1).) The signal/noise and signal/background ratios in these data segments are indicated by Fig 22's reproduction of the typically 1-sec pre-integrated and sampled traces; we applied no further filtering. Flight conditions for these data are listed in Table 3 (from Ref 1).

Chemiluminous yields in the nitric oxide overtone system are plotted against altitude of the auroral particles' maximum energy deposition in Fig 16. Effective height of the columns is about 30 km, 10 km of which is below the profile peak. The error bars indicate 90% confidence limits on the slope of the best-fit regression line between simultaneously-measured column energy input and infrared output (as in Fig 4 of Ref 27; an averaging method was used as a check in cases that output lagged input by more than ~3 sec), and do not include possible experiment sources of error. The estimated vertical error bar (two standard deviations, not shown) is +10, -5 km.

These yields assume that a fixed fraction of a model spectral distribution in the nitric oxide overtone system -- 42%, principally from bands originating from the 6th to 12th vibrational states -- remains in the wavelength region to which the radiometer responds. The actual spectrum of emission from the atmosphere has not been measured with sufficient resolution to identify individual $\Delta v = 2$ transitions. It is expected to be weighted to these measured (longer-wavelength) bands at lower energy-deposition altitudes because the vibrational cascade is partially quenched by collisions (Ref 31); however, as Fig 16 shows, the yields in the instrument's sensitivity band indicate a decrease with decreasing altitude. (We return to this issue in the following subsection.) The obser-

Table 3. Experimental and auroral parameters of 2.8 - 3.1 μ m-band enhancements.

SCEEN Passage	FLIGHT DATE Meridian	TIME (UT)	ARC POSITION Lat. Long. < A/C turnup>	HEADING True Nm	DEPTH (deg/sec.)	TRAJECTORY ALTITUDE (deg/sec.)	SOLAR ANGLE (int. 13 deg connected)	ILLUMINATED HEIGHT (13 deg (h=0.98 d))	RATIO ++ (6.3m/278) (5.57/3914) photons/photon	PEAK MAGNETIC INDEX ++ K Kp	
①	909/22 Apr 79	0237	51.36 71.38	321 360	321	13.61	-10.98 0	-18.75	113.3	11.1/14.9	84.8/43.2
	1153	0246	57.99 66.95	087 29	012	-21.74 0	-21.55	45.1	109.9	10.5/10.5	133.7
②	909/22 Apr 79	0237	51.36 71.38	321 360	321	-10.98 0	-18.75	113.3	11.1/14.9	84.8/43.2	
	1153	0249	61.63 71.76	321 360	331	-10.82 0	-10.59	119.5	11.1/14.9	84.8/43.2	
③	0213	58.94 68.67	325 360	328	13.60	-12.14 0	-11.91	129.4	7.0/10.3	2/3.1	
	0216	59.22 68.93	325 360	328	-12.02 0	-11.79	136.2	119.5	3 3		
④	0220	59.54 69.29	325 360	328	13.60	-11.89 0	-11.73	134.8	9.6/24.3	96.0/70.6	
	0224	60.47 69.67	325 360	328	-11.66 0	-11.43	128.0	119.8	3 3		
⑤	0226	61.76 69.61	144 180	135	13.61	-12.06 0	-12.31	148.5	5.1/6.4	29.1/18.6	
	0229	61.75 69.28	144 180	135	-12.58 0	-12.86	160.6	127.7	3 3		
⑥	0237	61.76 67.51	320 360	344	13.61	-23.42 0	-23.28	531.1	4.9/11.9	76.7/34.5	
	1153	0244	47.36 67.66	346 360	344	-22.89 0	-22.75	507.2	120.0	7 8	
⑦	924/18 Sep	0016	58.36 73.57	281 316	279	2.19	-9.40 0	-9.18	87.6	11.0/10.9	73.8/31.6
	1154	0019	58.29 74.12	269 306	269	-9.55 0	-9.34	85.5	159.5	4 6	
⑧	926/25 Sep	0016	58.94 77.67	164 292	265)*	-0.54	-10.05 0	-9.83	94.7	6.4/9.2	65.1/23.8
	1152	0022	57.32 78.82	171 168	198	-10.84 0	-10.54	117.3	127.2	3 4	
⑨	927/27 Sep	0020	54.77 68.83	327 356	327 3*	-1.35	-30.70 0	-30.47	919.9	2.5/1.3	13.7/3.6
	1151	0023	55.05 69.13	330 360	330 3turn	-30.62 0	-30.40	905.7	118.1?	3 4	
⑩	928/29 Sep	0119	57.18 76.59	230 269	228	-2.11	-20.21 0	-20.13	397.1	4.5/11.8?	(50.4/34.1)?
	1151	0123	56.76 77.27	230 260	233	-20.53 0	-20.45	409.8	116.0	3 2	
⑪	930/10 Sep	0054	60.99 122.02*	284 252	286	16.36	-9.17 0	-8.99	70.2	2.6/9.0	47.9/26.1
	1236	0744	63.34 124.75	284 252	286	-8.75 0	-8.62	72.8	108.8	6 5	
⑫	026/18 Aug	1125	65.86 147.49*	029 360	030	12.97	(0= Decreasing, Decreasing,	-9.05 1	97.0	4.1/26.6?	<196/106>
	1234	1126	65.16 147.36	029 360	030	I= Increasing)	-9.31 1	84.9	118.8	2 5	
⑬	1159	64.36 148.43*	209 177	207	12.96	-9.61 1	90.5	108.8	6 5		
	1203	63.93 148.95	209 177	207	I= Increasing)	-12.89 1	162.8	2.6/71.2	111.8/61.5		
⑭	027/19 Aug	1024	64.30 148.42*	026 358	029	12.65	-12.13 1	141.2	108.8	6 5	
	1204	1030	64.93 147.65	026 358	029	-11.45 1	128.5	4.7/10.0	<50/200>		
⑮	1055	65.85 147.46*	212 179	209	12.65	-12.34 1	149.1	119.5	6 5		
	1102	63.88 149.92	212 179	209							

* After flight 102, refer to latitude/longitude of intercept at 120 nm of the 12° tilted instruments

** 12° tilted, 10° longitude to 12° longitude, 1° zenith to flight: 909, 908, & 907

Brackets values are from our field photometer
+ + + K's refer to fulllege, All senior

+ + + K's refer to fulllege, All senior

* After 101 is the same as S 1955 - 01/75

vation that the energy conversion efficiencies that were measured with narrow-field instruments are generally higher (by almost a factor two) than those previously reported from the wider-field instruments, like the spread within each data set, is so far not explained.

The output of SWIR photons is found to lag energy input in all but one of the segments, in which no delay is detectable; in no case is the SWIR signal seen to lead. We estimated these lags (in Ref's 1 and 27) from the offsets between discrete radiance peaks and from differences in time for the two signals to return to baseline when excitation cuts off, finding that they vary from 0 to 6 sec with the distribution to be shown later in Fig 19 (and as noted, without any significant correlation with geophysical or instrument factors). Delays interpreted as the inverse of NO⁺ quenching rates were also computed (in Ref 27, by another group) using a method that involved dividing complex Fourier amplitude transforms of the input and output data streams to derive a transfer function of the atmosphere. This array was filtered after retransforming into the time domain applying an unspecified smoothing, and then was again transformed back into frequency space and fit to a single-or double-pole filter representation. This procedure results in quenching coefficients all but two of which lie within $1.1 \pm 0.1/\text{sec}$. (The result for one segment, for which we had estimated 0 to 1 sec delay, was $2.0/\text{sec}$.) This clustering may result from the use of a smoothing window of effective width 0.9 sec. Before determining delay times by applying Ref 28's cross-correlation and curve-fitting methods, we discuss briefly the existing information about excitation and quenching of NO⁺.

EXPECTED SPATIAL-TEMPORAL CORRELATION

The current model for production of vibrationally-excited NO molecules following ionization and dissociation of

N_2 in the upper atmosphere is illustrated schematically in Figure 17. Oxygen atoms can be seen to play an important part in the spectral yield and grow-in/decay time of the radiation, which is still unsatisfactorily quantified. Specifically,

- $NO(v)$ is deactivated by O , with partial rate coefficients for $NO(v')$ not yet reliably determined;
- N^2D , the principal precursor of NO^+ , is deactivated by O with a rate coefficient whose measured values (Ref's 32,33) differ by a factor 5 at 120 km; and
- N^2D is produced when N_2^+ reacts with O , but not when N_2^+ charge exchanges with O_2 .

In addition the probabilities that N atoms in the 2D state result from the key dissociation reactions are subject to error. A recent calculation (Ref 31) indicates that the uncertainties in the rates of the first two processes above and in the atmosphere's [O] profile result in a factor-2 uncertainty in the predicted steady-state volume emission rates of NO overtone at altitudes where auroral particles (and fission debris of nuclear explosions) deposit energy. However the highest derived column emission rates are still almost a factor two below the mean of all the aircraft (and aforementioned rocket) measurements. Runs of DNA's ARCTIC aerochemistry code (Ref 34) also resulted in similarly low overtone yields under steady-state particle irradiation.

Characteristic times in which the zenith auroral radiance approaches asymptotically these equilibrium values have also been calculated by ARCTIC (Ref 34), using model energy deposition profiles. They are 1-1/2 and 1 sec when the maximum of the profile is at 100 km and the input is stepwise increased and decreased respectively, and 7 sec when this

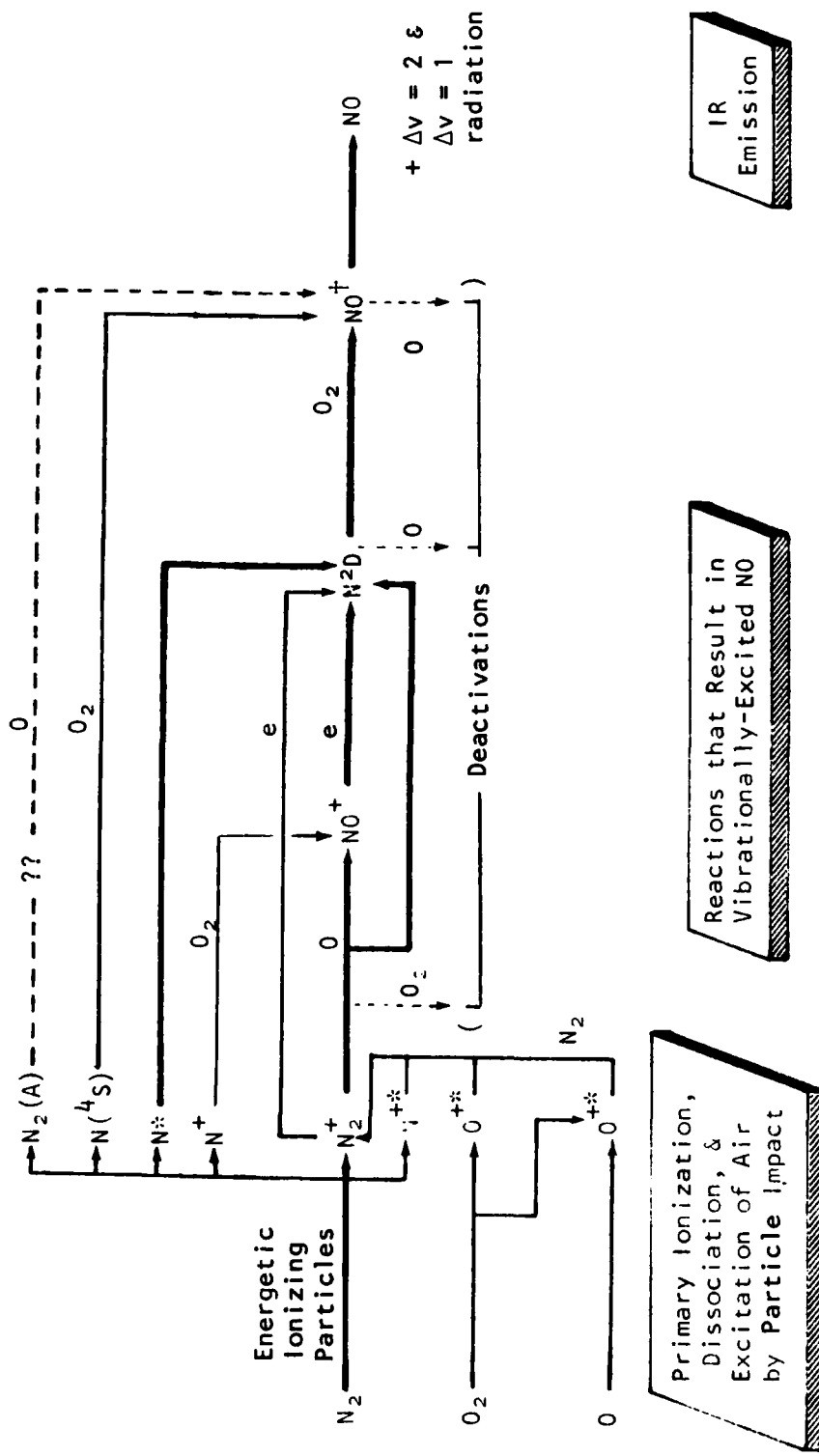


Figure 17. Schematic diagram of DoD's currently-applied model of excitation of nitric oxide vibrational radiations by energetic particles. Some minor reactions have been omitted. The principal reaction paths are shown by heavy lines.

maximum is at 120 km and the input is increased. AFGL/DNA's "BRIM" model of infrared limb brightness structure (Ref 35) makes the simplifying assumption that the final process of the principal reaction paths, $N^2D + O_2 \rightarrow NO(v) + O$ (whose rate coefficient is $5.2 \times 10^{-12} \text{ cm}^3/\text{sec}$) is the rate-limiting step in NO chemiluminescence. This directly implies that buildup of NO^+ ions, whose characteristic time for reacting with electrons is several sec, is not a major factor in production of N^2D atoms compared to direct impact dissociation of N_2 molecules. With this assumption the time dependence is exponential with time constant $\tau_0 = (5.2 \times 10^{-12} [O_2])^{-1}$, which is 1/10 sec at 100 km, 4 sec at 120 km, and 70 sec at 150 km deposition altitude. The infrared volume emission rate at time t would then be

(steady-state energy conversion efficiency) \times

$$\tau_0^{-1} \int_{-\infty}^t I(t') \exp - [(t - t')/\tau_0] dt',$$

where $I(t')$ is the energy input rate at previous time t' . The vertical-column emission rate would be this volume emission rate weighted over the auroral deposition altitude profile.

The aircraft measurements -- and for that matter any passive optical remote sensing of aurora, except perhaps of narrow isolated arc forms -- of course refer to a range of emission altitudes. As noted, this range spans about 30 km in the auroras in the data set; it decreases with decreasing altitude of the profile peak (see, for example, Ref 36) and thus generally with auroral intensity, which statistically correlates with hardness of the particle energy spectrum (Ref 37). Thus some imprecision is expected in representations of the altitude-summed time delays by single parameters such as we derive in the next section.

The lag attenuates high-frequency components of the temporal frequency spectrum of SWIR-band emission excited by nuclear particles, with a transfer function that can be

straightforwardly calculated. A similar effect on spatial frequencies of the background radiance results from differential transport of precursor species by wind shear and turbulent diffusion that occurs naturally or is induced by the detonation. The horizontal wind at 120 km has a shear that is highly variable in magnitude and direction (Ref 38), which averages about 100 m/sec per 10 km vertically; thus irradiated air parcels at different altitudes in a few sec move distances relative to one another that are comparable to the projected minimum surveillance-sensor footprint.

DATA REDUCTION -- APPROACH

To make quantitative estimates of the delays we apply two methods discussed in the Test Plan (Ref 28), established statistical cross-correlation and a procedure developed for determining predosing parameters by fitting time-integrated power input to observed radiation output using a simplified model of the latter's grow-in and decay. As noted, the high signal/noise data segments selected are identified in Table 3, whose column headings are described in Ref 1; montages of all-sky views of the visible aurora are in Ref's 1 and 27.

Cross-correlation analysis is particularly useful where foreknowledge of the physical relationship between processes is limited. The cross-correlation function is defined (neglecting for the moment normalization) by

$$C(\tau) = \int_{-\infty}^{\infty} I(t) J(t + \tau) dt,$$

where $I(t)$ is the input (3914 Å photometer) signal at time t , and $J(t + \tau)$ is the output (2.8 - 3.1 μm radiometer) signal at later time $t + \tau$. A narrow maximum in C at $\tau = \tau_1$, for example, would mean that the SWIR emission is shifted by τ_1 seconds; in practice, we expect it to be delayed over a range of times comparable to that required

for the processes in Fig 17 to approach completion. Were $J(t)$ to remain proportional to $I(t)$ (no delay), $C(\tau)$ would be directly proportional to the input's autocorrelation function

$$A(\tau) = \int_{-\infty}^{\infty} I(t) I(t + \tau) dt,$$

which has a maximum at $\tau = 0$. As derived in Ref 28, in the more general case

$C(\tau) = (\text{photon yield}) \times \int_{-\infty}^{\infty} R(\tau + t'') A(t'') dt''$, where R is a predosing function to be discussed shortly and t'' is the time interval between input and output.

To compute C and A we manually digitized 14 of the pairs of data traces at 1 sec intervals, which results in about 180 points per segment; segment 12 was digitized each 0.4 sec since its sharp SWIR enhancement lasted only about 8 sec. Each radiance trace was then time-averaged to zero, and a normalized $C(\tau)$ calculated as

$$C(\tau) = (P - \tau)^{-1} \sum_{t=0}^{(P-1)-\tau} [I(t) - \bar{I}] [J(t + \tau) - \bar{J}] \Delta t,$$

Where P is the total number of data points and \bar{I} and \bar{J} are the average values in the interval (the factor $(P - \tau)^{-1}$ compensates for the decreasing number of terms in the sum as lag τ increases). Subtraction of \bar{I} and \bar{J} formats the above equation to match the well known covariance of statistical analysis; historical usage in both statistics and turbulence theory applies the term cross-correlation to the normalized ratio $C(\tau)/C(0)$, to which results presented in the following subsection refer. We computed $C(\tau)$ for $\tau = 0$ to 10 sec in 1 sec steps, finding that almost all of the segments displayed broadly-peaked cross-correlation functions decreasing back to $C(0)$ in less than 10 sec.

The second procedure fits parameters in a model that calculates the contribution of previous energy input to SWIR

output. It is summarized in the equation

$$q_{NO} = F \int_{-\infty}^t q_0(t') R(t - t') dt',$$

where q_{NO} and q_0 are volume production rates of NO^+ and initial ionizations, F is the fraction of these ionizations that result in NO vibrational-band photons, and R is an impulse-response function that expresses the rate at which earlier energy input leads to emission from NO. (Transport of precursors is neglected, and dissociation of N_2 molecules is lumped with impact ionization, to which it is in any case proportional.) With the assumption that R does not change substantially over the ~30-km range of energy deposition altitudes in typical aurora,

$$q_0(t') = K' I(t'), \quad q_{NO}(t) = K'' J(t),$$

where K' and K'' are constants (K'' is presumed to depend on the column's mean altitude). The predicted SWIR column emission is then

$$J_p(t) = K \int_{-\infty}^t I(t') R(t - t') dt',$$

where K lumps the proportionality constants K' , K'' , and F .

This equation relating the data streams from a single coaligned radiometer-photometer pair applies to aurora that is coherently pulsating while remaining spatially near-uniform over the region scanned by the moving aircraft instruments. Large rates of change of I provide the highest resolution in unfolding R , and constant input of course provides no information about predosing. We select for R a physically reasonable analytical form with two free parameters that are fit to the data. The aerochemistry model (Fig 17) indicates that following impulsive energy input R increases as the concentrations of N_2^D and NO^+ (and perhaps other precursor species) build up, and then decreases as these species become depleted. This suggests a function of the form

$$R = G(t - t')^n \exp[-(t - t')/\tau_0],$$

where τ_0 is the time constant of the decreasing contribution of earlier dosing, n expresses the rate of grow-in of excitation of NO^+ , and G normalizes $\int_{-\infty}^{\infty} R dt$ to 1. (As Ref 28

shows, G is a gamma function and reduces to $1/\tau_0$ for $n = 0$.) The equation that predicts SWIR radiance then becomes

$$J_p(t) = K G \int_{-\infty}^t I(t') (t - t')^n \exp[-(t - t')/\tau_0].$$

K, which refers to the number of SWIR photons emitted per 3914 Å photon, can be determined directly from data taken when the fractional change in input rate is small over the expected predosing time, or by the crossplot-averaging methods of Ref's 1 and 27. Note that two parameters allow independent rates of grow-in and die-out of NO vibrational emission; as mentioned BRIM (Ref 35) assumes instantaneous grow-in, with $n = 0$.

To evaluate n and τ_0 , we summed the above integral over a $t - 20$ sec interval (the aircraft platform moves 4.4 km or ~5 instrument fields of view in this time). The process was repeated (by computer) for n and $\tau_0 = 0$ to 10 in one-unit steps, with smaller steps applied near the best-fit value. Best-fit is at the minimum value of the sum

$$\chi^2 = M^{-1} \sum_i [J(t_i) - J_p(t_i)]^2 / \sigma_i^2,$$

where σ_i is the uncertainty in the measurement of J_i . We took σ_i to be the typical radiometer noise of 20 kR at all data points in calculating the chi-squareds in Figure 23.

Three segments from the data base, 12, 3, and 5, appeared suitable for this impulse-response treatment. Noise and the finite intensity resolution of the data limit the precision with which the parameters in R can be determined, as we will find.

RESULTS -- EVALUATION

The cross-correlations and autocorrelations of I are plotted in Figure 18a and b, broken out into groups in which the aurora was fully sunlit, partially sunlit, and not sunlit. Tabulated values on the figure give τ at the peak of each curve and the halfwidth of that section lying above the normalization to $C(0)$ at 1.00 (dashed horizontal line). $C(\tau)$

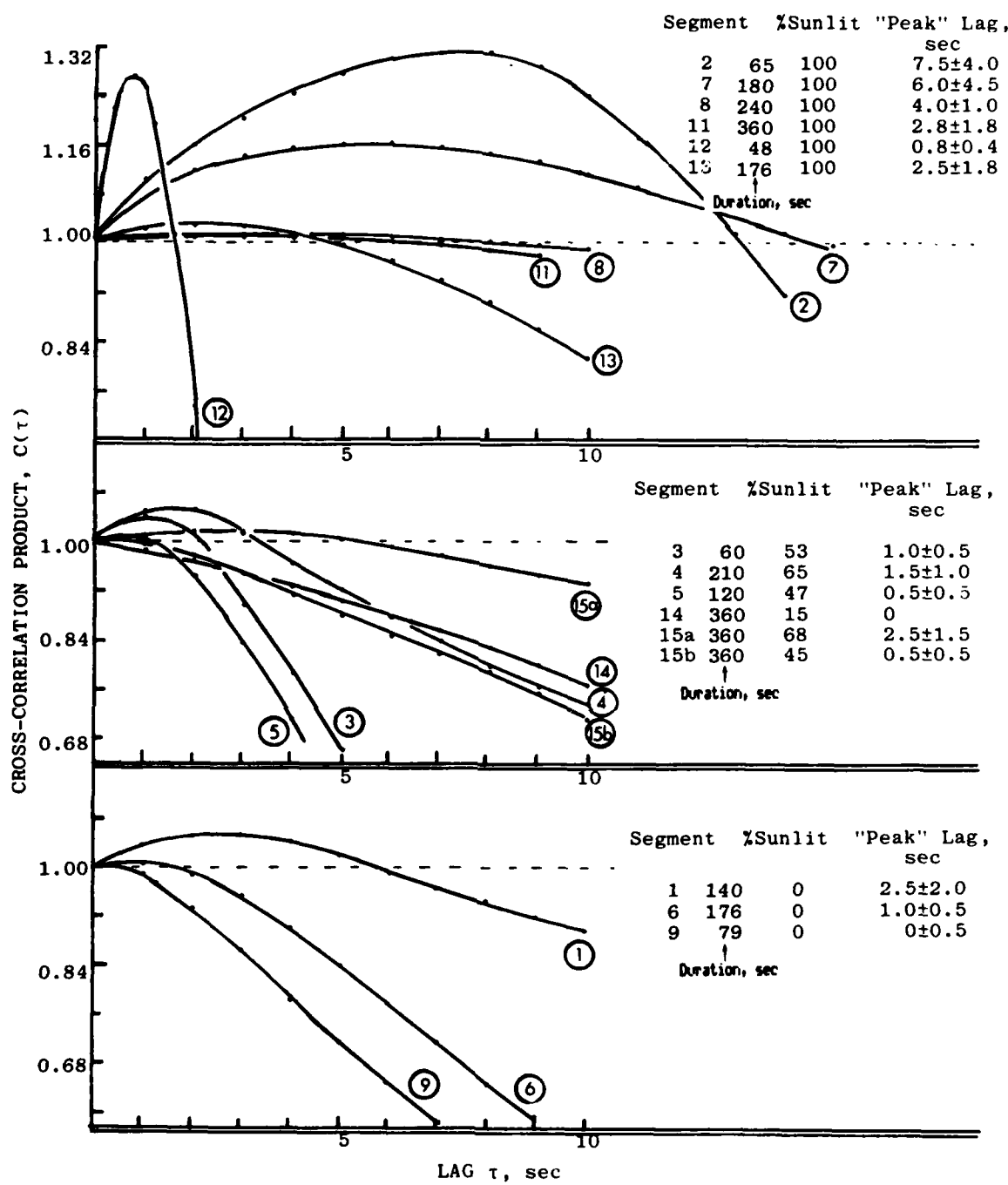


Figure 18a. Cross-correlation functions of the 15 aircraft data streams. The tabulated values are halfwidths above the normalization at 1.0 of the maximum in $C(\tau)$.

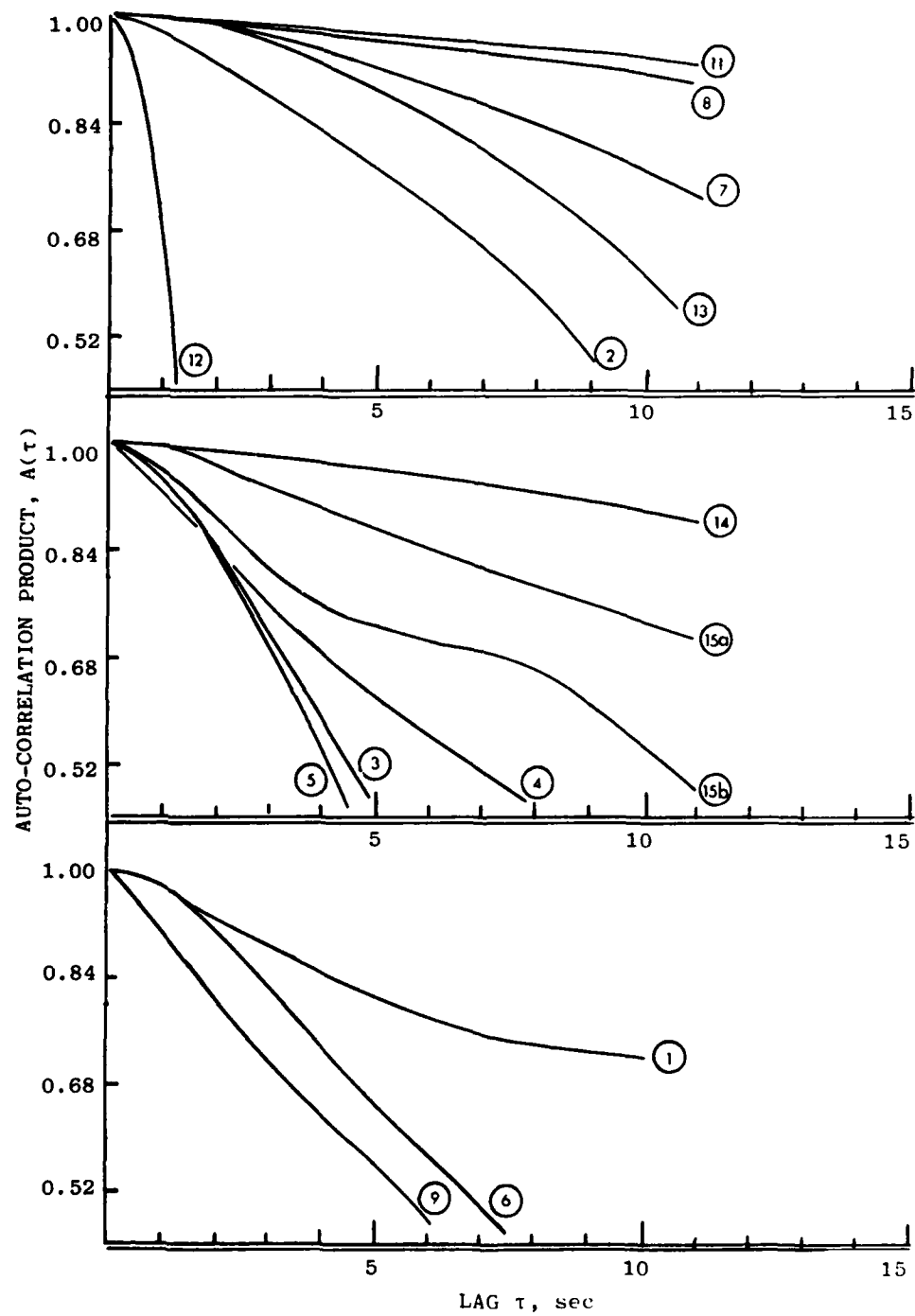


Figure 18b. Auto-correlation functions of the 15 aircraft data streams.

dropping below this zero-offset level implies that further relative shifting of the data streams will result in a poorer match of the two data sets. As expected, the A's all show a maximum at zero lag; no subsidiary peak, which would indicate a <10-sec periodicity in the aurora, is evident (except perhaps in segment 15b).

The location of the peak in the cross-correlation function should not depend on the width of the autocorrelation function, which as expected increases with the length of the data segment. We interpret the location of this maximum as the average lag between SWIR output and particle energy input.

(Note that R's can be estimated by solving the above integral equation $C = \int RAdt$, either by direct fitting of test response functions or by the usual Fourier transform-inverse transform procedure applicable to convolutions; see Ref 28.)

These peaks are compared in Figure 19a with the lags estimated previously by visual inspection of the data streams. The scatter is significant, which is not surprising considering the imprecision of the visual method. (The individual average delays from the cross correlation method are generally less than the offsets of radiation peaks and times for SWIR to drop to baseline.) Figure 19b shows a weak correlation between the lag at maximum C and peak of the energy deposition altitude profile. Although the slope of the straight-line equally weighted least-squares fit is uncertain and the correlation coefficient is low, the upward trend is in the direction predicted from NO chemistry. Figure 19c shows that there is no statistically significant dependence of the amplitude of $C(\tau)/C(0)-1$ on this altitude. The cross plot in Fig 20, in which the lags are again identified by segment number, shows no significant correlation between lag at maximum C and solar illumination.

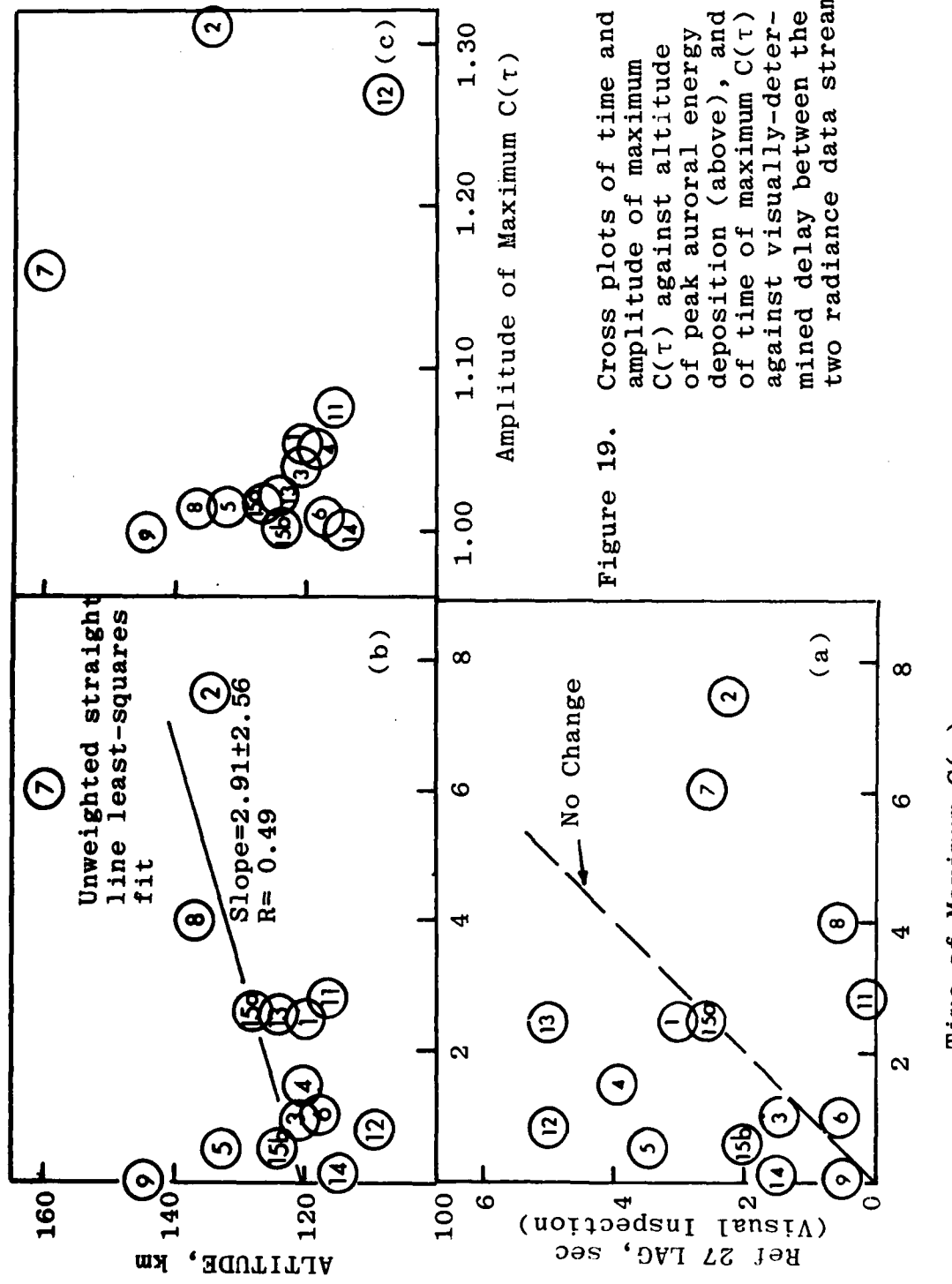


Figure 19. Cross plots of time and amplitude of maximum $C(\tau)$ against altitude of peak auroral energy deposition (above), and of time of maximum $C(\tau)$ against visually-determined delay between the two radiance data streams.

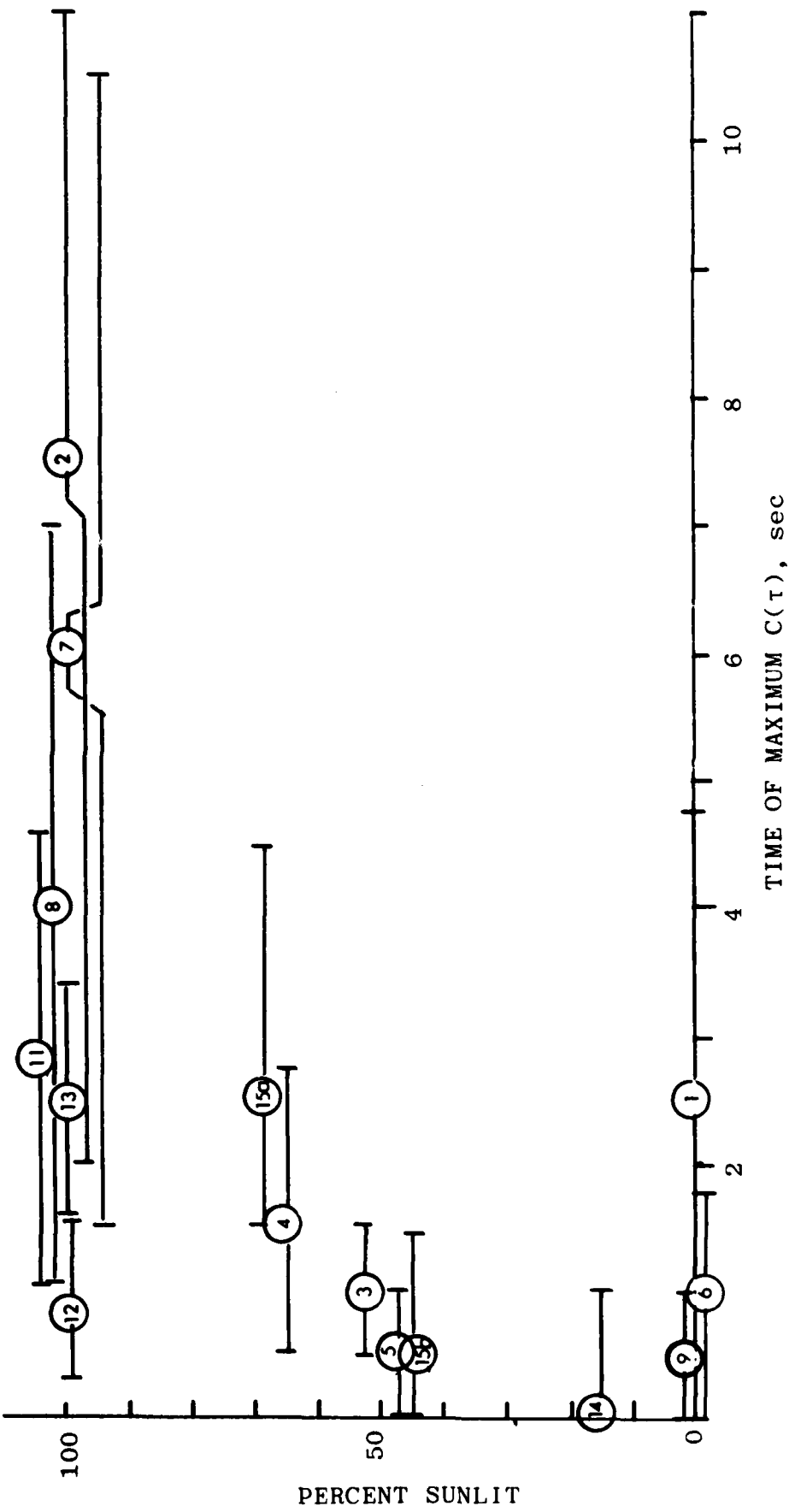


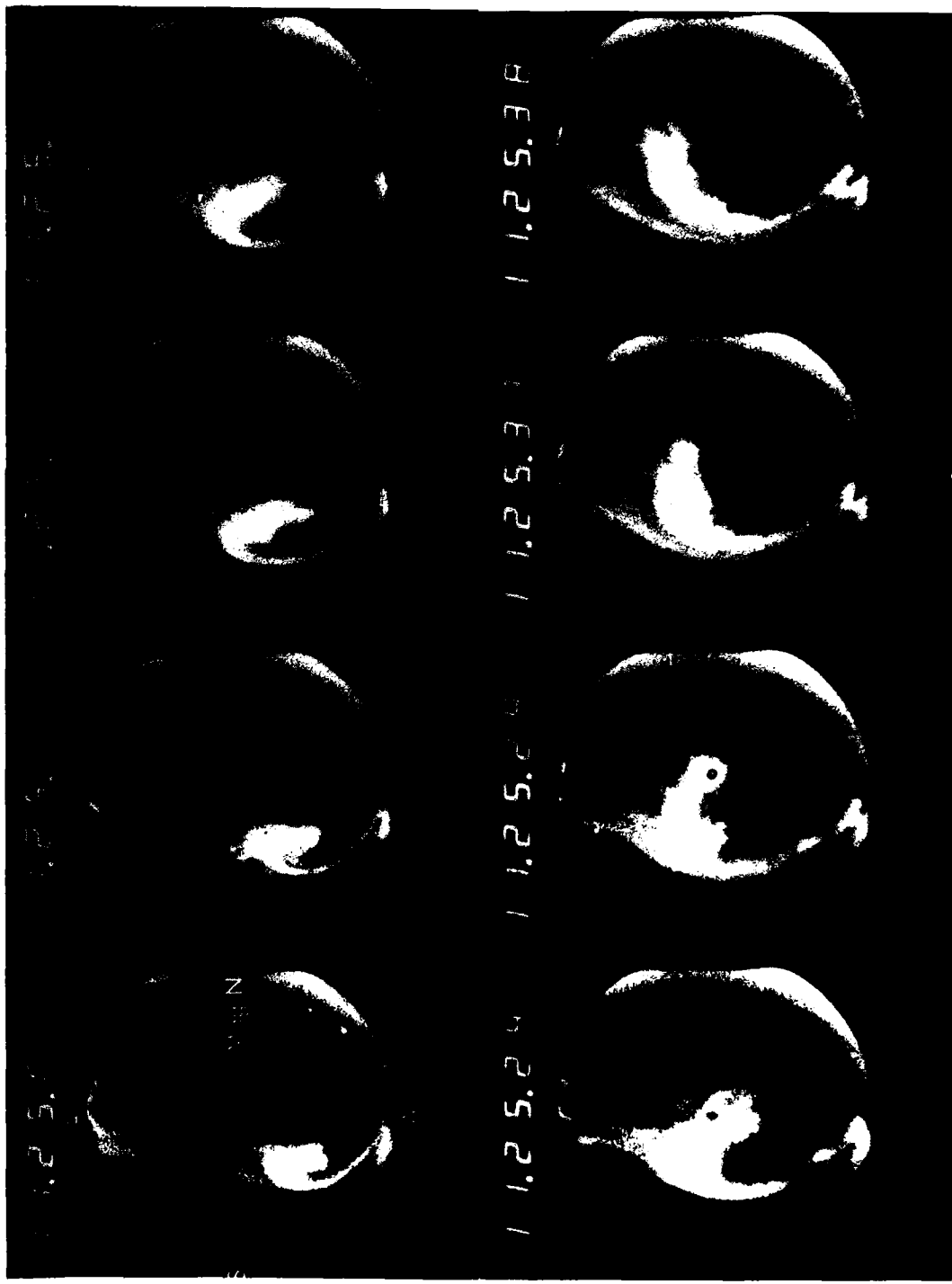
Figure 20. Cross plot of time of maximum $C(\tau)$ against fractional solar illumination of the auroral profile. Error bars refer to the FWHM values tabulated in Fig 18a.

We turn now to deriving the parameters of the model impulse response function R from the three flight segments in which aurora turns on and off most sharply. Consecutive all-sky views of segment 12's sunlit aurora (the perceived best case) are in Figure 21, and the radiance traces are in Figure 22. The center of the small open circle on each frame is the pointing direction of the $\sim 1/3^\circ$ -fields radiometer and photometer. As the aircraft was heading north, the instruments pointed 26° N of the magnetic field direction. Up to 1125:26 a relatively low-level (< 25 kR 3914 Å) diffuse glow lies in the instrument fields, after which a bright (> 100 kR) section of an arc that had formed in the west sweeps rapidly eastward across them.

Two measured quantities enter into the calculation of a set of J_p 's, K (the ratio of total number of SWIR to 3914-Å photons during the data interval) and the OH radiance (the hydroxyl fundamental-band background level within the radiometer's bandpass). In practice, the goodness of fit of the computed J_p 's is sensitive to the choice of both these parameters. The bottom trace in Fig 22 indicates that the hydroxyl overtone radiance remains nearly constant at 50 kR during the period of enhancement; since the ratio of $\Delta v = 1$ to $\Delta v = 2$ in-band OH photons is 2.5:1 (Ref 27), the SWIR pulse would be expected to be superposed on a ~ 125 kR OH background. However the quiescent level of the SWIR signal derived from the actual traces is about 355 kR, which we adopted as the baseline for this segment (the fits using 125 kR are very poor). Similarly, the value of K that we had derived earlier (in Ref 1, 3.1 photons/ photon) is both low compared to that from other segments and results in less-close fits; hence we calculated sets of J_p 's using also $K = 4.6$, which is the ratio at the peak of these traces. These discrepancies in absolute infrared signal strength may indicate some error in calibration of the radiometer in the segment.

SEGMENT 12

Figure 21. All-sky photographs of data segment 12's aurora. The circles show the projection of the field of the radiometer and photometer.



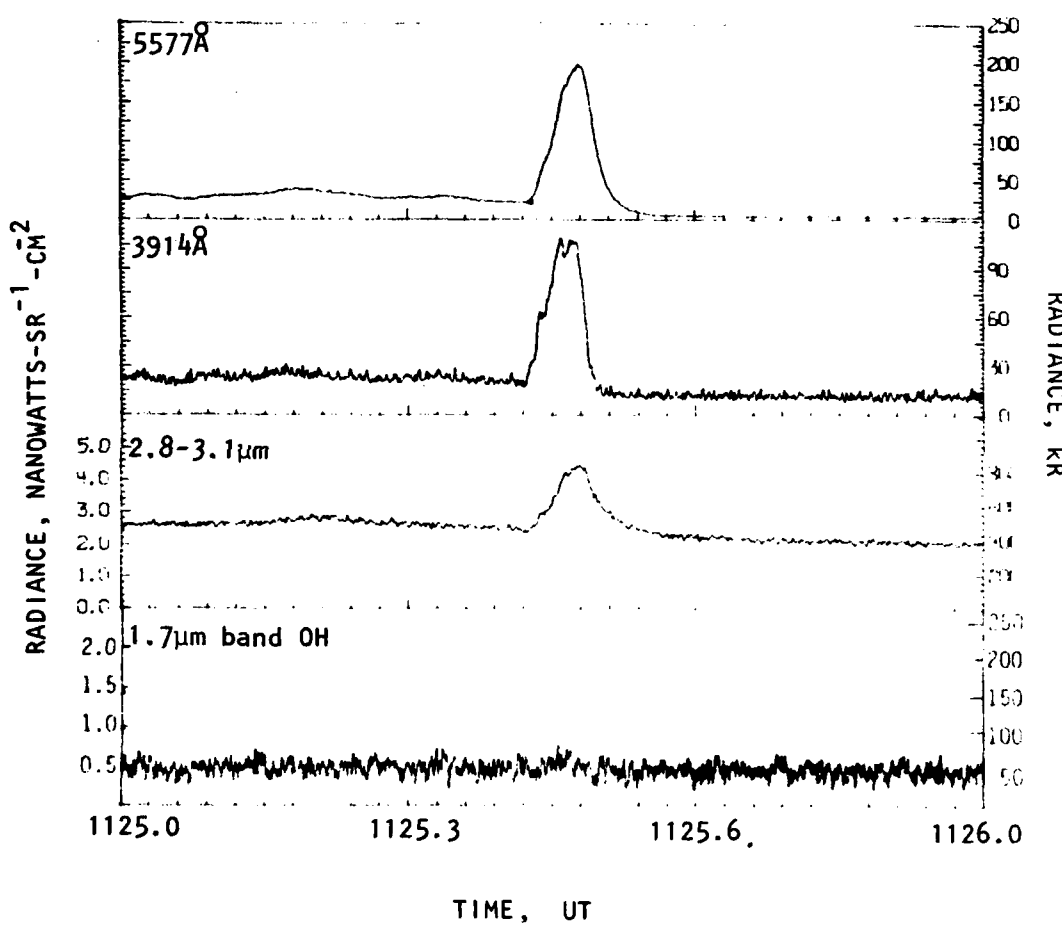


Figure 22. Radiometer and photometer traces of data segment 12's aurora. The supporting data at top and bottom are auroral 5577 Å radiance (photometer aligned with the 3914 Å photometer) and radiance in a section of the hydroxyl overtone-bands airglow (wider-angle radiometer pointed to zenith).

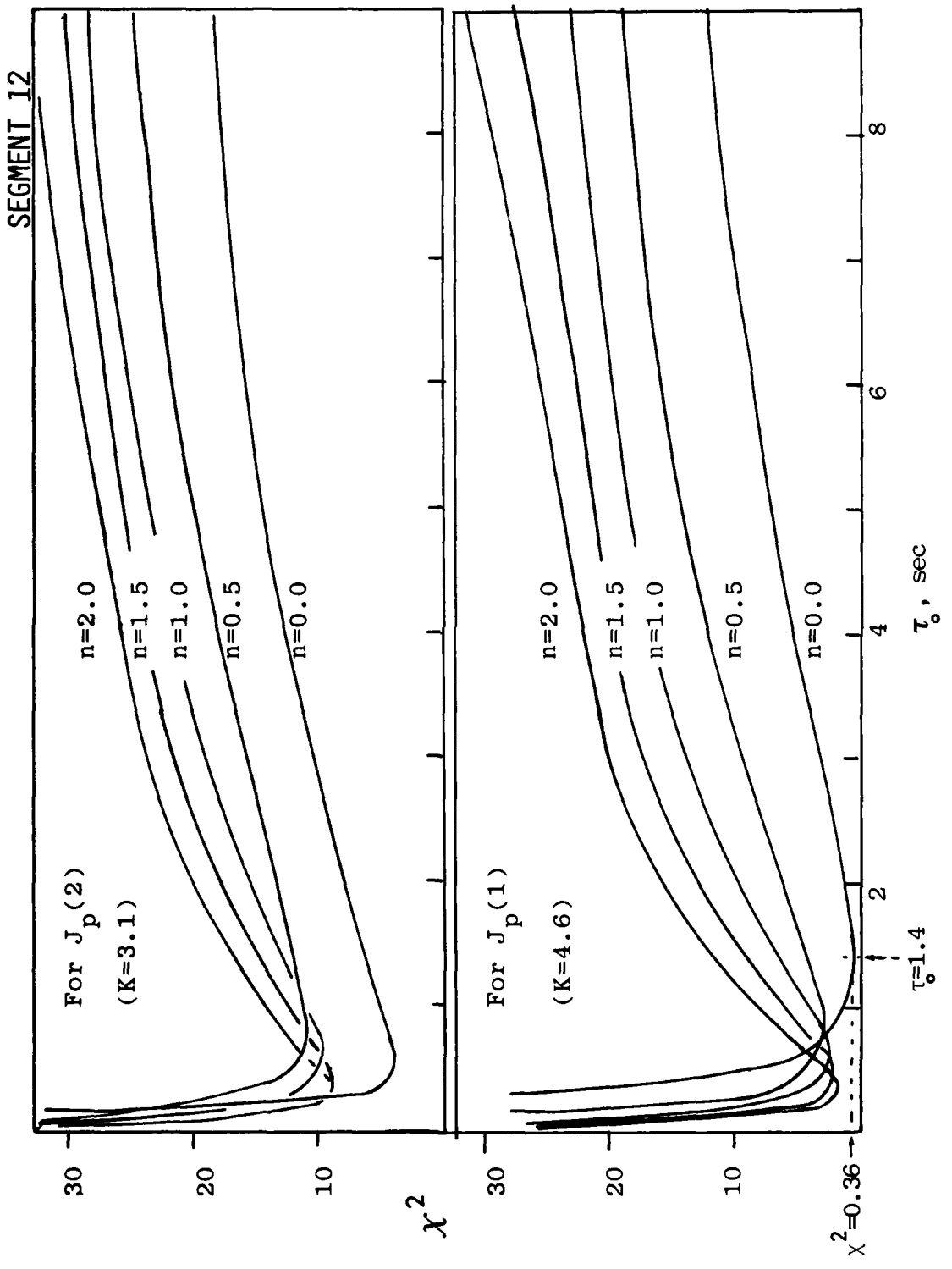


Figure 23. Chi-squared resulting from selection of τ_0 and n for two values of the equilibrium photon emission ratio, data segment 12.

SEGMENT 12

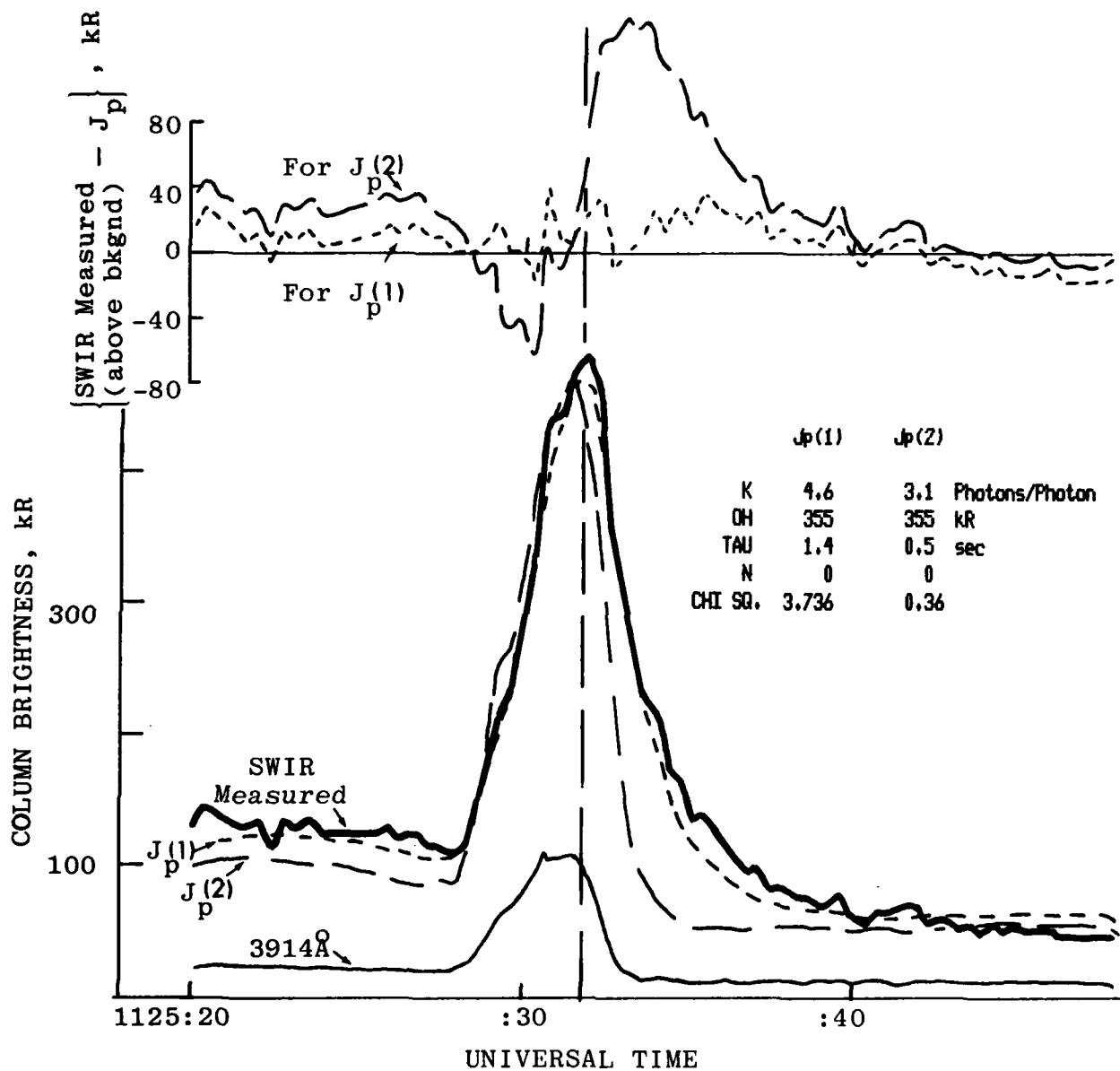


Figure 24. Pest-fits of SWIR predicted from model excitation function to radiance data, segment 12.

Figure 23 plots χ^2 vs τ_0 for n between 0 and 2 for both K 's. χ^2 is relatively insensitive to n and τ_0 , even for these rapidly-changing radiances, as neither set of curves shows a well defined minimum. When $n = 0$ (absolute minimum in χ^2) the best fit is at $\tau_0 = 1.4$ sec selecting $K = 4.6$, and at $\tau_0 = 0.5$ sec for $K = 3.1$. $J_p(t)$ in this case reduces to $K\tau_0^{-1} \int_{-\infty}^t I(t') \exp [-(t-t')/\tau_0] dt'$ (as in BRIM), in which the average lag can be readily shown to be τ_0 . Figure 24 plots measured and predicted SWIR column intensities and their deviation. As can be seen, $J_p(K = 4.6)$ -- that is, with the more plausible energy conversion yield -- gives a much better fit; its standard deviation is 12 kR ($\chi \times 20$ kR noise), compared to 39 kR for $J_p(K = 3.1)$. The 1.4 sec exponential time constant is larger than the 0.8 sec from Fig 18a.

In segment 5 an 80 kR 3914 Å, half-sunlit arc some 30 km in width traverses the instrument fields closely anti-parallel to the aircraft's motion in about 15 sec (Figure 25). Figure 26 shows results from the calculation of J_p , with two n 's because the χ^2 's plots did not show a clear difference between minimums at the best-fit n , τ_0 pairs (not shown). The closest fit is reached with $n = 4.5$, $\tau_0 = 0.2$ sec. With n forced to zero τ_0 is 2.5 sec with a somewhat poorer fit; the standard deviation is 41 kR compared to 26 kR for 4.5, 0.2 sec. Clearly, this data set does not provide good resolution of the effects of predosing. The τ_0 derived with $n = 0$ is again about twice that inferred from the cross correlation method.

In segment 5 the aircraft traversed a narrow, weakening form (Figure 27) that was about half sunlit, with the instruments pointing at magnetic zenith. As the duration of SWIR enhancement was relatively long compared to the expected τ_0 (15-20 sec), it represents a less than ideal case

SEGMENT 3

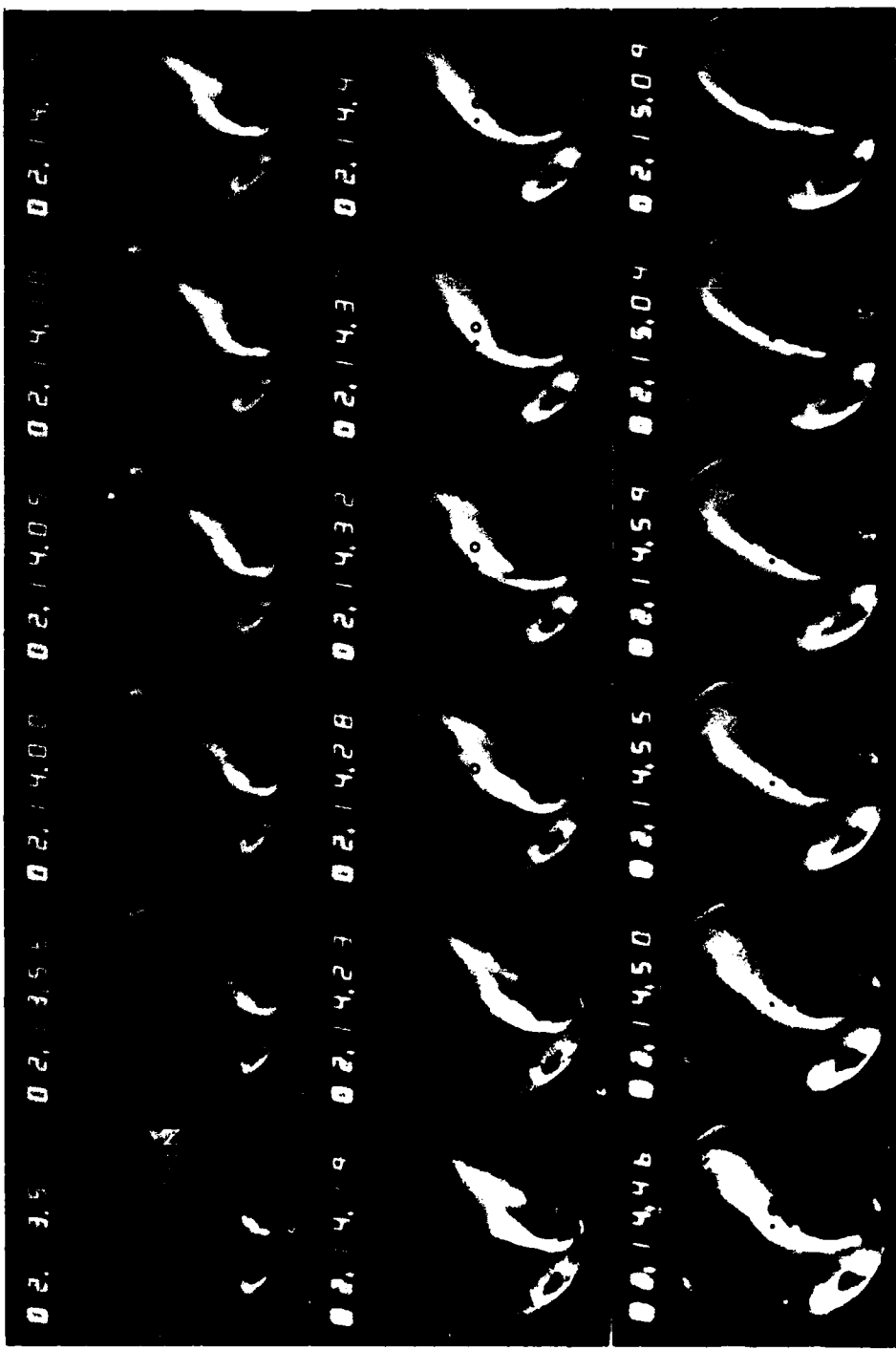


Figure 25. All-sky photographs of data segment 3's aurora.

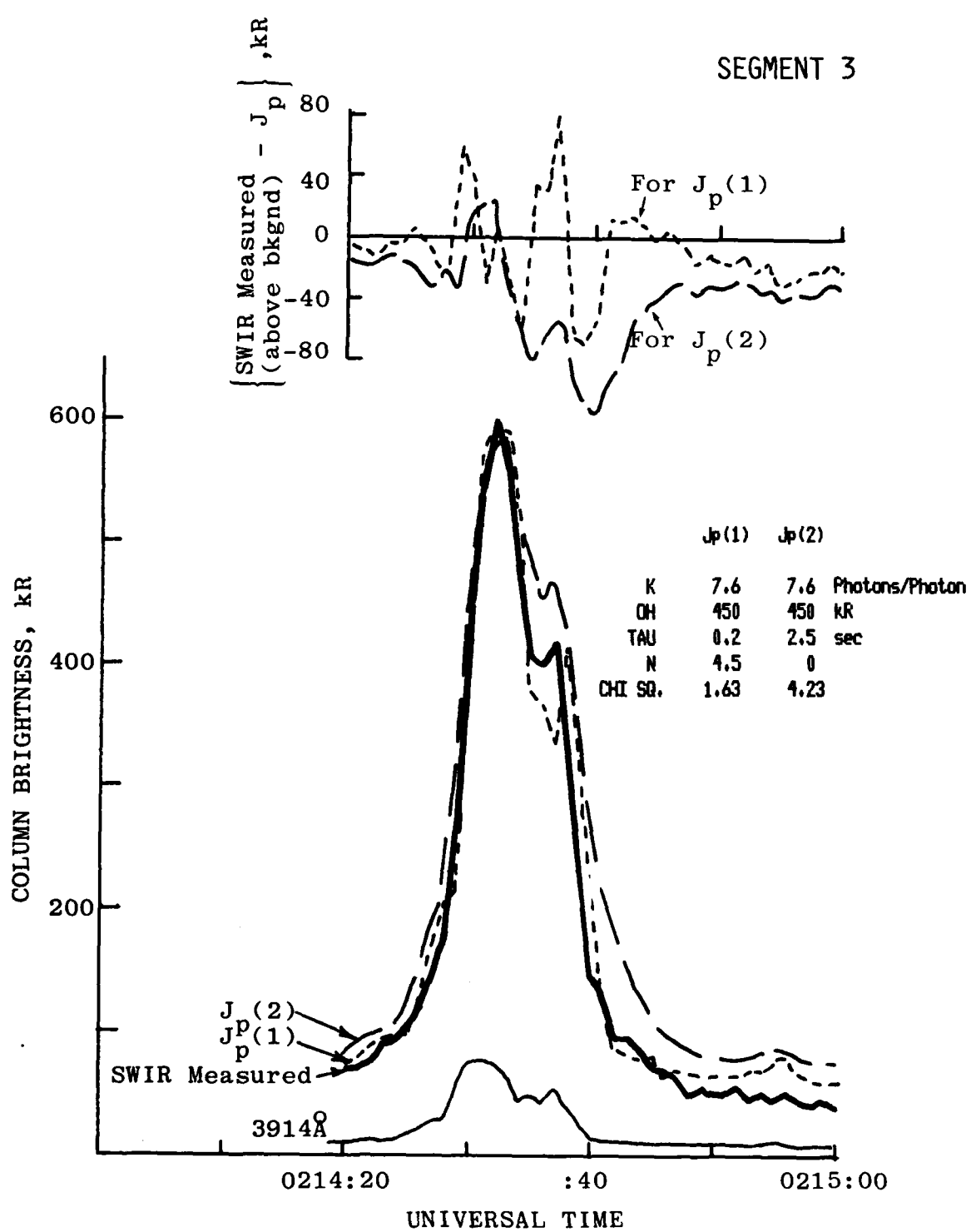
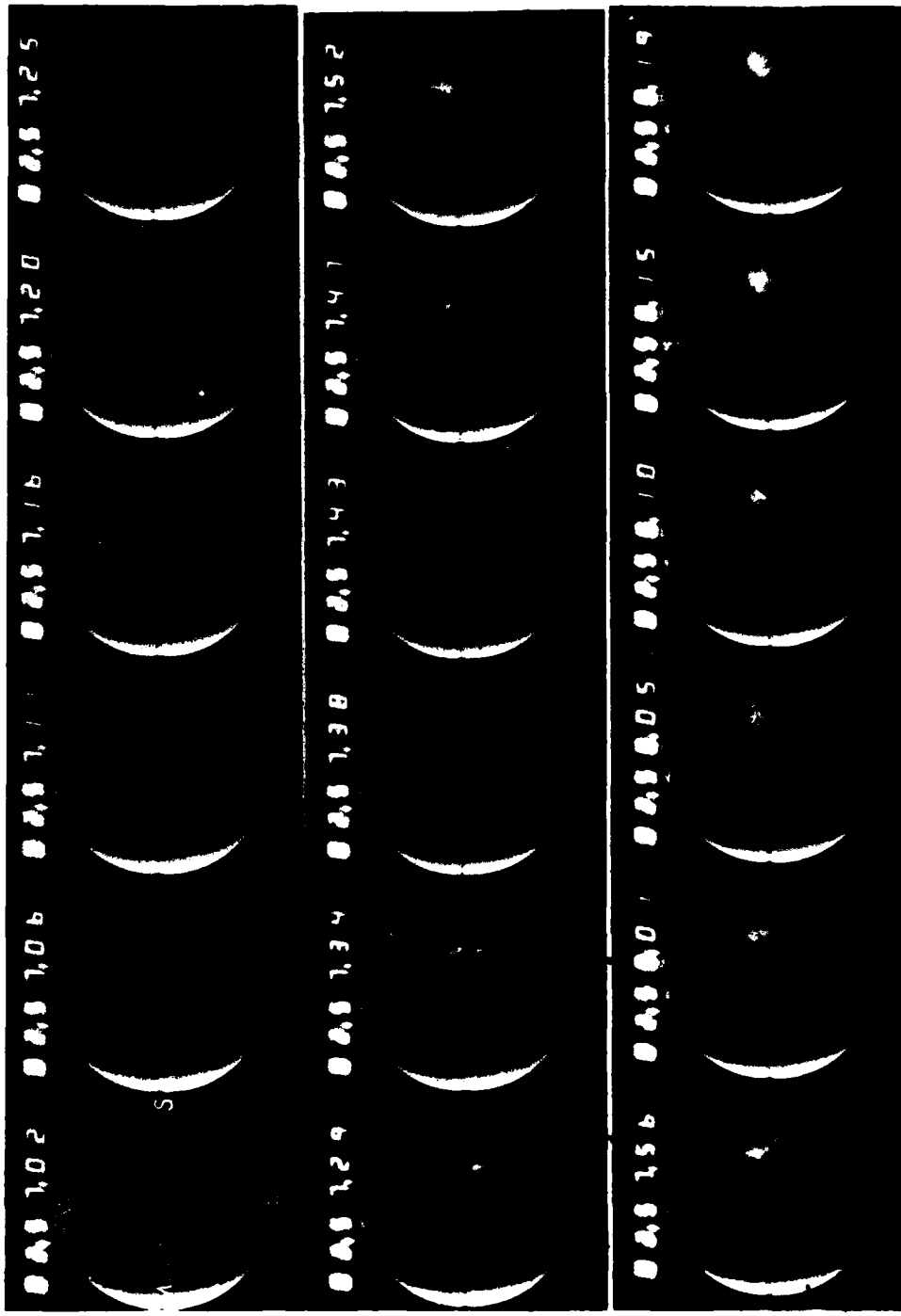


Figure 26. Fit of model SWIR excitation function to radiance data, segment 3.



SEGMENT 5

Figure 27. All-sky photographs of data segment 5's aurora.

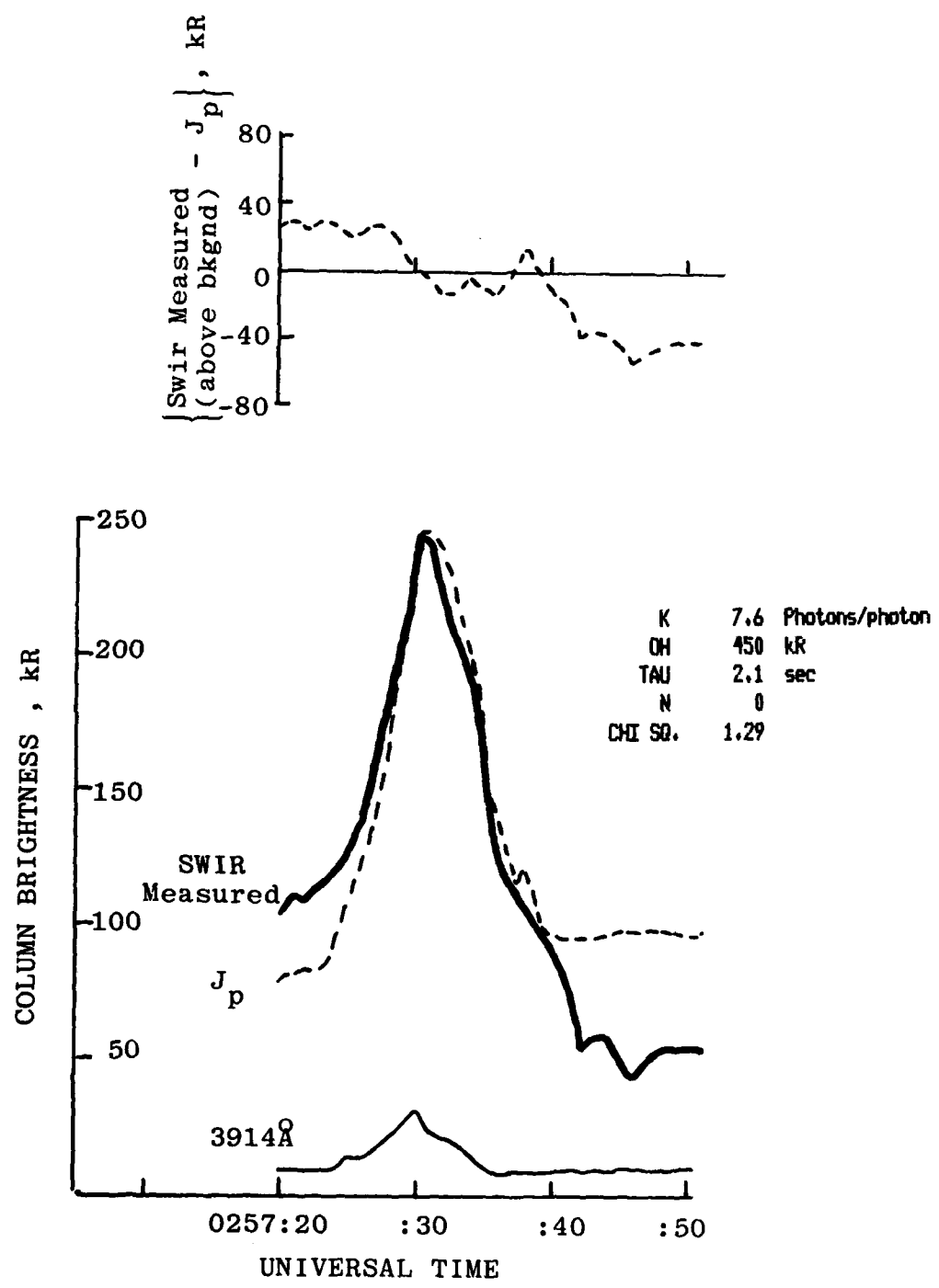


Figure 28. Fit of model SWIR radiance function to radiance data, segment 5.

for impulse-response analysis. The best-fit values (Figure 28) are $n = 0$, $\tau_0 = 2.1$ sec; again τ_0 is about twice that derived from Fig 18a, and no grow-in factor appears. Note however, that the fit of J_p to the measured J is poor before and after passage through the arc, which may indicate a calibration inaccuracy.

CONCLUSIONS

The mean delays between $2.8 - 3.1\mu\text{m}$ -band output and particle energy input inferred from cross correlating the two auroral data streams cluster near 2 sec and vary between 0 and 7 sec with an indication of increasing with the height of the peak in the energy deposition profile between $\sim 110 - 140$ km altitude (Fig 19). Fits of three arc data segments using a simplified input-output model resulted in characteristic exponential SWIR decay time constants about twice those from the cross correlation peaks with no resolvable trend with altitude (the best-fit values were $1\frac{1}{2}$, $2\frac{1}{2}$ and 2 sec). These two-parameter fits suggest that the emission of nitric oxide vibrational radiation from the E region is a maximum immediately after impulsive energy deposition (at the $10^5 - 10^6$ ion pairs/cm³ sec level), that is, that most of the N₂D precursor atoms are produced directly or in very fast reactions.

These lag times are within their resolution consistent with those predicted by current DoD aerochemistry models. (The higher total yields of SWIR nitric oxide overtone radiation, however, are not explained.) Some further aircraft data segments are available, and other analysis techniques may provide better estimates of the time delay and geometric offset of the SWIR emission.

REFERENCES

1. I.L. Kofsky, C.A. Trowbridge, D.P. Villanucci, and M.T. Chamberlain, Further Evaluations of Infrared Simulation Data, DNA TR-81-41 (30 Nov 81).
2. I.L. Kofsky, D.P. Villanucci and R.B. Sluder, Evaluation of Infrared Simulation Data, DNA 5521F (26 Nov 78).
3. D.H. Archer, EXCEDE Energy Deposition: Theory and Experiment Compared, DNA 5525F (30 Nov 80).
4. D.H. Archer, Infrared Program Support: EXCEDE and Related Topics, DNA TR-81-45 (MRC-R-675) (30 Nov 81).
5. R.R. O'Neil (ed.), EXCEDE: Spectral Preliminary Results, AFGL Technical Memorandum 41 (1980).
6. R.R. O'Neil, A.T. Stair, Jr., E.T.P. Lee, D. Burt, and G. Frodsham, EXCEDE: Spectral: An Artificial Auroral Experiment, Paper AIAA-81-0422, AIAA 19th Aerospace Sciences Meeting, 12-15 Jan 81.
7. P.W. Tarr, ARCTIC Code Electron Deposition Theory in Application to Project EXCEDE, DNA 3636T (HAES Report No. 10) (18 Jun 75).
8. W. Bernstein, H. Leinbach, P.J. Kellogg, S.J. Monson, and T. Hallinan, J. Geophys. Res. 84, 7271 (1979).
9. L.M. Linson and K. Papadopoulos, Review of the Status of Theory and Experiment for Injection of Energetic Electron Beams in Space, Science Applications, Inc. LAPS 65 (1980).
10. P.M. Banks, C.R. Chappell, and A.F. Nagy, J. Geophys. Res. 79, 1459 (1974).
11. T.L. Stephens and A.L. Klein, Electron Energy Deposition in the Atmosphere (Vol 1), GE-TMP-7 (May 1975).
12. E.P. Szuszczewicz, K. Papadopoulos, W. Bernstein, C.S. Lin, and D.N. Walker, J. Geophys. Res. 87, 1565 (1982).
13. B. Grandal (ed.), Artificial Particle Beams in Space Plasma Studies, Plenum, New York, 1982.
14. J.R. Winckler, Rev. Geophys. Space Phys. 18, 659 (1980).
15. R.E. Leadon, A.J. Woods, E.P. Wenaas, and H.H. Klein, An Analytical Investigation of Emitting Probes in an Ionized Plasma, Jaycor Report J200-80-250A/2172 (12 Apr 81).

REFERENCES (continued)

16. A.V. Jones, Space Sci. Rev. 11, 826 (1971).
17. T.J. Hallinan and P. Wagner, Final Report on Contract DNA001-80-C-0260 (Dec 81).
18. J.D. Algeo and M.B. Denton, Appl. Spectroscopy 35, 35 (1981).
19. P.R. Bevington, Data Reduction and Analysis for the Physical Sciences, McGraw-Hill, New York, 1969.
20. K. Papadopoulos and K. Ko, Private Communication (Sep 82).
21. R.O'Neil, Private Communication (1981).
22. J.J. Scialdone, J. Vac. Sci. Tech. 9, 1007 (1972).
23. B.A. Mirtov, IGY Annals XII, Chapter 5.7 (1957-58).
24. J.J. Scialdone, A.B. Hedin, and C.J. Rice, J. Geophys. Res. 83, 195 (1978).
25. D. Golomb and M.A. Macleod, J. Geophys. Res. 71, 2299 (1966).
26. G. Israelson and J.R. Winckler, J. Geophys. Res. 84, 1442 (1979).
27. E.R. Huppi, D. Villanucci, and M. Bruce, Temporal and Spatial Structure of Short Wavelength Infrared Backgrounds, AFGL-TR-81-0299 (13 Oct 81).
28. I.L. Kofsky, D.P. Villanucci, and W.S. Andrus, Assessment of Rocketborne and Airborne Infrared Data, DNA 4731F (30 Nov 78).
29. R.B. Sluder, W.S. Andrus, I.L. Kofsky, and D.P. Villanucci, Aircraft Program for Target, Background, and Sky Radiance Measurements, AFGL-TR-78-0123 (18 May 78).
30. I.L. Kofsky, D.P. Villanucci, and R.B. Sluder, Data Reduction and Auroral Characterizations for ICECAP III, DNA 4220F (31 Jan 77).
31. G.E. Caledonia and J.P. Kennealy, Planet. Space Sci. 30, 1043 (1982).
32. J.E. Davenport, T.G. Slanger, and G. Black, J. Chem. Phys. 64, 4442 (1976).

REFERENCES (concluded)

33. J.E. Frederick and D.W. Rusch, J. Geophys. Res. 82, 3509 (1977).
34. D.H. Archer, Private communication (1982).
35. J.B. Kumer, R.D. Sears, J.E. Evans, S.E. Harris, and R.M. Nadile, Application of Visible Monochromatic Auroral Imaging Data for Modeling Infrared Earth-Limb Morphology, AFGL-TR-81-0025 (26 Mar 81).
36. A. Belon, G.J. Romick, and M.H. Rees, Planet. Space Sci. 14, 597 (1966).
37. S.B. Mende and R.H. Eather, J. Geophys. Res. 80, 3211 (1975).
38. J.P. Heppner and M.L. Miller, J. Geophys. Res. 87, 1683 (1982).

DISTRIBUTION LIST

DEPARTMENT OF DEFENSE

Assistant to the Secretary of Defense
 Atomic Energy
 ATTN: Exec Asst

Defense Nuclear Agency
 ATTN: RAAE, P. Lunn
 ATTN: RAAE, H. Fitz, Jr
 ATTN: RAAE, W. McKechnie
 4 cy ATTN: TITL

Defense Tech Info Ctr
 12 cy ATTN: DD

Field Command Defense Nuclear Agency
 Det 1

Lawrence Livermore Lab
 ATTN: FC-1

Field Command
 Defense Nuclear Agency
 ATTN: FCTT, W. Summa
 ATTN: FCTT, G. Ganong
 ATTN: FCTT
 ATTN: FCPR

Under Secretary of Defense for Rsch & Engrg
 ATTN: Strat & Space Sys (OS)
 ATTN: Defensive Systems
 ATTN: Strat & Theater Nuc Forces, B. Stephan

DEPARTMENT OF THE ARMY

Atmospheric Sciences Lab
 USA Elect R&D Cmd
 3 cy ATTN: DELAS-EO, F. Niles

BMD Advanced Tech Ctr
 ATTN: ATC-T, M. Capps
 ATTN: ATC-O, W. Davies

BMD Systems Cmd
 2 cy ATTN: BMDSC-HW

Deputy Chief of Staff for Rsch Dev & Acq
 ATTN: DAMA-CSS-N

Harry Diamond Labs
 2 cy ATTN: DELHD-NW-P

USA Ballistic Rsch Labs
 ATTN: DRDAR-BLB, J. Mester
 ATTN: DRDAR-BLA-S

USA Cmbt Surv & Target Acq Lab
 ATTN: DELCS-K, S. Kronenberg

USA Foreign Science & Tech Ctr
 ATTN: DRXST-SD

USA Nuc & Chem Agcy
 ATTN: Library

USA Rsch Office
 ATTN: R. Mace

DEPARTMENT OF THE NAVY

Naval Electronic Systems Cmd
 ATTN: PME 117-20

Naval Intel Spt Ctr
 ATTN: Doc Con

Naval Postgraduate School
 ATTN: Code 1424 Library

Naval Rsch Lab
 ATTN: Code 4128.2, J. Johnson
 ATTN: Code 6700, T. Coffey
 ATTN: Code 6780, J. Fedder
 ATTN: Code 4700.1, W. Ali
 ATTN: Code 4139, D. McNutt
 ATTN: Code 2627
 ATTN: Code 2000, J. Brown
 ATTN: Code 4780, D. Strobel
 ATTN: Code 4720, J. Davis
 ATTN: Code 4780, S. Ossakow

Naval Surface Wpns Ctr
 ATTN: Code X211
 ATTN: Code F31

DEPARTMENT OF THE AIR FORCE

Air Force Geophysics Lab
 ATTN: OPR, D. Smith
 2 cy ATTN: OPR, R. Armstrong
 2 cy ATTN: OPR, D. Paulson
 2 cy ATTN: OPR, R. Nadile
 2 cy ATTN: LKO, R. Huffman
 2 cy ATTN: OPR, R. Sharma
 2 cy ATTN: LKB, K. Champion
 2 cy ATTN: LKD, R. Narcisi
 2 cy ATTN: OPR, R. Murphy
 2 cy ATTN: OPR, R. O'Neill
 4 cy ATTN: CA, A. Stair

Air Force Office of Scientific Rsch
 ATTN: AFOSR/NC

Air Force Systems Cmd
 ATTN: SDR
 ATTN: DLTW
 ATTN: DLXP
 ATTN: DLS
 ATTN: DLAE

Air Force Tech Applications Ctr
 ATTN: Tech Library
 ATTN: TD
 ATTN: TF

Air Force Wpns Lab
 ATTN: SUL

Air University Library
 ATTN: AUL-LSE

Deputy Chief of Staff
 Rsch, Dev & Acq
 3 cy ATTN: AFRDS, Space Sys & C3 Dir

DEPARTMENT OF THE AIR FORCE (Continued)

Rome Air Development Ctr
ATTN: OCD, J. Simons

Space Division
ATTN: WE
ATTN: YGD
ATTN: YN

DEPARTMENT OF ENERGY

Department of Energy
Office of Mil Appl
ATTN: OMA, DP-22

OTHER GOVERNMENT AGENCIES

Central Intelligence Agcy
ATTN: OSWR/NED

Department of Commerce
National Bureau of Standards
ATTN: A. Phelps

Department of Commerce
National Bureau of Standards
ATTN: Sec Ofc for J. Devoe
ATTN: Sec Ofc for R. Levine
ATTN: Sec Ofc for M. Krauss
ATTN: Sec Ofc for S. Abramowitz

Department of Commerce
National Oceanic & Atmospheric Admin
3 cy ATTN: E. Ferguson
3 cy ATTN: F. Fehsenfeld

Institute for Telecommunications Sciences
National Telecommunications & Info Admin
ATTN: G. Falcon
ATTN: W. Utlauf

NASA
ATTN: Tech Library
ATTN: Code 6801, A. Tempkin
ATTN: Code 900, J. Siry
3 cy ATTN: A. Aiken

NASA
ATTN: W. Roberts
ATTN: N. Stone
ATTN: J. Watts

NASA
ATTN: MS-168, C. Schexnayder

NASA
ATTN: N-245-3, R. Whitten

NASA
ATTN: J. Gray

NASA Headquarters
ATTN: I. Schardt, Code EE

OTHER AGENCIES

Government Publications Library-M
ATTN: J. Winkler

OTHER AGENCIES (Continued)

Yale University
ATTN: Engrg Dept

DEPARTMENT OF ENERGY CONTRACTORS

University of California
Lawrence Livermore National Lab
ATTN: L-325, G. Haugan
ATTN: L-262, D. Wuebbles
ATTN: L-48, E. Woodward
ATTN: L-10, A. Grossman
ATTN: L-10, H. Kruger
ATTN: L-71, J. Chang
ATTN: L-262, W. Duewer

Los Alamos National Lab
ATTN: Librarian
ATTN: MS 670, J. Hopkins
ATTN: T. Kunkle, ESS-5
ATTN: M. Sandford
ATTN: M. Pongratz
ATTN: G. Smith
ATTN: MS362 Library
ATTN: R. Jeffries
ATTN: D. Sappenfield

Sandia National Labs
ATTN: T. Cook

Sandia National Labs
ATTN: Tech Library 3141
ATTN: L. Anderson
ATTN: M. Kramm
ATTN: ORG 1250, W. Brown

DEPARTMENT OF DEFENSE CONTRACTORS

Aero-Chem Rsch Labs, Inc
ATTN: A. Fontijn

Aerodyne Rsch, Inc
ATTN: C. Kolb
ATTN: J. Wormhoudt
ATTN: M. Zahnizer
ATTN: M. Camac

Aerospace Corp
ATTN: J. Straus
ATTN: J. Reinheimer
ATTN: I. Garfunkel
ATTN: T. Widhopf
ATTN: V. Josephson
ATTN: H. Mayer
ATTN: N. Cohen

AVCO Everett Rsch Lab, Inc
ATTN: A830
ATTN: C. Von Rosenberg, Jr
ATTN: Tech Library

Battelle Memorial Institute
ATTN: H. Lamuth
ATTN: Stoiac
ATTN: R. Thatcher

Berkeley Rsch Assoc, Inc
ATTN: J. Workman
ATTN: S. Brecht

DEPARTMENT OF DEFENSE CONTRACTORS (Continued)

Boston College
ATTN: E. Hegblom
ATTN: W. Grieder

The Trustees of Boston College
2 cy ATTN: Chairman Dept of Physics
2 cy ATTN: Chairman Dept of Chemistry

University of California at Riverside
ATTN: J. Pitts, Jr

California Institute of Technology
ATTN: J. Ajello

Calspan Corp
ATTN: W. Wurster
ATTN: M. Dunn
ATTN: J. Grace
ATTN: C. Treanor

University of Colorado
ATTN: C. Lineberger-JILA
ATTN: G. Lawrence-LASP

Columbia University
ATTN: Sec Officer for H. Folcy

Computer Sciences Corp
ATTN: F. Eisenbarth

Concord Sciences
ATTN: E. Sutton

Cornell University
ATTN: M. Kelly

University of Denver
ATTN: Sec Officer for D. Murcay

University of Denver
ATTN: B. Van Zyl

Environmental Rsch Inst of Michigan
ATTN: Iria Library

EOS Technologies, Inc
ATTN: B. Gabbard

General Electric Co
ATTN: P. Zavitsanos
ATTN: R. Edsall

GEO Centers, Inc
ATTN: E. Marram

HSS, Inc
ATTN: M. Shuler

Institute for Defense Analyses
ATTN: E. Bauer
ATTN: H. Wolfhard

IRT Corp
ATTN: H. Mitchell

Kaman Sciences Corp
ATTN: J. Jordano

DEPARTMENT OF DEFENSE CONTRACTORS (Continued)

Kaman Tempo
ATTN: B. Gambill
ATTN: J. Devore
ATTN: K. Schwartz
5 cy ATTN: DASIAC

Kaman Tempo
ATTN: DASIAC

Lockheed Missiles & Space Co, Inc
ATTN: J. Reagan
ATTN: M. Walt
ATTN: B. McCormac
ATTN: J. Kumer
ATTN: J. Cladis
ATTN: R. Sears
ATTN: J. Perez

University of Lowell
ATTN: G. Best

Mission Rsch Corp
ATTN: D. Archer
ATTN: F. Guigliano
ATTN: P. Fischer
ATTN: D. Sowle
ATTN: M. Scheibe
ATTN: R. Hendricks
ATTN: R. Kilb
2 cy ATTN: Tech Library

Nichols Rsch Corp, Inc
ATTN: R. Burns

Pacific-Sierra Rsch Corp
ATTN: H. Brode, Chairman SAGE

PhotoMetrics, Inc
4 cy ATTN: I. Kofsky
4 cy ATTN: M. Chamberlain
4 cy ATTN: D. Villanucci

Physical Dynamics, Inc
ATTN: A. Thompson

Physical Rsch, Inc
ATTN: T. Stephens

Physical Science Lab
ATTN: W. Berning

Physical Sciences, Inc
ATTN: T. Rawlings
ATTN: K. Wray
ATTN: R. Taylor
ATTN: D. Greem
ATTN: G. Caledonia

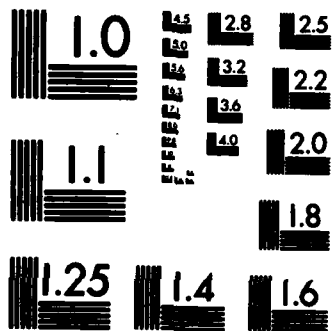
Physics International Co
ATTN: Tech Library

University of the Commonwealth at Pittsburgh
ATTN: F. Kaufman
ATTN: M. Biondi
ATTN: W. Fite

Princeton University
ATTN: Librarian

HD-A137 267 INTERPRETATION OF EXCDE: SPECTRAL AND AURORAL INFRARED 2/2
SIMULATION DATA(U) PHOTOMETRICS INC WOBURN MA
I L KOFSKY ET AL. 30 NOV 82 PHM-TR-82-04 DNA-TR-81-191
UNCLASSIFIED DNA001-81-C-0003 F/G 4/1 NL





MICROCOPY RESOLUTION TEST CHART
NATIONAL BUREAU OF STANDARDS-1963-A

DEPARTMENT OF DEFENSE CONTRACTORS (Continued)

R&D Associates

ATTN: R. Lindgren
ATTN: F. Gilmore
ATTN: H. Dry
ATTN: R. Turco
ATTN: P. Haas

R&D Associates

ATTN: B. Yoon
ATTN: J. Rosengren

Rand Corp

ATTN: P. Davis
ATTN: C. Crain

Rand Corp

ATTN: B. Bennett

Science Applications, Inc

ATTN: D. Hamlin
ATTN: D. Sachs

Science Applications, Inc

ATTN: E. Hyman

Space Data Corp

ATTN: S. Fisher

Spectral Sciences, Inc

ATTN: F. Bein

SRI International

ATTN: R. Leadabrand
ATTN: D. McDaniels
ATTN: J. Casper
ATTN: W. Chesnut

DEPARTMENT OF DEFENSE CONTRACTORS (Continued)

SRI International
ATTN: C. Hulbert

Stewart Radiance Lab
ATTN: R. Huppi
ATTN: J. Ulwick

Technology International Corp
ATTN: W. Boquist

Teledyne Brown Engineering
ATTN: F. Leopard
ATTN: N. Passino
ATTN: MS-12 Tech Library

Toyon Rsch Corp
ATTN: J. Ise

Utah State University
Attention Sec Con Ofc for
ATTN: C. Wyatt
ATTN: A. Steed
ATTN: D. Baker
ATTN: K. Baker, Dir Atmos & Space Sci

Visidyne, Inc

ATTN: T. Degges
ATTN: W. Reidy
ATTN: C. Humphrey
ATTN: J. Carpenter
ATTN: H. Smith
ATTN: O. Shepard

Wayne State University
ATTN: R. Kummier
ATTN: W. Kauppila

